THESIS

DESIGN AND IMPLEMENTATION OF THE SBX1: A SMART ENVIRONMENT CHAMBER FOR BIOLOGICAL RESEARCH AND DISCOVERY

Submitted by

Daniel S. Ball

Department of Electrical and Computer Engineering

In partial fulfillment of the requirements

For the Degree of Master of Science

Colorado State University

Fort Collins, Colorado

Summer 2021

Master's Committee:

Advisor: Thomas Chen

Jesse Wilson
Adam Chicco

ABSTRACT

DESIGN AND IMPLEMENTATION OF THE SBX1: A SMART ENVIRONMENT CHAMBER FOR BIOLOGICAL RESEARCH AND DISCOVERY

Modern biomedical laboratories make significant use of environmentally controlled chambers for incubation and examination of live cell samples. They require precise control over temperature, humidity, and gas concentration to mimic natural conditions for cell survival and growth. Many incubators and live cell imaging systems exist as commercial products; however, they are prohibitively expensive, costing tens or hundreds of thousands of dollars depending on capabilities of the system.

This thesis presents the electrical, optical, mechanical, and software design of the SBX1 Smart Environment Chamber. This device aims to fulfill the needs of most users at a lower cost than current commercial offerings, providing an opportunity for less funded labs to pursue biomedical research and development. The chamber provides temperature, humidity, and gas concentration controls, an internal microscope with an automated stage, and an integrated ARM microcomputer to with a graphical user interface for control and monitoring of the system.

A patent has been filed for the SBX1; application no. US 2020/0324289 A1.

ACKNOWLEDGEMENTS

- Professor Thomas Chen: As a professor you provided me with world class instruction and expertise. As an advisor you provided mentorship, guidance, and support that made this a possibility. Thank you for your wisdom and your patience.

- Professor Sanjay Rajopadhye: Serendipity gave me a position in your amazing lab. Without it, I would have struggled to finish an undergraduate degree, let alone a master's degree. I also wouldn't find any humor in tessellated kangaroos.

- Dr. Jeffrey J. Field: Thank you for taking the time to consult with me regarding the microscope optics and illumination and the loan of your test slides.

- Dr. Elaine Carneval: Thank you for discussing your needs for equine/bovine oocyte incubation, and for the loan of your portable incubator.

- Caleb Begly: Thank you for your support, your expertise, and more importantly your friendship. You are a great duck.

- Ming-Hao Cheng: Thank you for putting up with me. I'm sorry I never got around to putting plumbing in your house.

- Lang Yang. You were one of the best TAs I could have asked for. Thank you also for liaising with the Chinese manufacturers for injection molding and prototyping quotes.

- William Tedjo, and Yusra Obeidat: Thank you for your tutelage and advice.

DEDICATION

Grandma, I will never know how you fit so much love in such a tiny package. I'm sorry that I couldn't finish before you left.

Stitch, thanks for keeping me going through the hard times. I'll miss you.

TABLE OF CONTENTS

LIST OF TABLES

LIST OF FIGURES

Chapter 1

Introduction

An environmental chamber is a widely used apparatus in biological research and product development. Traditional environmental chambers are mainly used for bio-sample storage. As a storage apparatus for bio-samples and biomaterials, the main function of a traditional environmental chamber is to maintain a desired temperature and humidity for the storage space (or subspace) for applications such as microbiological incubation. Therefore, environmental chambers are often referred to as incubators. These two terms are used interchangeably in this thesis.

Laboratory incubators come in a great variety of form factors and feature sets. Larger models, akin to industrial refrigerators, can incubate many cultures in the same environment. Smaller bench-top versions are available when lab space is at a premium and large volume is less important. There are even small stage-top incubators, able to be directly placed on a compatible microscope stage for imaging without disrupting the environment.

The most basic units only include temperature control and possibly humidification. The role of humidification is simply to keep media from evaporating. Rather than precise control, it is common to maintain a high (>90%) relative humidity inside the enclosure [1]. Temperature control, on the other hand, has a marked impact on the survival, growth, and behavior of cell and microbe cultures. Mesophilic organisms thrive at or around body temperature, between 30 and 39°C [2]. Included in this category are commonly studied pathogens such as *Streptococcus pyogenes* and *Escherichia coli* as well as probiotic organisms such as those residing in the intestines like lactic acid bacteria [2]. Another significant mesophile is Saccharomyces cerevisiae. Most notably used in baking and brewing this yeast species in particular has seen significant use in genetics studies as a model organism and as a cell factory for production of a variety of chemicals and pharmaceuticals [3] [4]. Besides the usefulness of temperature control in the study of microbes, temperature has a large impact on the growth of mammalian cells, whose

optimal growth range is between 33 and 38°C [5]. It is no surprise, then, that practically any incubator available will have some degree of temperature control. The temperature control range varies by unit, but a typical range is room temperature to 55°C [1].

Besides maintaining temperature and humidity, modern environmental chambers also allow precise control of carbon dioxide (CO_2) and oxygen (O_2) concentrations within the controlled space to better mimic in vivo conditions during incubation. Oxygen concentration is important because growth of mammalian cells requires oxygen concentrations ranging from 1% to 14% [6] to better match the conditions inside a mammalian body, rather than the 20.9% found in Earth's atmosphere [7].

CO_2 concentration does not directly affect the growth of cells, but it is still important for its effect on the pH of the cellular environment. Incubators typically use 5% CO_2 regulating pH levels via a bicarbonate buffer system like that found in mammalian physiology [8]. Dissolved carbon dioxide reacts with water to form carbonic acid (H_2CO_3). The dissociated acid reacts with its conjugate base, bicarbonate (HCO_3^-), to form the equilibrium reaction $H_2CO_3 \leftrightarrow HCO_3^- + H^+$ [8]. The introduction or removal of hydrogen ions (H^+) results in a disturbance in the equilibrium, which stabilizes with a shift to the right or left as necessary, thus maintaining the pH level in the solution. The pH at equilibrium is dependent on the amount of dissolved carbon dioxide, which is dependent on temperature and partial pressure of CO_2 [9], hence the need to maintain a precise concentration of carbon dioxide in the incubator.

Maintaining live samples is only the first step. In order to observe the samples, complex microscopy systems are required. Optical microscopy is a vast category, but it can be somewhat narrowed in the context of biological samples. With opaque subjects, the light source generally needs to be on the same side of the subject as the objective. In this case, incident illumination is generally required, where light is reflected from the surface of the sample into the objective. Typically, this will require an upright microscope with the objective oriented above the sample. On the other hand, with thinly sliced tissue samples or cell cultures, the subject can be backlit so that light is transmitted through the subject and into the objective. This allows an inverted

configuration, where the objective is situated beneath the sample. This can be particularly useful for cell cultures, as the entire culture will be on a single horizontal plane and is thus easily imaged. While useful, this configuration may not be practical for cells on a biosensor apparatus if the device itself is opaque.

Often in biological samples, the sample is transparent and mostly colorless. These samples may not show clearly using transmitted or incident illumination alone, but contrast enhancing techniques can be employed to reveal details in the image. Several techniques are available to increase visibility of features in such subjects. Dark field illumination, Differential Interference Contrast (DIC), and phase contrast serve to increase the feature definition of unstained subjects. Dark field illumination uses a condenser and a light stop so that only scattered light reaches the objective [10]. The result is that "edges, boundaries, and refractive index gradients" are more clearly defined, as can be seen in Figure 1.1.

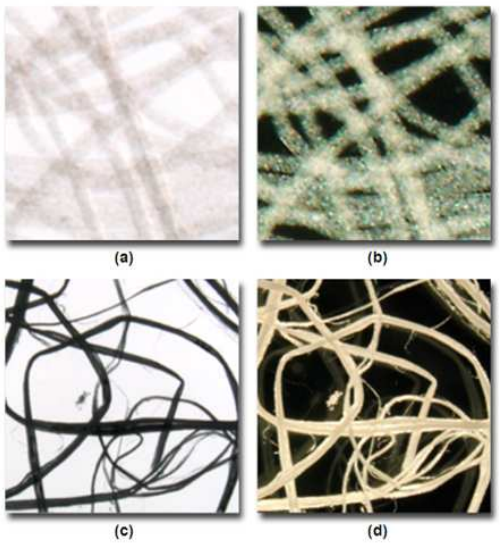

Figure 1.1: Contrast enhancement techniques for nylon fibers with brightfield (a) and darkfield (b) illumination as well as coconut fibers with brightfield(c) and darkfield(d) illumination. Source: [10]

While dark field illumination is good at revealing edges and boundaries, it struggles with internal details. On the other hand, phase contrast and DIC are capable of not only enhancing

contrast of transparent specimens, but subcellular subjects such as nuclei and organelles as well, as can be seen in Figure 1.2.

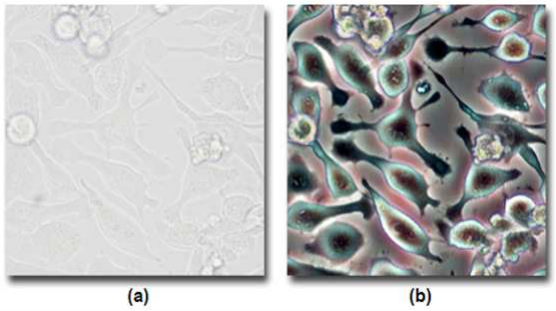

Figure 1.2: human glial brain tissue under brightfield (a) and phase contrast (b) imaging. Source: [11]

While optical contrast enhancing techniques are useful for identifying the physical characteristics of a subject, fluorescence techniques have the capacity to reveal single particle interactions and biological processes. The discovery and development of stains and dyes in the latter half of the 1800's was crucial in "the discovery of many cytological phenomena" [12]. In particular, the discovery and investigation of fluorescence led to the synthesis of uranin, the first fluorescent dye used in animal physiology [12]. The discovery of green fluorescent protein in 1962 and the cloning of its encoding gene in 1992 allowed fluorescent labeling of proteins and tracking expression of the gene throughout an organism [13]. Now, nearly three decades later, a staggering variety of fluorophores are available. Fluorescence has become a vital phenomenon in several techniques useful for live cell imaging. The variety of techniques and applications for fluorescence in biological applications is too great to describe here, but a few examples are warranted. Fluorescence Resonance Energy Transfer (FRET) relies on the proximity of two fluorophores, where the emission band of one corresponds to the excitation band of another [14]. This can be used to detect proximity of two molecules (<10 nm) in a sample, useful for monitoring interactions between tagged proteins or for studying conformational changes within a protein [14]. A combination of nucleic acid staining and fluorescent beads as reference particles were used in [15] with Fluorescence Flow Cytometry (FFC) to count bacteria. Voltage

sensitive fluorescent dyes can even be used to examine electrochemical properties such as the membrane potential around a cell [16]. Traditionally, microscopes are not needed within incubators in terms of storage and incubation. However, with the increasing demand for real-time monitoring of cells during their incubation period to capture real-time changes of cells and cell culture, more advanced instruments have combined incubation and microscopy into a single platform to provide sophisticated analysis of biological cells and cell culture. Sartorius lists over 2700 publications whose studies utilized their IncuCyte live cell imaging systems on research areas including cardiovascular, stem cell, immunology, oncology, and more [17].

Modern environmental control systems have evolved over time from simple storage and incubation to accomplishing more sophisticated cell analysis tasks during incubation using other instruments such as microscopes and biochemical sensors. These advanced capabilities provide holistic analytical solutions to users. As the sophistication of modern incubators improves and more applications are developed, demand is growing. The world market for incubators is projected to have a compound annual growth rate (CAGR) of 6.9% from 2017 to 2025 [18]. Although this growth rate includes the growing segment of incubators for assisted reproductive technology (ART) to meet the increasing demand due to incidents of premature babies and low birth weight of babies, demands for incubators for general medical and biological research and development are still parts of its overall growth trend.

Figure 1.3 shows the composition of the incubator market as of 2018. Although the incubator market is dominated by some of the big medical device players such as GE Healthcare and Fisher Scientific, there are growing number of startups providing innovative solutions to the growing demand for sophisticated cell/culture analysis needs of the future [19]. One of the severe market constraints for further growth of the incubator market as pointed out by [20] is their high cost. This impedes penetration into emerging markets around the world as the healthcare demands in these markets increases faster than the rest of the world in the future. The research described in this thesis addresses this head-on while maintaining most of the essential incubator functionality. Chapter 2 will provide an overview of some of existing incubators on the

market and their advanced features. We also point out the shortcomings of these incubator products to highlight the need for a new type of incubator design.

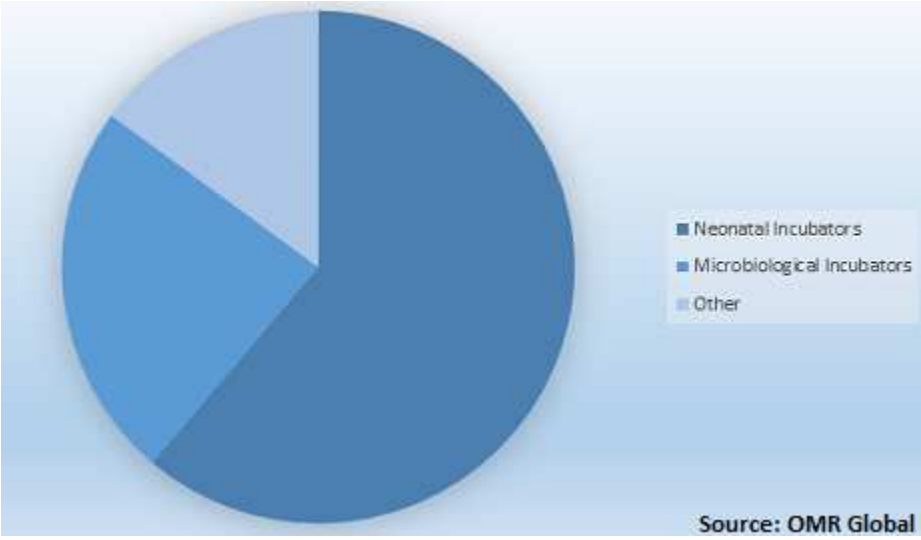

Figure 1.3: Global Incubator Devices Market Share by Product Type, 2018 (%). Source: [20]

With a clear need for a better tradeoff between cost and functionality, following chapters will discuss the engineering behind the proposed incubator design, SBX1, with a tradeoff intended for lower cost while maintaining the functionality needed by a majority of users. Chapter 3 describes the design of the SBX1, including the design of electrical, mechanical and control systems. It also discusses the design of software for the user interface and firmware for the embedded microcontrollers. Chapter 4 discusses the capabilities and limitations of the system. Finally, Chapter 5 concludes the thesis with an overview of what has been accomplished in the development of the SBX1 as well as future work, including desired features and design changes.

Chapter 2

Existing Bioanalysis Chamber Designs

Commercial incubators and imaging systems can be separated into four broad categories:

- Bench-top and Portable Incubators
- Stage-top Incubators
- Microscope Enclosures
- Live Cell Imaging Systems

Additionally, some labs have found available commercial options prohibitively expensive or inadequate and have developed their own research prototypes. The cost, capabilities, and drawbacks of both commercial and custom-built systems are examined here. For consistency, prices and quotes are for systems which have the following environmental control capabilities where possible: temperature control, CO_2/O_2 control, and active or passive humidification. Some systems may require additional accessories to meet these capabilities, e.g., a stage-top chamber in addition to a microscope enclosure for gas control. It should be noted that control accuracy could not be tested or verified for commercial products; capabilities listed are only manufacturer claims. Further, it is not always clear what manufacturer claims refer to, particularly with regards to accuracy specifications. It is assumed that "accuracy" refers to absolute accuracy (i.e., accuracy relative to the true value), unless otherwise noted in system specifications. For example, a specification sheet may list sensor or measurement accuracy as well as control accuracy, at which point the system's absolute accuracy would be the sum of the two.

2.1 Bench-top and Portable Incubators

Bench-top and portable incubators serve only to maintain environmental conditions; they have no imaging capabilities. This necessitates removing the sample from the environment

to observe it. In this category are the K Systems G85, Planer BT37, and Micro Q IQ series incubators. Price estimates in this category range from $3,000 to $12,500 [21] [22]. The Planar BT37 [23], shown in Figure 2.1, is a medium volume bench-top incubator; it has temperature control and accepts pre-mixed gas with an in-line bubbler for humidification. It has capacity for a variety of dishes, including 8x 4 well NUNC dishes, 8x 60 mm petri dishes, or 20x NUNC 30 mm dishes [24]. The K Systems G85 [25], shown in Figure X, has similar capabilities but has a significantly smaller footprint and a correspondingly smaller volume, only accommodating 4x NUNC 4 well dishes or similarly sized dishes, with their associated warming blocks.

(a) Planer BT37. Source: [23].

(b) K Systems G85. Source: [25].

Figure 2.1: The Planer BT37 and K Systems G85 are representative examples of bench-top incubators. They utilize premixed gas passed through a water bubbler for humidification

The environmental control capabilities of these devices are shown in Table 2.1. MicroQ's incubators are portable devices which solely maintain temperature inside a canister. They do not list a control accuracy, nor did conversation with a sales representative reveal one. The system's temperature set-points are in 0.1 °C increments, but control is to the nearest 0.062 5 °C, the minimum error they claim from their sensor [26].Assuming this value is the granularity of the ADC for their temperature sensor and a reasonable accuracy estimate of 0.1 °C for the sensor, we can estimate a system accuracy. If the ADC resolution is 0.062 5 °C, the worst case setpoint

error is given by $\frac{0.0625\,°C}{2} = 0.031\,25\,°C$. This is summed with quantization error to give an error from the setpoint of 0.093 75 °C. With a reasonable sensor accuracy of 0.1°C, this would give an estimated absolute accuracy of about 0.2 °C.

Table 2.1: Capabilities of Surveyed Bench-top and Portable Incubators

Device	**Temperature** (°C)	**Gas Concentration (%)**	**Humidity (%)**
Planer BT37 [24]	Ambient + 5 to 40 ± 0.3	pre-mixed	No % listed, bubbler in line with gas supply
K Systems G85 [25]	Ambient to 42 ± 0.2	pre-mixed	No % listed, bubbler in line with gas supply
Micro Q IQ1 T [27]	2 to 8 9 to 19 20 to 30 ± 0.2 31 to 45	N/A	N/A

Advantages: These devices function well as long term incubators in the case of the BT37 and G85, and as a portable incubator in the case of the Micro Q series. In the case of bench-top incubators, their primary advantage is volume: they can hold multiple well plates, dishes, or tubes. The primary advantage of the Micro Q series is obviously portability.

Disadvantages: The devices have no imaging capability. If the samples need to be observed while in a controlled environment, they must be removed from the incubator. Gas input needs to come from either a third-party mixer or from a pre-mixed source. The primary disadvantage of a portable incubator is battery life. Eventually the capability of the incubator will degrade beyond usability and either the battery or the unit will need to be replaced.

2.2 Stage-top Incubators

Stage-top incubators are compact enclosures, typically large enough to fit a single standard well plate with some additional internal hardware. An example of one such device from Okolab can be seen in Figure 2.2.

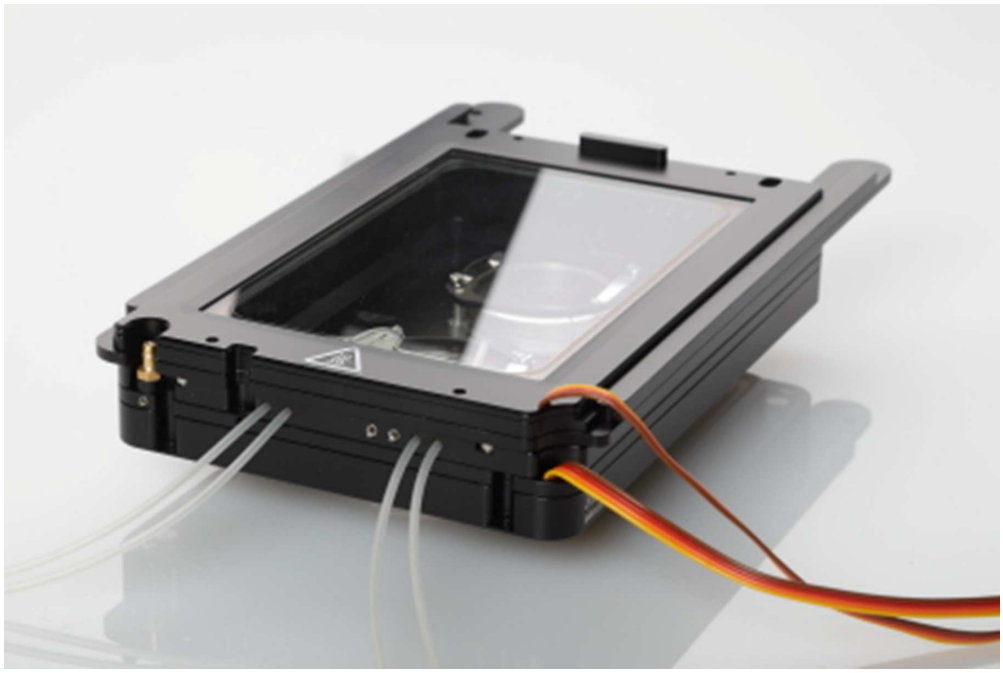

Figure 2.2: Okolab H301-K-Frame stage-top incubator. Source: [28]

Features vary by product, but typically include temperature control via a thermocouple and a plate heater, gas control using a gas mixer or premixed gas, and humidification via a bubbler or internal evaporative reservoirs. A complete system will run upwards of $12,000 [29] [30].

Systems from Okolab, Ibidi, and Tokai Hit were examined as examples of commercial stage-top incubators. Table 2.2 shows the control accuracies claimed by each company for their incubator.

[2]The system has better sample temperature accuracy with the sensor in “sample feedback" vs “chamber feedback” mode. The claim of ± 0.3 °C is dubious: the plot used to demonstrate accuracy shows a delta of 1.2°C and there is no indication of sigma for the stated accuracy. [32]

[2]Tokai Hit did not list an accuracy for gas concentration

Table 2.2: Capabilities of Surveyed Stage-top and Portable Incubators

Device	**Temperature** (°C)	CO_2 **(%)**	O_2 **(%)**	**Humidity (%)**
Okolab Stage-Top Incubator System [31] [32] [33]	Ambient + 3 to 60 ± 0.1\± 0.3[1]	0 to 10 ± 0.1 0 to 18 ± 0.1 0 to 20 ± 0.1	0 to 20 ± 0.1 1 to 20 ± 0.1 1 to 95 ± 0.1 0 to 1 ± 0.1	50 to 95 ± 1
Ibidi Stage-Top Incubator System [34] [35]	Ambient to 45 ± 0.2	0-15 ± (0.2 + 3% of reading)	1 to 21 ± 0.2	20 to 99 ± 2.5
Tokai Hit STX Series [36] [37][2]	30 to 40 ± 0.1	5-20	0.1 to 18	> 95

The enclosures from each company have similar capabilities, but there are some differences in implementation or additional features. The Okolab and Ibidi systems use an active humidifier on the gas inlet; whereas the Tokai Hit enclosure has a heated bath [37] [33] [30]. All three systems require inserts to fit microplates, slides, or petri dishes, and may require proprietary dishes or plates as well [30] [29] [36]. Stage adapters are also required [30] [36] [38]. All three companies use a thermocouple either in air or inserted into a reference well for temperature control [35] [32] [37]. This brings accuracy claims into question. Thermocouples are relatively inaccurate; typically around of ± 0.5°C for "special limits of error" thermocouples [39]. It is possible that the probes are calibrated individually with each box, which might allow greater accuracy, potentially as good as 0.1°C. The accuracy of a thermocouple-based sensor also depends on the precision of the cold junction compensation to ensure an accurate delta is measured [40]. While accuracy claims of commercial products may be in doubt, it is unlikely that it is truly an issue. An accuracy of 0.5 °C is at the edge of tolerance for incubation [22].

Advantages: If a lab already has a microscope system which meets their needs, this may be a good solution to accompany it. The small volume of the chamber allows for responsive temperature control.

Disadvantages: A smaller chamber is also more susceptible to large environmental disturbances such as an abrupt change in ambient temperature. The chambers must match the microscope stage it will be used with. Additionally, the volume does not readily accommodate other devices or more complex microfluidic arrangements: the setup is restricted to the perfusion ports made available on the chamber. Finally, space is restricted to one well plate or similarly sized arrangement of dishes. If multiple dishes or plates need to be incubated, either a standalone incubator or multiple stage-top incubators are necessary.

2.3 Microscope Enclosures

Enclosures for a traditional microscope setup may be appealing to a lab if they already have a quality microscope but need to do live cell imaging. Commercial products in this category are the Okolab Bold Line enclosure, Digital Pixel Microscope Incubation Chamber, and World Precision Instruments (WPI) Environmental Control Unit. While other models exist, these appear to be representative of the market.

These enclosures must be purchased to match a make and model of microscope. Prices run upwards of $19,900 [29] [41] for units with O_2/CO_2 and temperature control. Temperature control is typically accurate to within ± 0.1-0.3 °C. Gas control is possible but requires additional stage-top chambers for all but Digital Pixel's "SuperSeal" model, which is only available for Zeiss microscopes at this time [42]. Humidification of the environment is less consistent. Okolab's enclosures have a passive humidifier available for the enclosure, or active control for a stage-top chamber [43]. The WPI enclosure has an optional manually adjustable humidifier module for an additional $1000 [41], while the Digital Pixel enclosure does not include an option for humidification [42]. Figure X shows enclosures produced by Digital Pixel and Okolab as examples typical enclosure designs. Characteristics of offerings from each company are summarized in Table 2.3.

Advantages: Enclosures are built for existing microscopes, so a lab need not purchase additional optics, only the enclosure and its associated components. A full enclosure allows man-

Table 2.3: Capabilities of Surveyed Microscope Enclosures

Device	**Temperature** (°C)	CO_2 **(%)**	O_2 **(%)**
World Precision Instruments [41] [44]	ambient to 45 ± 0.1 at the sensor ± 0.2 across the stage	0 to 20 ± 3	0 : ambient ± 0.5
Digital Pixel [45]	Ambient + 1 to 42 ± 0.3 at the sensor ± 0.3 across the stage	0 to 10	0 to 21
Okolab [29] [43]	Ambient + 3 to 45 ± 0.1 at the sample	0 to 10 ± 0.1 0 to 18 ± 0.1 0 to 20 ± 0.1	0 to 20 ± 0.1 1 to 20 ± 0.1 1 to 95 ± 0.1 0 to 1 ± 0.1

ual manipulation of a sample while maintaining the environment around it. There may also be room for other apparatuses such as a more complicated electrochemical sensor systems or more complex microfluidics arrangements that could not fit in a stage-top enclosure. A larger volume makes the system more resistant to external disturbances. In combination with a stage-top incubator, the enclosure can act as a buffer to help the smaller incubator maintain homeostasis. Configuration of these systems is generally as simple as entering a target parameter and waiting for the system to stabilize. Most systems are simple control units, but the Okolab system has an "Smart Box" accessory which provides data logging and remote access to the system [43].

Disadvantages: If gas control is required for the full enclosure, it will necessitate a larger flow rate from gas supplies and thus a higher cost to run the system. In addition to the cost for air, the power requirements for heating increase with the larger volume. Digital Pixel does not offer humidification for the enclosure, although users could place distilled water baths inside the enclosure to raise the humidity within the chamber. Finally, while these enclosures are among the less expensive options provided a suitable microscope is already available, $12,000 is still a large investment for environmental control.

2.4 Live Cell Imaging Systems

Several devices fall into this category. Those examined for comparison are the Zeiss Celldiscoverer 7, Keyence BZ-X800E, Thermo Fisher Evos M7000, and Sartorius IncuCyte S3. These are devices with sophisticated imaging systems and advanced computer vision algorithms. Cost and capability vary between the systems, but all include fluorescence microscopy capabilities, computer vision and automation algorithms to generate and analyze high quality imagery, and automation for streamlining large processes.

The IncuCyte S3, shown in Figure 2.3 differs from the other three in that it is targeted more at volume analysis with a capacity for six fixtures which can hold well plates, dishes, or flasks [46]. The other three systems only allow for a single fixture for plates, slides, or dishes. Further, rather than moving the sample only the optical system moves, allowing samples to remain stationary inside an incubator during analysis, but its imaging capabilities are less than the other systems.

Figure 2.3: The Keyence BZ-X800E, an example of a mid-range live cell imaging system. Source: [47]

All except the IncuCyte system include Z-stacking, which allows the composition of 3D images of the subject through techniques such as confocal scanning laser microscopy or structured illumination. To achieve this, each product uses different techniques. The BZ-X800E, shown in Figure X, uses an optical sectioning technique with co-axial illumination [[48]8]. Zeiss Celldiscoverer 7, shown in Figure X, uses software deconvolution similar to the BZ-X800E, but may also utilize confocal Scanning Laser Microscopy (CSLM) using their AiryScan system [48] [49] [50]. It is unclear what method the M7000 uses, but they do advertise a Z-stacking capability and the size of the unit suggests a method other than CSLM [51] [51]. Each of these systems also include stitching algorithms, to produce images spanning areas larger than the field of view of the objective [49] [51] [52].

Fluorescence microscopy is common in biological research microscopes and is a key feature of these devices. The Celldiscoverer 7 uses up to 7 configurable LED modules for illumination, allowing the user to customize their excitation spectra [50]. Like the Zeiss system, the M7000 uses LED based light cubes, which have good spectral matches for a large variety of fluorophores [47]. The BZ-X800E microscope utilizes a broad-spectrum metal halide lamp and uses Chroma brand filter cubes to restrict the emission band [48]. The IncuCyte system is more restrictive in terms of excitation bands. It comes in two flavors: S3 and S3 Neuro. The S3 version has an excitation band of 440-480nm with a green source and 565-605nm with a red source [53]. The neuroscience variant uses an orange source for 513-568nm excitation, and a near infrared source for 658-674nm [54].

Options for environmental control vary by system: the IncuCyte S3 is designed to be placed entirely inside a large incubator [46]. The Evos M7000 and Keyence BZ-X800E systems are compatible with stage-top incubators but do not have integrated environmental regulation [52]. [51] Of the four imagers examined, only the Celldiscoverer 7's environmental control is internal to the system. Zeiss has partnered with Pecon GmbH for environmental control [50]. The Pecon controller for CO_2/O_2 is an automated gas mixer can provide 0-20.0% CO_2 and 20.8-0.1%O2, ± 2% of setpoint [55]. For temperature, the setpoint range is 0-60°C and they claim a typical

loop control accuracy of ± (0.15 * setpoint)% of the setpoint. These are by far the most expensive imaging option. Quotes were obtained for each system, ranging from $80,000 to $180,000 except for Zeiss's system, which stands out at $200,000 to $500,000 depending on the configuration [50] [56] [57] [58].

Advantages: Systems may be tailored to fit the imaging needs of a lab, including multiple illumination configurations and CSLM capabilities. Software is capable of a range of functions such as autofocus, Z stacking, image stitching, motion analysis, image cytometry, and more [52] [49]. With significant funding and experienced engineers behind the products, the hardware can be expected to be well built and reliable, with good support from the manufacturer.

Disadvantages: These systems have staggering costs, making them unaffordable unless a lab is particularly well funded or multiple labs pool resources. Of the systems surveyed, only the Zeiss system has integrated environmental control [50]. The M7000 and BZ-X800E can provide incubation via an external environmental controller with a stage-top incubator [52] [51], while the IncuCyte system must be placed entirely within a cabinet style incubator [46]. Additionally, they invariably use inverted microscopes, which is likely enough for most biological applications but not all, for example when the sample rests on an opaque surface such as a biosensor.

2.5 Review of Research Prototypes

An alternative to commercial imaging systems is for a lab to build their own microscope at a fraction of the cost of the previously examined live cell imaging systems. One strategy for building a reasonably high-quality microscope without special skills or equipment is to use à la carte commercial optical components, such as the Flexiscope. Another is to build a system entirely from scratch, such as the one designed by Walzik et. al.

The Flexiscope, shown in Figure 2.4, uses a combination of commercial and 3D printed components and can be arranged in one of three configurations: upright, upright/electrophysiology, or inverted. It is capable of "automated stage scanning; visualization of unstained tissue and

sub-micrometre computer-controlled micromanipulation" [59]. The device is constructed from a combination of commercially available and 3D printed parts, and uses Matlab or Python for control and image processing [59]. The microscope's primary advantages are in its relatively low cost and versatility. It has multiple configurations, can be easily modified, and has a cost of cost of around 17,810.17€ or about $19,250 at the time of publication [59]. This allows a lab to purchase one set of components to meet multiple requirements, rather than purchasing multiple commercial microscopes.

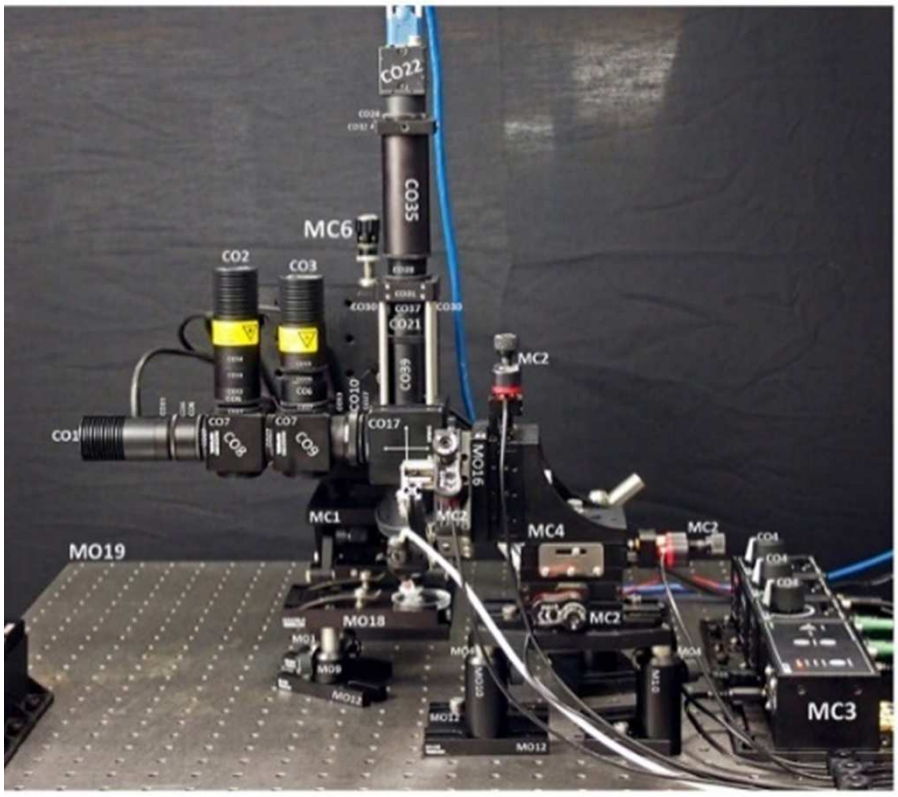

Figure 2.4: The Flexiscope, a custom microscope made from commercial and 3D printed parts. It can be arranged in an upright or inverted configuration. Source: [59].

The assembly touts many of the same features as expensive commercial products, including Z-stacking, fluorescence microscopy, stitching, and a piezoelectric stage for nanometer scale adjustments. For larger scale adjustments, it can also use stepper motors to drive the linear stage [59]. One drawback is that commercial stages only have 13-25.4mm of travel, depending

on the configuration [59]. This is insufficient for observing a well plate or a 100 mm petri dish; though it is certainly adequate for slides.

The Flexiscope, while remarkably capable, lacks environmental control and is relatively large. In addition, while $18,000-$20,000 may be less expensive than a comparative commercial device it is still a significant investment. On the other hand, the device designed by Walzik et al., shown in Figure 2.5, is a compact device with a footprint of only 12x12cm, and a parts cost of less than €1,250 ($1,525) [60].

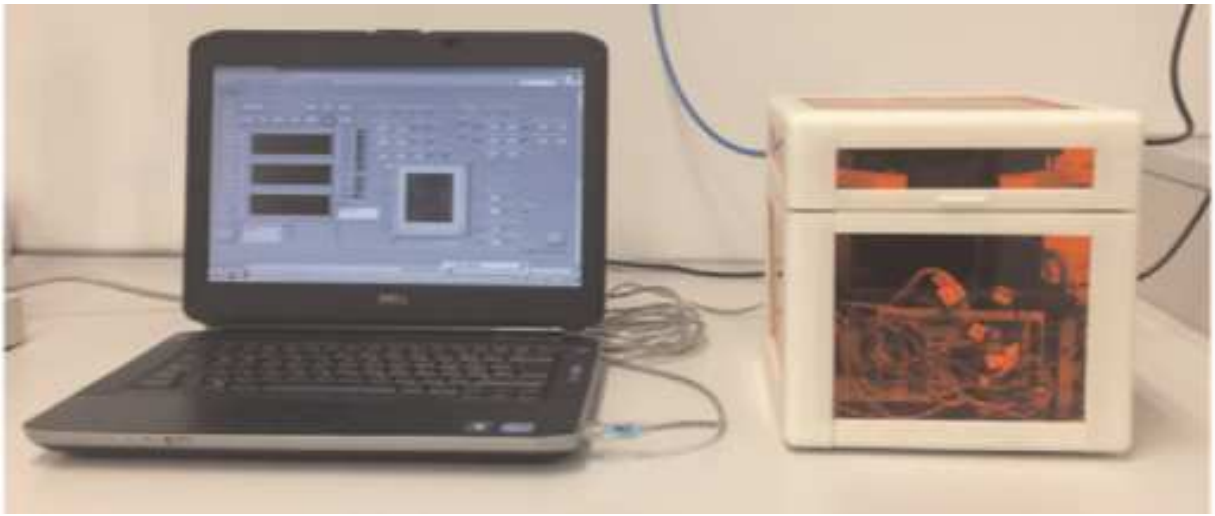

Figure 2.5: The low cost environmentally controlled chamber by Walzik et al. provides environmental control as well as some automation for its integrated microscope. Source: Adapted from [60]

The chamber uses a modified USB microscope for imaging and two sets of white LEDs for illumination: one configured for bright field and 4 for dark field [60]. It does not have fluorescence capabilities, but it could be modified to include single color high power LEDs for such a purpose. Humidification is accomplished with reservoirs in the chamber and reaches 70-80% after two hours [60]. It is apparent from the plots in [60] that both CO_2 concentration and temperature are controlled using hysteresis, with temperature controlled to ± 0.6°C and CO_2 concentration controlled to ± 1.1% [60]. With the camera mounted on an XY gantry, the device is capable of stitching; however, it does not have a Z axis motor. Rather it appears to use

a fixed focus camera, relying on a constant distance from the subject to the objective. Further, the image is cropped so that the usable area of the sensor is 700x700 pixels [60].

Advantages: Purchasing commercial components to build a custom microscope has a better potential for support than a fully custom design, provided the parts are not discontinued. Modifications are more feasible, and less daunting because a mistake isn't nearly as expensive in terms of money if not time. A fully custom fabricated design is even less expensive, potentially even allowing multiple enclosures for a single lab.

Disadvantages: As with the choice with a manufactured imaging system, you pay for quality and convenience. While less expensive than commercial imaging systems, the Flexiscope still amounts to a significant investment in parts. Moreover, those parts will be more susceptible to wear and tear as the device is transitioned between configurations. The Walzik device is very affordable but requires more technical and mechanical ability to assemble and use. For either device, the imaging, automation, and computer vision capabilities are reliant on the tools and techniques of the lab building the system and programming the software, which are not typically skills associated with a biomedical degree.

2.6 Need for a New Breed of Smart Bioanalysis Chamber

Commercially available products are certainly feature rich and companies are willing to work with customers to build a system that meets their needs. Purchasing a commercial device will provide device support and make available technical resources. However, commercial live cell imaging solutions have some drawbacks. The largest is cost; even with institutional discounts, prices can be prohibitive, especially for underfunded labs. Even if the price barrier is overcome, systems may not meet all requirements. Stage-top incubators have a relatively small volume, with little room for third party devices and limited access for microfluidics. Cage incubators generally provide temperature and possibly humidity control, but typically require an additional stage-top incubator to maintain gas concentration; although this could also be a benefit, minimizing the gas required to maintain homeostasis. One option to avoid these costs

is for a lab to design their own system to their specifications, or to find an open-source design which meets their needs.

The main benefits of "DIY" systems are lower cost and design flexibility, but those benefits have costs in time and potentially quality depending on the design and the skills of the builder. Additionally, support for projects may be lacking: The project may have a small or uninvolved community, developers may move on to other projects, and graduate students don't stay forever. One example is the Cambridge Labs Open Microscope, whose web site is now largely defunct and contains no information regarding the function or design of the microscope (although it is still accessible through the "Wayback Machine" Internet Archive) [61]. With these issues in mind, the needs of a new comprehensive bioanalysis chamber are developed. A chamber which combines the advantages of commercial imaging systems, cage incubators, and stage-top incubators, and has a price comparable to DIY solutions. It should also minimize the downsides of each of these categories to the extent possible.

The imaging system should include a motorized gantry with motion in X, Y, and Z axes. This is necessary for features such as autofocus, Z-stacking, and stitching, and automation routines such as multi-well time-lapse. Dark field imaging is desirable but not strictly required. The optical system should be configurable for both upright and inverted positions to accommodate a variety of microscopy needs. It is also apparent that fluorescence microscopy is a vital aspect of modern biological research, and thus the device should include fluorescence illumination compatible with a large selection of fluorophores. Finally, there should be an integrated camera with a still image resolution of 2MP images and 1080(p/i) video.

The stage should accommodate a standard well plate or petri dish, as well as non-standard subjects without significant investment. Ideally there would also be room for incubating multiple dishes/wells simultaneously without the need for a second incubator. The stage volume should allow tall objects to be placed under the objective, should be able to support several pounds without significant deflection in order to accommodate custom designed apparatuses. There should also be access from outside the box for microfluidics, power, and data cables for

external equipment to access the stage without compromising the environmental integrity of the chamber.

Environmental control should be integrated with the enclosure. Temperature control is necessary in the range of ambient to 40 with absolute accuracy of ± 0.3°C. Gas control should include O_2 from 20%-0%, and CO_2 from 0-20%. Relative humidity does not need to be actively controlled, but there should be some mechanism for humidification of the environment to minimize media evaporation or sample dehydration. Software should be intuitive and easy to use, both for manual control as well as automated tasks. It should have a data logging mechanism which can store environmental data alongside images and video. Some sort of network connectivity may be desirable for a video feed, remote access, control, notifications, et cetera.

Chapter 3

Design of the SBX1 Chamber

The environment chamber, tentatively dubbed SBX1, is a complex system. It is best considered in terms of interrelated mechanical, optical, electrical, and software design units. The mechanical design consists of the environmental enclosure and the microscope assembly. Optical design refers to the design of the microscope optics and illumination. The electrical system handles power and signal distribution throughout the box. It drives the motorized microscope gantry, controls microscope lighting, and facilitates communication with the environmental sensors and controls. Finally, software and firmware reside physically in the electrical subsystem but can be considered a separate design domain. Software provides a user interface for the SBX1 chamber and communicates with the microcontrollers. Firmware resides on two microcontrollers, which manage the system functions and provide system status to the user interface. One is responsible for driving the X, Y and Z axis motors of the microscope gantry. The other is responsible for managing the sensors and the environmental control system.

The primary objective of the SBX1 chamber is to provide a low-cost option that can satisfy most use cases in biological sensing and imaging applications. This overarching goal necessitates a few major constraints. Suitability for biological experiments drives the system specifications. The system must meet environmental control requirements including temperature control to at least 40 °C ± 0.2 °C, CO_2 concentration from 0 to 5% ±0.5%, O_2 concentration from 0 to 20% ±0.5%, and relative humidity maintained at 85% ±5%. The device also needs to include a small incubator drawer which can hold well plates and petri dishes. In addition to maintaining a suitable environment for live cell experiments, a live-cell imaging system is necessary, to include a microscope with fluorescence capability. A motorized microscope is necessary to position and focus the sample, as well as to enable features such as autofocus, image stitching, and Z stacking.

3.1 Microscope Design

The microscope lies at the heart of the SBX1 chamber. It enables a user to image samples without opening the chamber and disturbing the environment. It also makes possible automation features such as image stitching, Z stacking, autofocus, and time-lapse imaging. It consists of four subassemblies, shown in Figure 3.1. The Stage holds samples in place for observation and aligns well plates with the XY axis. The Stage Actuator provides X and Y travel for the stage, while the Z actuator is responsible for microscope focus. The optics assembly provides magnification of the subject and camera capture capability. Finally, the light ring provides illumination for the subject.

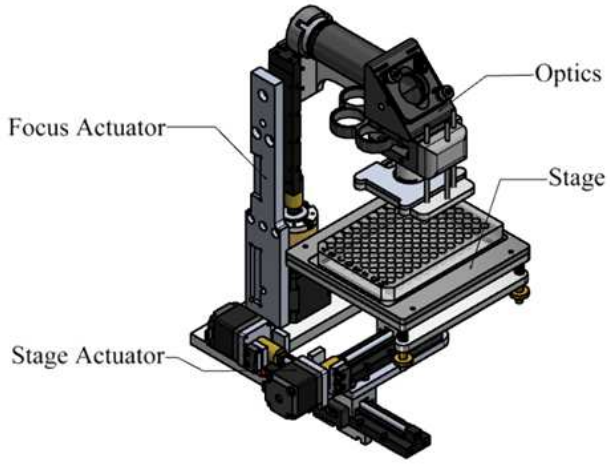

Figure 3.1: The microscope assembly consists of four subassemblies: Focus Actuator, Stage Actuator, Optics, and Stage.

3.1.1 Actuators

The Stage Actuator subassembly, shown in Figure 3.2, provides X and Y travel for the microscope stage. It has four subassemblies. The base plate is the supporting structure for the whole microscope and includes mount holes for securing the microscope to the environment chamber base. The Y actuator mounts to the base plate. The X Actuator Mount Plate affixes to the Y actuator's carriage, and the X actuator affixes to the mount plate.

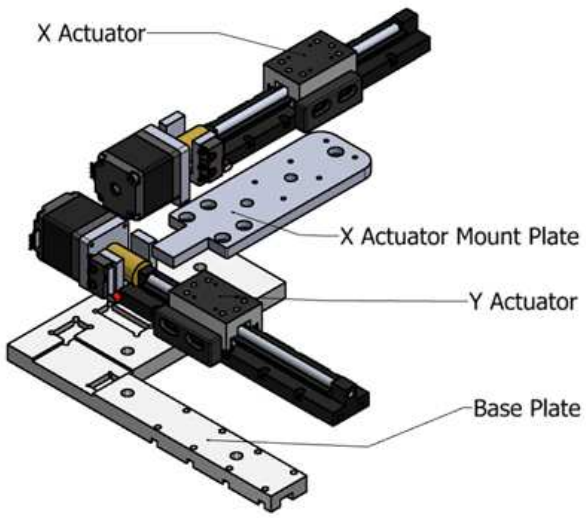

Figure 3.2: The Stage actuator consists of an X and Y actuator joined by a mounting plate, and attached to the microscope's base plate.

The X and Y Actuators are nearly identical except for mounting brackets, so only the X actuator is shown in exploded view in Figure 3.3. Each actuator uses a Misumi XTSC-150-5 linear guide coupled to an 11HS12-0674S NEMA 11 motor. These guides have a travel of 150 mm and a lead of 5 mm/revolution. The X and Y motor drivers are configured to use $\frac{1}{16}$ microsteps, and the motors have a 1.8° rotation per step. Combined, this information can be used to calculate a theoretical linear travel of 1.5625 um/microstep.

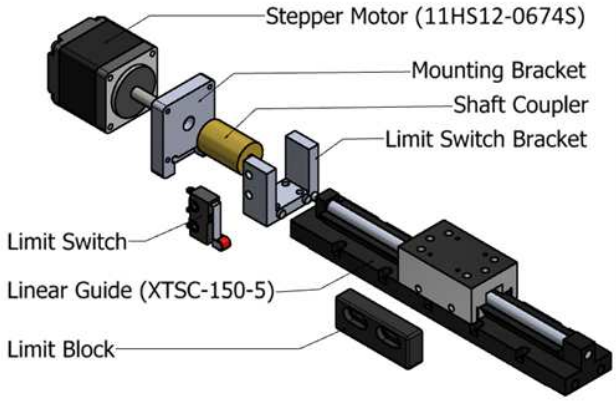

Figure 3.3: X actuator exploded view.

The Z axis, shown in Figure 3.4, uses an XTSC-120-5 linear guide and a 17HS19-1684S-PG27 NEMA 17 stepper motor. This linear guide has a travel of 120 mm and a lead of 5 mm/revolution. Like the 11HS12-0674S, this motor has a 1.8-degree rotation per step, but also comes equipped with a 27:1 planetary gearbox. This significantly reduces vertical travel per step to provide the movement resolution necessary for focusing on microscopic samples. In practice, the travel rate with $\frac{1}{16}$ microsteps was too slow, so the microstep size was increased to ¼ step, resulting in 0.232 $\frac{\mu m}{\mu step}$ for the Z axis. The addition of the planetary gearbox improves the step resolution of the Z axis, but it also amplifies backlash, necessitating algorithmic backlash correction for automated tasks.

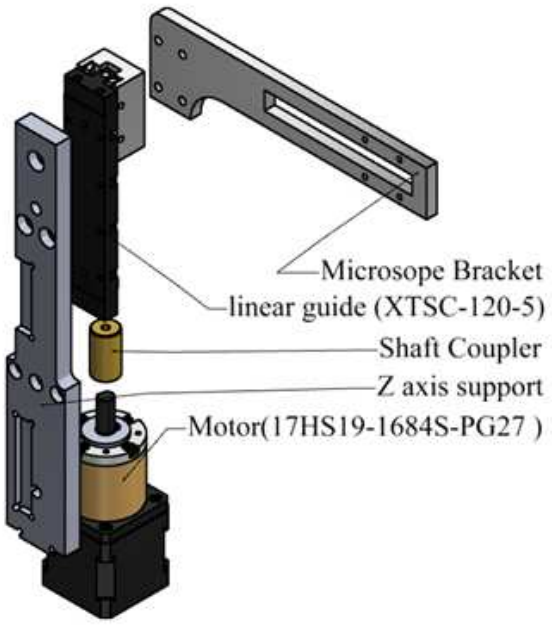

Figure 3.4: Focus Actuator components exploded view. Provides vertical movement of the optics to adjust focus.

Each axis also has a limit switch at the 0 position for each axis. This provides a system origin with the stage in the front left and the microscope in the lowered position. The limit switches are used only for determining system origin for absolute positioning; They do not provide collision prevention. Avoiding collision requires software checks to prevent stepping beyond the travel

range of each axis. These checks are handled in the GUI software, as the motor microcontroller will accept any movement commands provided to ensure smooth movement.

3.1.2 Optics

The optical chain of the microscope is built from off-the-shelf components. An exploded view of the assembly in Figure 3.5 shows each component. While customers may supply their own objectives, those supplied with the microscope are 4x/0.10, 10x/0.25, or 20x/0.40 160/0.17mm lenses from the Amscope AX-6-V300 objective set. This range of magnification is sufficient for viewing samples down to approximately 5-10 microns. This is adequate for viewing biological samples such as oocytes and stem cells, particularly if it is not necessary to observe organelles. Above the objective is a 6-position filter wheel, which houses 25.4 mm filters used in conjunction with the single-color LEDs for fluorescence illumination. Above the filter wheel is a 45-degree mirror which redirects the optical path horizontally onto the Pi Camera V2. The bend in the path reduces the height required for the microscope assembly, helping keep the SBX1 volume low. The Raspberry Pi camera connects to the end of the tube using a custom housing.

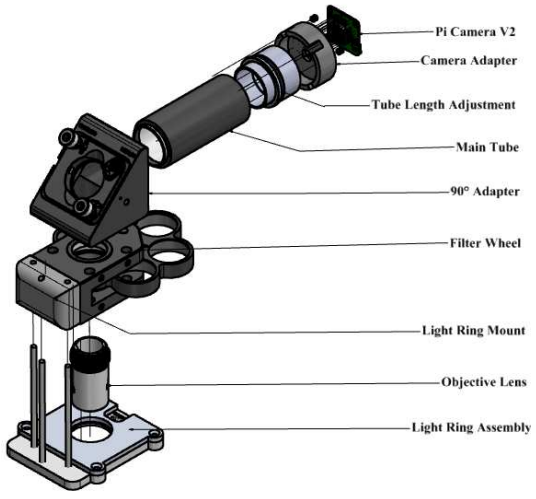

Figure 3.5: Optical path components, including the camera, tubes and mirror, filter wheel, and objective lens.

The ring light subassembly is illustrated as an exploded view in Figure 3.6. The mount block attaches to the filter wheel. The ring mount has three aluminum rods secured to its front which are slightly bent away from each other. These rods fit into the holes in the mount block, and friction with the block holds the assembly in place, allowing the user to freely position the light to match the objective height without having to adjust any screws or knobs. It also allows the mount to slide up in the event of a collision with the stage, rather than damaging the light or the stage. The ring light is affixed to the ring mount, and the heat sink is affixed to the back of the ring light using a silicone thermal pad. The ring light provides both white and single-color illumination.

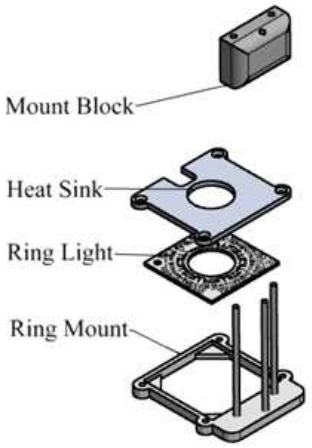

Figure 3.6: Optical path components, including the camera, tubes and mirror, filter wheel, and objective lens.

3.1.3 Stage

The payload of the stage determined its dimensions. The original specification for the stage was to hold one of the lab's 100 mm x 100 mm smart well devices or a 100 mm well plate, thus the stage was only a 101.6 mm x 101.6 mm (4in x 4in) acrylic sheet. This size is inadequate for well plates, and it also has mounting screws which interfere with smaller samples. A new design has been modeled in CAD, but has not been prototyped, as the next version will likely use a commercial stage due to insufficient machining capabilities at BLISS Labs. The new version,

shown in Figure 3.7, enables securely seating well plates, petri dishes, slides, or other samples by exchanging easily removed adapter plates. The plate shown in the figure is a standard 96 well plate. The well plate is secured in an adapter plate, which screws onto the level plate. This plate is leveled using a leveling assembly, consisting of three screws situated about the center of the leveling plate. They can be adjusted to ensure that the level plate is normal to the optical axis by using the leveling nuts to compress or decompress the leveling springs. The standoff block at the bottom raises the top of the stage assembly to the height of the enclosure's access door.

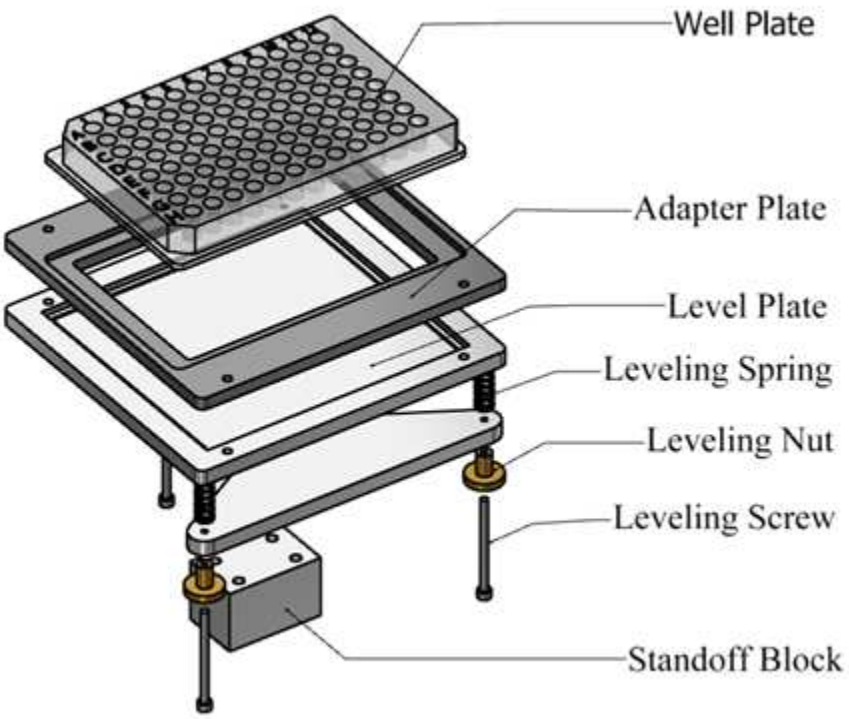

Figure 3.7: Stage assembly exploded view

3.2 Enclosure Design

The SBX1 is a complex interconnection of multiple systems. It is difficult to describe the design of one aspect without tying in another. The enclosure consists of three distinct layers, highlighted in Figure 3.8. The upper layer is the microscope enclosure, which houses the mi-

croscope and samples under study. The middle layer houses the air exchanger, responsible for maintaining the environment within the SBX1. It also contains the incubator drawer for longer term storage of samples. The bottom layer houses the electronics and provides connection points for power and peripherals such as a monitor, mouse, keyboard, and external storage devices.

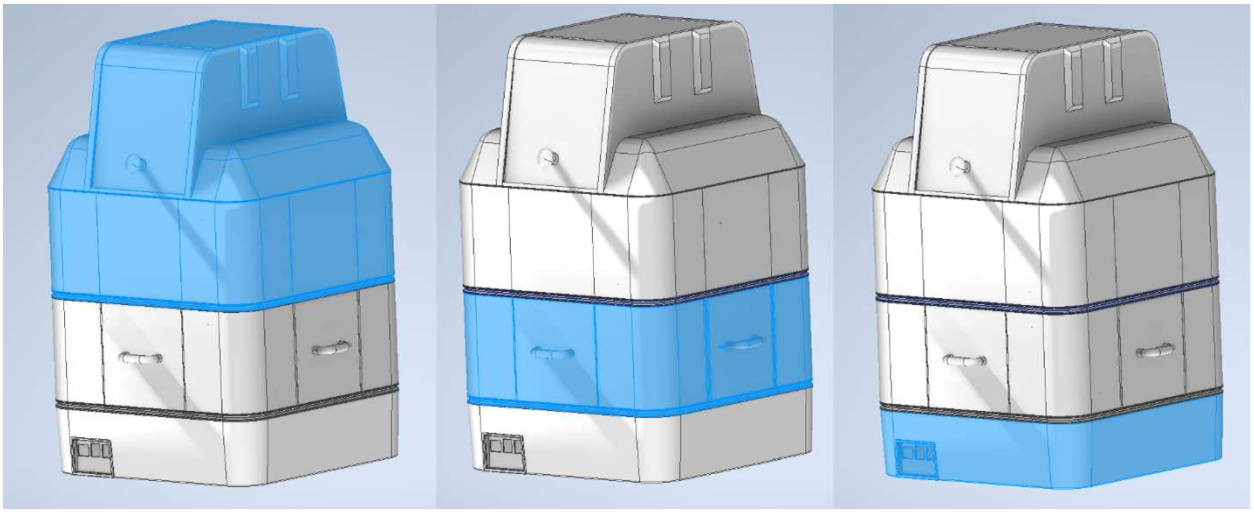

Figure 3.8: Major sections of the SBX1. From left to right: Microscope enclosure, air exchanger, electronics enclosure.

3.2.1 Dimensions

The dimensions of the box are driven by utility and function. The height and footprint of the box should be minimized to reduce the space taken in a lab. To facilitate environmental control, the volume and surface area of the controlled environment should be minimized. The minimal dimensions of the box are largely determined by the microscope and its requirements. The stage must move to place each well of a standard well plate under the objective lens, and it must be able to image the entirety of a 100 mm diameter petri dish. The larger of the two is the lengthwise distance between wells of 108 mm. Twice this dimension (216 mm) is the minimum square footprint of the stage, including its movement extents.

The height of the upper chamber is constrained by the clearance of the microscope from the stage. The largest device allowed to be on the stage would sit at approximately three inches high, so the gantry was designed with an extra inch above that for focus and positioning. The height of the middle section was largely determined by the size of the heat sink for the heat exchanger unit, 4 inches tall. Finally, the bottom section height needed to be tall enough to house the power supply as well as allow air flow over the electronics for cooling. The final design has a footprint of 12.77 in x 12.77 in and is 23 in tall. In the air exchanger, height was driven by the 4in. x 4in. heat sinks for the heat exchanger. In the electronics enclosure, the minimum height was constrained by the cross-sectional air flow required for cooling the power supply. The power supply's air intake was approximated as a circle with a diameter of 60 mm, or an area of 188.5 mm^2. This determined the size of the air duct, which maintains the cross-sectional area of the power supply fan intake to ensure adequate airflow. This means that the air intake for the air duct in the electronics enclosure must have a minimum height of 60/pi is 60 mm x 20.32 mm, for an area of 1 219.2 mm^2 which determined the minimum height of the duct section of the electronics enclosure.

3.2.2 Housing Design

The primary design considerations for the enclosure are cost, size, and thermal efficiency. Cost is mitigated primarily by minimizing size and using efficient manufacturing techniques such as injection molding. The size of the chamber "falls out" from a desire to minimize the size of the device. A smaller device will cost less, be more thermally efficient, and take up less space in a user's lab.

Thermal efficiency is related to construction materials, enclosure volume, surface area, and insulating techniques. The first consideration is construction material. A material with lower thermal conductivity will function to better retain heat inside the device. In general, plastics have reasonably low thermal conductivities, on the order of 0.2 W/°C [62]. For this reason, the obvious choice was made to design the box out of plastic. But not any plastic will do, it must

be resistant to UV degradation, chemicals, and temperatures typical of sterilization. The first prototype was made out of ABS, as it was a cheap option for a prototype that didn't need to last but had thermal properties typical of similar plastics. Future prototypes will be made from materials which can withstand UV and NO2 based sterilization, as these are viable methods for room temperature sterilization of the internal chamber surfaces.

While plastic has a low thermal conductivity, atmospheric air is lower by an order of magnitude. This led to a decision to use a double-walled design, with an air gap between each wall. This increases the thermal resistance of the walls, as does reducing the surface area of the enclosure.

Finally, because thermal resistance is proportional to the area exposed to a temperature differential, the internal surface area of the box is minimized to the extent possible. The internal volume also relates to efficiency and is minimized, but for a different reason. The volume of air dictates the thermal mass which must be maintained at the temperature set point, thus a lower volume will require less heat pumped into the box to maintain the target temperature. Even with a relatively small size for the SBX1, manufacturing costs are a concern. One way to minimize cost for manufacturing is to use injection molding. With this process, Initial costs for molds are high (in the range of $75,000 to $150,000 for a complete set). However, once production has begun the BOM cost for an enclosure would be only $50-$100. By comparison, a 3D printed prototype cost $1200. For any significantly large volume of production (over 100 or so units), injection molding is clearly more cost effective.

While the cost benefits are clear, design for moldability is more difficult than design for 3D printed parts. Careful consideration for the geometries of each part must be taken to ensure manufacturability and to minimize mold costs. A draft angle is required on any side walls to promote mold ejection. The type of plastic and the smoothness of the surface determine the draft angle required. A minimum draft angle of 2 degrees was used; however, most surfaces exceed this minimum.

Additionally, the mold cost is related to the volume of the cavity that must be created: deep parts will be significantly more expensive than shallow ones. For this reason, parts were designed to have minimal depth, thus minimizing the depth of the cavity required. Another way to minimize mold cost is to simply minimize the number of molds required. Figure 3.9 is a prime example of these principles.

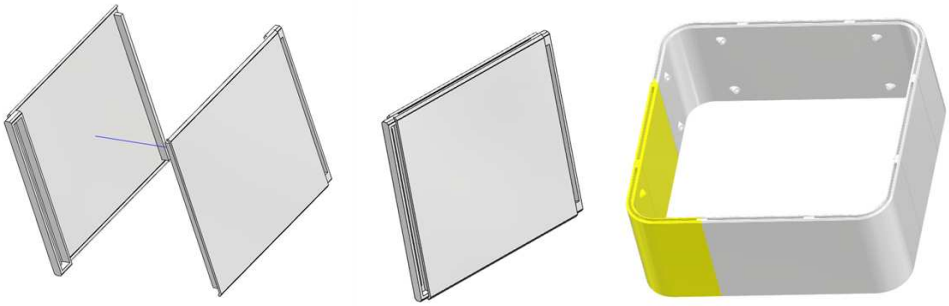

(a) Two wall halves **(b)** Wall Section **(c)** Full Wall

Figure 3.9: An example of injection mold design, showing how part reuse and flat components are used to keep mold costs down. Identical parts are joined together to form the straight wall sections, which mate with corner sections to form a completed wall.

The straight wall sections are formed by mating two copies of the same part, shown in Figure 3.9a. The left and right sides of the halves mate to form a completed hollow wall segment with slotted tab, as seen in Figure 3.9b. The slot in the tab mates with protrusions internal to the corner sections. Another feature which facilitates a reduced part count is symmetry. Except for the electronics enclosure, the box also has mirror symmetry down the center plane and significant radial symmetry as well, so that parts on the left and right side are identical, as are many of the parts in each quadrant of the box. An example of part reuse is shown in Figure 12, where a highlighted corner wall and side wall are reused four times to form the complete lower wall for the microscope enclosure as in Figure 3.9c.

3.2.3 Air Exchanger

The air exchanger houses the control mechanisms for each environment variable: water baths for humidity, a heat exchanger for temperature, and solenoid valves for gas concentration. To maintain a homogeneous internal environment, it is necessary to mix the air within the chamber. This is accomplished using an internal fan with a high flow rate and a controlled path for air within the box. Air is drawn in from the environment chamber via an inlet beneath the microscope stage. In the air exchanger, A 110 cubic feet/minute fan forces the air across the inner heat sink of the heat exchanger to heat the air. From there, the path splits into two symmetrical paths on the left and right half of the box. Each path has two branches. One is directly into the upper chamber. The other branch traverses over a water well to humidify the air, then up to the microscope enclosure through the forward corner, whence it is drawn across the stage and back into the intake to repeat the path. In the current design, gas mixing is asymmetrical, with inlets into the chamber in the forward right corner. The air flow within the box is illustrated in Figure 3.10

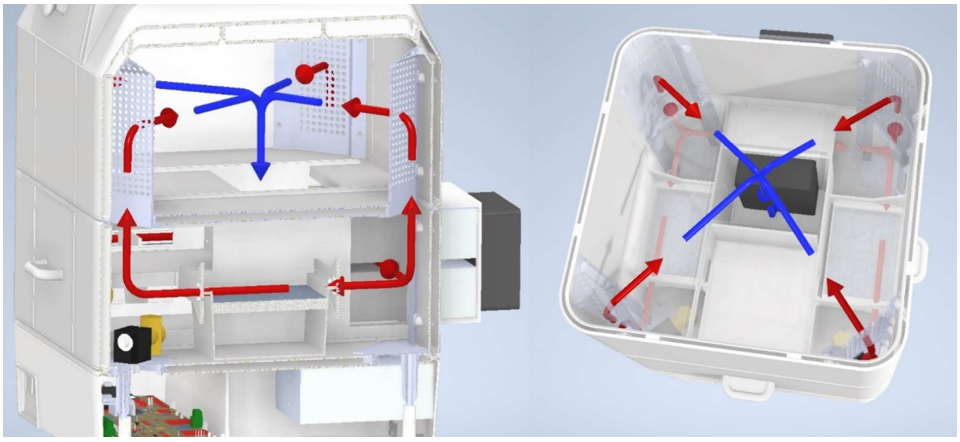

(a) Right side cutaway. **(b)** Top Top down cutaway.

Figure 3.10: The air flow in the environment chamber is driven by a 110 CFM fan directed across the heatsink. Heated air is forced through air columns in each corner of the chamber, over the sample, and down through a return vent below the microscope stage.

The incubator drawer sits between the two air channels in the front center of the air exchanger. It is isolated from the intake by the back panel of the incubator drawer except for a small gap around the edges. There are also slots in the left and right side of the drawer guide. These slots and the gaps in the rear allow the air in the incubator to be mixed without significant air flow directly over the samples. This design is intended to minimize convective heat transfer from air flow over the samples, which would cause faster evaporation

3.2.4 Electronics Housing

The electronics housing's primary purpose is to protect the electronics of the system. They are isolated from the controlled environment by a double-layered barrier between itself and the environmental chamber above. While the power supply board is greater than 90% efficient under load, these loads can be quite large, consuming upwards of 200 W during a warming cycle, leaving as much as 20 W to be dissipated as waste heat. Due to the well-insulated nature of the enclosure, it is necessary to ensure adequate cooling to protect electronic components. This is accomplished by ensuring air flow travels over the components in the box, beginning with the relatively cool components on the control board, and ending with the switching circuitry on the power board. The designed air flow is illustrated in Figure 3.11.

Air is drawn through the electronics enclosure by a Mean Well SE-450-48 48 V DC switching power supply in the rear of the device. The circular fan inlet of the power draws air from the only available inlet in the back of the box. It then follows a closed path across the electronics, into the power supply through the fan inlet, and out the power supply's air exhaust. The air path through the housing maintains a cross-sectional area greater or equal to that of the fan inlet to ensure adequate air flow is maintained.

A temperature of approximately 18.5°C above ambient was measured at the exhaust port of the electronics housing, which isn't excessive for the components used, even assuming that is the temperature over all components in the enclosure. The Raspberry Pi integrated temperature sensor measures 60°C during normal operation, which is within tolerances for the chip.

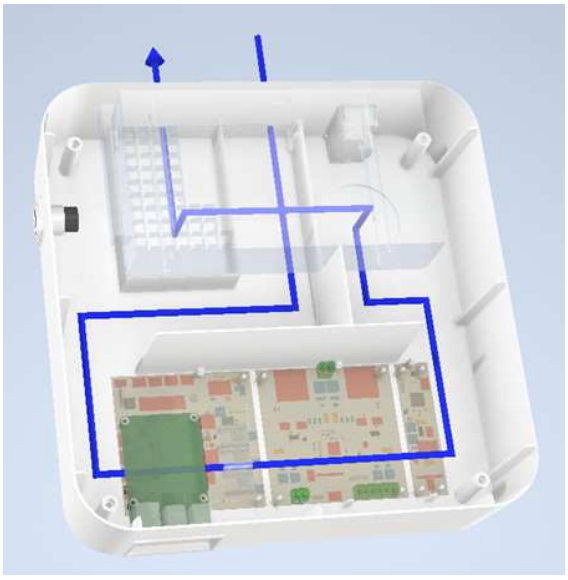

Figure 3.11: Air flow in the electronics enclosure enters the rear of the box. It is guided over the cooler control board, then the warmer power board, then through the 48V power supply and exhausted out the back of the box.

In addition to air flow, the housing must accommodate front panel access to the Raspberry Pi I/O connections as well as a power inlet and HDMI access. Not shown are the interconnecting cables. Originally, power ingress was from the rear of the device, but an oversight in design (two objects cannot occupy the same space) prevents it from being placed there. Instead, the power inlet is on the left side near the HDMI connector.

3.3 Environmental Control

Maintaining homeostasis within the environment chamber requires multiple feedback control systems. Each system consists of at least one sensor to detect the process variable and an effector to control it. All the environmental control mechanisms, shown in Figure 3.12, are housed in the air exchanger unit. A pair of solenoids allow gas mixing internal to the chamber, water baths on the left and right can be used to increase humidity, and a heater in the rear provides heat as well as air circulation for the chamber.

The gas and humidity controllers are relatively simple hysteresis controls, although the gas control is slightly more complex due to the multiple inputs. Temperature is controlled with

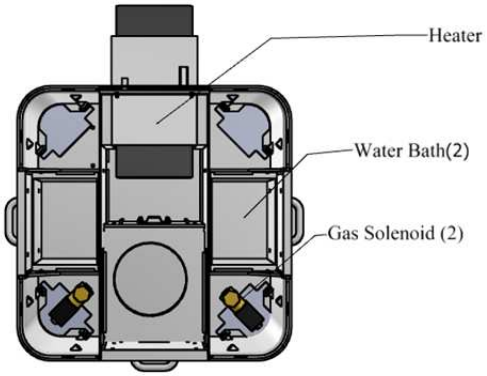

Figure 3.12: Environmental Control mechanisms are housed in the air exchanger, including the gas solenoids, water baths, and the heater.

a Proportional Integral Derivative (PID) control loop due to the need for accurate and precise control. All environmental control occurs within the air exchanger.

3.3.1 Environment Monitoring

There are two types of sensors in the SBX1, one is a LuminOx LOX-02 optical O_2 sensor from SST Sensing, used for the gas control loop. The other is a Bosch Sensortec BME280 Temperature, Pressure and Humidity sensor. These are used for temperature and humidity control. There are two BME280 sensors, one positioned at the objective to monitor temperature and relative humidity near the sample under study. The other is positioned in the incubator drawer. Both sensors were chosen for their excellent datasheet specifications, among other practical factors.

Oxygen Monitoring

The LuminOx LOX-02 sensor is an optical oxygen sensor which relies on fluorescence quenching rather than electrochemical measurements. This methodology provides two primary advantages over electrochemical sensors. First, there is no cross sensitivity with common gasses, including N_2 and CO_2, commonly used in microbiological applications [63]. Second, because the sensor does not rely on a chemical reaction for detection, it can have a longer life in system before requiring recalibration and/or replacement. The drawback is that there is an increased cost at $100 USD per unit compared electrochemical sensors at a cost of $40 USD [64]. How-

ever, electrochemical sensors have a shorter lifetime by 2-3 years, lower temperature tolerance, require frequent calibration, and are subject to cross-sensitivity [64]. These factors make them a poor choice for the SBX1. A more viable selection might be a Zirconium Dioxide based sensor, but the only benefit over the LOX-02 is a longer lifetime at a proportionally higher cost [64].

The LOX-02 measures from 0.1-25% concentration. The accuracy of this measurement is dependent on the internal measurement of ppO2, which has a full scale (0-300mbar) accuracy of better than 2% (6 mbar) [63]. The typical use case of the chamber will be at atmospheric pressure. The pressure measurement is accurate to within 5 mbar, so at standard pressure (1013.25 mbar), this would give a worst-case accuracy of $\frac{6mbar}{(1013.25-5)mbar}$ = 0.6% or ± 0.6% O_2. While the sensor provides a reasonably accurate pressure measurement, the listed accuracy for the BME280 sensor is superior so it is used instead.

Temperature, Pressure, and Humidity Monitoring

Early on in development we were fortunate to find the inexpensive but powerful BME280 sensor, which touts accurate measurements for temperature, pressure, and humidity in a tiny LGA package. It can also communicate over either I^2C or SPI, which makes it easy to control with the microcontrollers in the SBX1. The sensor has an integrated controllable IIR filter and oversampling for temperature and pressure measurements to reduce noise and smooth short fluctuations, particularly in pressure measurements which are subject to sudden changes due to environmental shifts (e.g. doors opening, ventilation starting, etc.) While the datasheet only lists temperature accuracy as ± 0.5°C at 25°C and ± 1.0°C at 65°C [65], the device has been shown to be significantly more precise following individual calibration. Additionally, it is demonstrably superior to the thermocouples commonly used in other environment chambers.

To show the difference in precision, a BME280 and a type T thermocouple were tested against a Fisherbrand Traceable calibrated (ISO 17025, A2LA, NIST) temperature standard, catalogue number 15-078-181. This reference thermometer is accurate to ± 0.05 °C between 35-39°C [66]. To perform the test, the SBX1 was initialized with a fixed 7V input to the heater, which raises the temperature to near 37°C. The reference thermometer was placed on the stage next to the

BME280. The type T thermocouple with was wrapped around the reference thermometer's probe and connected to an MCP9800 thermocouple controller. The result of this experiment is shown in Figure 15, which plots a histogram of the error from the thermocouple, minus the mean offset. The BME280 show a smaller standard deviation of $\sigma_{bme} = 0.03$ when compared to the σ_{th}[3] = 0.11 for the thermocouple.

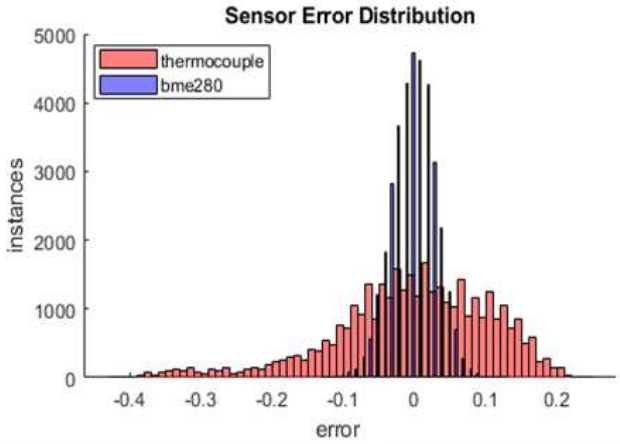

Figure 3.13: Error distribution of a thermocouple versus a Bosch Sensortec BME280.

It is evident that the BME280 is significantly more precise than the thermocouple. With calibration to remove the offset, the BME280 sensor is ± 0.09°C with 99.7% certainty. Accuracy of the humidity measurement is less important; we merely wish to maintain relative humidity within the chamber above 80%. The sensor's stated accuracy of ± 3% is acceptable for this purpose. The pressure sensor has a reported absolute accuracy of ± 1 mbar, which is remarkably accurate. This value is not used for any control systems, but it is only reported to the user interface should the data be desired.

3.3.2 Humidity Control

The environment's relative humidity can be increased either passively or actively. If active control is disabled, humidification is achieved by placing paper wicks in the water baths, rather

[3]The thermocouple deviates from normality somewhat, but it is mostly normal. Regardless, the data clearly show less deviation in the BME280 measurements.

than ultrasonic misters. The level of relative humidity can be controlled to an extent by changing the number of filters added to the wells. A single filter in each well will raise relative humidity to approximately 50%, while three filters in each well will raise relative humidity as high as 100%.

If active control is enabled, humidity is increased by means of an ultrasonic mister in a water bath contained in the air exchanger unit. The mister produces a burst of mist rather than water vapor. This mist must evaporate to raise the humidity within the chamber; and this evaporation is endothermic, pulling heat from the air. This in turn impacts the temperature controller's ability to maintain the target temperature. Thus, enabling the humidifier involves not only raising the humidity in the chamber, but replacing the heat lost to evaporation. In addition, the mist tends to fall, which allows it to condense on surfaces around the mister.

The control loop must compensate for the temperature drop, the lag in humidification, and the potential for condensation after a mist burst. The control algorithm, a "burst and settle" modified hysteresis loop shown in Figure 3.14, addresses these issues. If the system is more than 5% below the target relative humidity, the system enters in the "active" state. In this state, the controller will command 15 second bursts of mist, waiting for humidity to stop increasing before the next burst. This delay is to give the burst time to evaporate. If humidity has increased beyond the set point, then the humidifier will stop, not restarting again until humidity has fallen below 85%. The goal of the loop is to ensure relative humidity does not fall below 80% once in steady state, and that it does not rise above 95%, to prevent condensation. In practice, tests showed that humidity with active control is accurate to ± 5%. Although the humidifier stops misting when the setpoint is reached, mist in the chamber continues to evaporate, increasing humidity. A setpoint of 90% causes humidity to fluctuate between 85% and 95%.

3.3.3 Gas Control

The gas control system is a hysteresis loop illustrated in the flowchart shown in Figure 3.15 which automates the control of two solenoid valves connected to external gas supplies. A fill

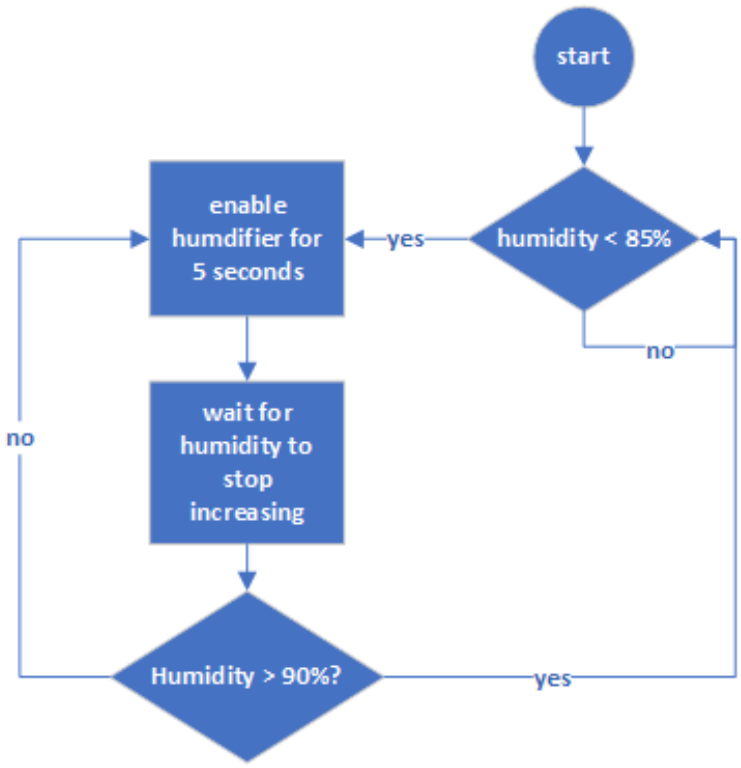

Figure 3.14: Flowchart illustrating humidity control loop.

gas containing no oxygen is connected to the fill port and dry air or oxygen (or some mix containing ample oxygen) are connected to the oxygen port. If the target concentration is above the upper threshold, the controller enters LOWER mode, and opens the solenoid for fill gas. When the O_2 concentration specified by the user interface is reached, the system enters REST mode until either the configuration has changed, or the gas concentration has risen above the upper threshold. These thresholds are adjustable, but default to ± 0.5% of the set point. If the configuration has changed and the new lower threshold is below the lower threshold, the system will enter RAISE mode to bring concentration back into the hysteresis window. When the lower threshold is reached, the system reverts to REST mode and resume the normal control loop. This pattern results in a steady state oscillation with some undershoot as the displacement gas continues to dissipate after the valve shuts, and some overshoot as the system continues to rise above the upper threshold before the fill gas begins to displace air in the chamber.

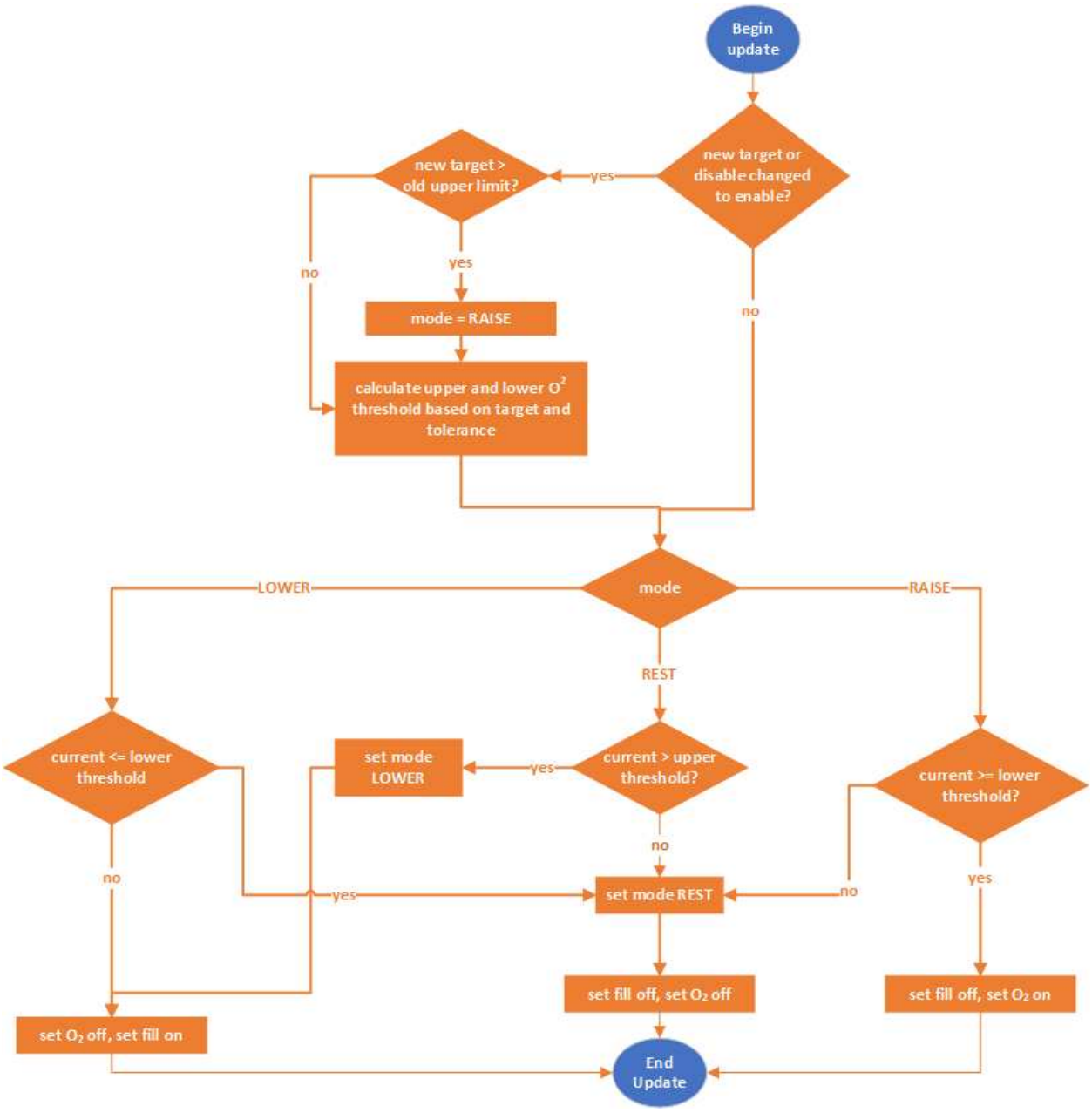

Figure 3.15: Flowchart illustrating gas concentration control loop.

3.3.4 Temperature Control

The temperature control system is by far the most complex of the three to design and implement. It required a reasonably accurate model of the system and a significant investment of time in design and testing. Much of the physical design of the chamber revolved around the requirements for precise and stable temperature control. Temperature within the chamber is

raised by means of a heat exchanger in the rear of the air exchanger layer. The heater is a device which relies on the Peltier Effect, a phenomenon where current passing through joined conductors of different material generates or absorbs heat based on current direction [66]. These devices are known by several names, including “Peltier heater”, “Peltier device”, “Thermoelectric Cooler (TEC)”, and these terms as well as “heater” and “heat pump” are used interchangeably throughout this thesis. While significantly less efficient than a resistive heater, the benefit of such devices is the precision with which they can be controlled. TECs also have a long life, particularly at low temperatures. Single stage elements can have a mean time between failure (MTBF) of over 200,000 hours when not subjected to frequent thermal cycling [67].

Modeling

Unlike the other two systems, temperature control must be maintained precisely and must be resilient to disturbances. For these reasons, a PID loop was chosen for the control mechanism. The loop output controls the power supply board’s channel 0 voltage. This output is connected to a parallel pair of TEC1-12710 40 mm Peltier elements. These heaters are affixed between two heat sinks with thermal grease. Each heat sink has a high throughput (Maximum 110 CFM) 12V 1A fan directing air over the fins. The external fan maintains the cold side at approximately room temperature, while the hot side fan distributes pumped heat throughout the enclosure, as described during the discussion of enclosure design.

The control loop is illustrated in Figure 3.16. The controller ($PID(s)$) corrects its output ($v(t)$) to compensate for the error between the target temperature and the temperature within the chamber. The plant, G(s), includes the conversion of voltage ($v(t)$) to power ($qh(t)$) by the TEC. The heat pumped by the TEC raises the temperature in the system based on the thermal characteristics of the box and its contents, $H(s)$. The heat output of the TEC is slightly nonlinear, but it is linear enough that the integrating term in the controller will be able to compensate for the nonlinearity in the heater. The response of the chamber itself is expected to be purely linear.

The first step in designing the PID control is developing a system model. Characterization begins with the resistance of the walls and the heat loss in steady state. This determines a min-

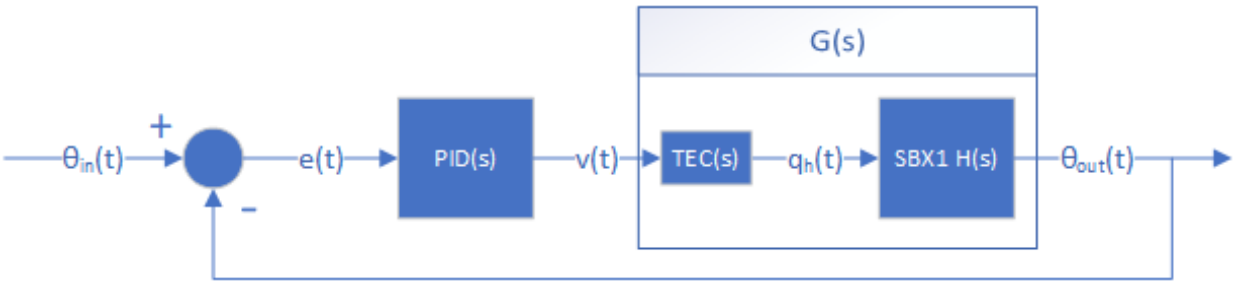

Figure 3.16: The temperature control loop uses negative feedback to regulate the output temperature. The plant consists of the chamber itself, and the heater. The PID loop controls the voltage over the heater to regulate its output.

imum heat input and assists in choosing a heat source. A model for steady state heat loss is shown in Figure 3.17. The higher internal temperature θ_e dissipates through the walls (R1) and the insulating air layer (R2) into the external environment.

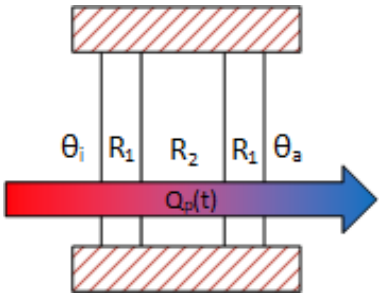

Figure 3.17: Thermal model for steady state heat loss through chamber walls, with the box's internal temperature on the left and external temperature on the right. The rate of heat transfer is inversely proportional to the thermal resistance of the chamber walls.

In the design of the enclosure, limiting the conduction of heat from the internal to the external environment will improve efficiency and increase the maximum stable temperature setpoint. This is characterized by the Fourier's Law,$\dot{Q} = -kA\frac{dT}{dx}$. In steady state, the temperature gradient through a single medium becomes constant. and can be expressed as $\frac{T_1-T_2}{x_1-x_2}$. To simplify the expression, we can substitute $\Delta T = T_1 - T_2$ and $L = x_1 - x_2$ and rearrange the equation to yield $\dot{Q} = \Delta T\frac{kA}{L}$. Finally, we can replace the constant term with a single variable representing thermal resistance: $R = \frac{L}{kA}$, yielding $\dot{Q} = \Delta TR$. This expression is analogous to Ohm's law, applied to thermal conductivity, and this leads to a useful analysis tool: heat transfer problems

can be solved in the same way as an electrical circuit [68]. The equivalent electrical circuit for steady state heat loss is shown in Figure 3.18.

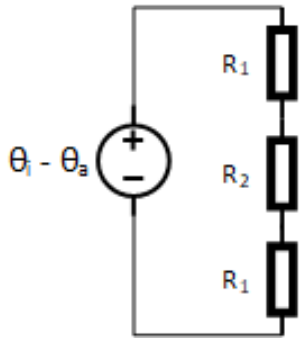

Figure 3.18: The electrical equivalent circuit for steady state heat loss through chamber walls. By convention, ground is 0 °C, so the supply is the internal temperature, θ_i minus the ambient temperature θ_a.

The equivalent electrical circuit can be useful for analyzing behavior of the system, both in illustrating the interaction of components and in allowing application of circuit solving tools. To model heat loss through the walls, we need to know the resistance of the walls, as well as the insulating air gap. These values are calculated with the formula for thermal resistance through a wall: $R = \frac{L}{A \times \sigma}$. where L is the thickness of the wall, A is the cross-sectional area of the wall, and σ is the thermal conductivity of the material. The device prototype was 3D printed using Polyacrylonitrile-butadiene-styrene (ABS). Other plastics are under consideration for the final product, including polycarbonate (PC), and polymethylmethacrylate (PMMA/Acrylic). The highest thermal conductivity of these plastics is PC at $\sigma_1 = 0.22\,\frac{\mathrm{WK}}{\mathrm{m}}$ at room temperature [62]. By contrast, air is substantially less conductive at $\sigma_2 = 0.026\,\frac{\mathrm{WK}}{\mathrm{m}}$ at 30 °C [69]. The internal surface area of the walls of the environment chamber is approximately $A = 0.700.70\,\mathrm{m}^2$. At 3.175 mm thick, this gives the inner and outer walls a thermal resistance of $R_1 = \frac{0.003\,175\,\mathrm{m}}{0.70\,\mathrm{m}^2 \times 0.22\,\frac{\mathrm{WK}}{\mathrm{m}}} = 0.02\,\frac{\mathrm{K}}{\mathrm{W}}$. On the other hand, the air gap is 6.35 mm thick, resulting in a thermal resistance of $R_2 = \frac{0.006\,35\,\mathrm{m}}{0.70\,\mathrm{m}^2 \times 0.026\,\frac{\mathrm{WK}}{\mathrm{m}}} = 0.37\,\frac{\mathrm{K}}{\mathrm{W}}$, an order of magnitude larger than the resistance of the walls alone. Since the thermal resistances are in series in the equivalent thermal circuit (Figure 15), they can be summed to yield an effective wall resistance of $R_w = 2R_1 + R_2 = 0.370\,2\,\frac{\mathrm{K}}{\mathrm{W}}$.

The desired maximum temperature is at least 45°C and we consider room temperature to be 20°C. With the previously calculated resistance and $\Delta T = 45°C - 20°C = 25\,°C$, the heat loss through the walls in steady state can be approximated as $Q_{wall_{45}} = \frac{25\,°C}{0.3702\,\frac{K}{W}} = 67.53\,W$. This gives a minimum estimated power required to reach and sustain 45°C. In addition to the maximum power requirement for the heater, we can also determine the nominal power requirement using the most common set of 37°C, which yields $Q_{wall_{37}} = \frac{17°C}{0.3702\,\frac{K}{W}} = 45.92\,W$.

To compensate for potentially lower ambient temperatures and inaccuracies in the model, an approximately 50% margin is used to select a heater capable of 100W output or greater. This will also give the temperature controller ample headroom for operation. While this value is useful for selecting a component, it certainly does not fully represent the dynamics of the system. To characterize the plant as a whole, we need a better model of the SBX1. In this model, shown in Figure 3.19, heat is transferred through the heat sink h into the internal air i. Additionally, there are objects within the box, particularly the humidifier reservoir and the microscope gantry, represented by block g. These objects will absorb heat from the air until they reach equilibrium. Finally, we have the walls, w, which insulate the heated environment from ambient air.

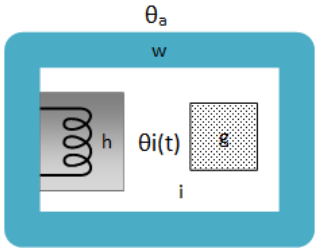

Figure 3.19: The thermal model of the SBX1. The internal temperature $\theta_i(t)$ is determined by the rate of heat dissipated by the heat sink h into the chamber, the heat absorbed by the internal air i and other objects in the box g, and heat lost through the walls w to the ambient air, which is at temperature θ_a.

An analogue to Ohm's law has been established but one more concept is required to model the box as a thermal circuit. The ability of an object to store heat is thermal mass or thermal capacitance [70]. This is a measure of how much heat an object can store and is described by the equation $Q = C\frac{dT}{dt}$, where Q is the heat stored, C is the thermal capacitance in $\frac{J}{K}$, and $\frac{dT}{dt}$ in

$\frac{K}{s}$is the rate of temperature change over time [70]. With this and the calculation of resistance for the walls, the thermal model can be translated to an electrical equivalent, shown in Figure 3.20.

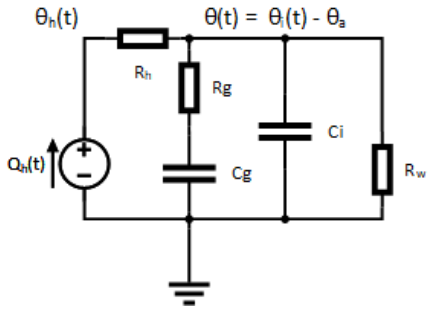

Figure 3.20: The electrical equivalent thermal model for the SBX1. Ground is 0 °C by convention.

In this circuit variables are defined as follows:

θ_a is the constant ambient temperature.

θ_i is the temperature inside the enclosure.

C_g approximates a lump thermal capacitance of the enclosure contents.

R_g approximates a lump thermal conductivity of the enclosure contents.

R_w is the thermal resistance of the chamber walls.

q_h is the heat delivered to the chamber by the Peltier device.

Ambient temperature is assumed to be constant, thus we can treat it as "ground" and use the temperature delta between internal and ambient as the output function. R_h is the resistance of the heat sink, C_i is the thermal mass of the air in the box. R_g and C_g correspond to the thermal resistance and capacitance of the microscope gantry and other objects within the box. Finally, R_w is the thermal resistance of the walls.

The volume of the box is approximately $0.035\,m^3$. Dry air at atmospheric temperature and pressure has an average molar mass of $28.964\,\frac{g}{mol}$, and a density of$1.29\,\frac{kg}{m^3}$. Finally, the specific heat of dry air at constant pressure is $1.006\,\frac{JK}{g}$. This allows the calculation of thermal capacitance of the internal air shown in (3.1):

$$C_i \approx .0350.035\,\mathrm{m}^3 \times 1\,290\,\frac{\mathrm{g}}{\mathrm{m}^3} \times 1.006\,\frac{\mathrm{JK}}{\mathrm{g}} = 45.42\,\frac{\mathrm{J}}{\mathrm{K}} \tag{3.1}$$

For C_g, we approximate the thermal capacity based on the normal contents of the chamber. This consists of approximately 2 kg of aluminum from the gantry, 0.5 kg of iron from the motors, and 0.25 L (250 g) of water in the reservoirs. Using specific heats from [71] we can calculate the thermal mass of the objects within the box as in (3.2).

$$C_g \approx 0.9\,\frac{\mathrm{JK}}{\mathrm{g}} \times 2\,\mathrm{kg} + 0.44\,\frac{\mathrm{JK}}{\mathrm{g}} \times 500\,\mathrm{g} + 4.18\,\frac{\mathrm{JK}}{\mathrm{g}} \times 250\,\mathrm{g} = 3\,065\,\frac{\mathrm{J}}{\mathrm{K}} \tag{3.2}$$

From this, we can clearly see that Cg is much larger than Ci. For this reason, the Ci term can be ignored, reducing the circuit to that shown in Figure 3.21.

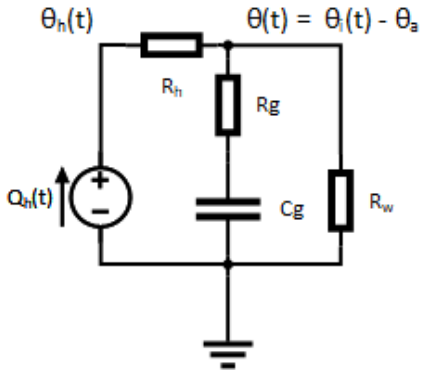

Figure 3.21: The electrical equivalent thermal model for the SBX1 can be reduced to a first order model as the second order components are negligible.

The response of the system is characterized by the equivalent impedance of the system $Z_{eq}(s) = \frac{\theta(s)}{Q_h(s)}$. This is elaborated in 3.3.

$$
\begin{aligned}
Z_{eq} &= R_h + \left(Rg + \frac{1}{sC_g}\right) \Big\| R_w \\
&= \frac{sC_g R_g \left(R_w R_h + 1\right) + sC_g R_w + R_w R_h + 1}{sC_g R_g R_w + R_w} \\
&= \frac{sC_g \left(R_g R_w R_h + R_g + R_w\right) + R_w R_h + 1}{sC_g R_g R_w + R_w}
\end{aligned}
\tag{3.3}
$$

Admittedly this is a bit of a mess, but it can be simplified by substituting an equivalent impedance for the contents of the chamber: $Z_g = R_g + \frac{1}{sC_g}$. Using this substitution, we can write the simplified first order model as shown in (3.4).

$$
\begin{aligned}
Z_{eq} &= R_h + Zg \| Rw \\
&= R_h + \frac{Z_g + R_w}{Z_g R_w}
\end{aligned}
\tag{3.4}
$$

Controller Design and Simulation

From the mathematical model we can see that the simplified circuit is a first order system with one pole and one zero. This information, in conjunction with experimental data from the prototype, was used to determine a first order estimate for the dynamic response of the system. This estimate was used as a starting point for modeling the system and choosing initial values for the K_p, K_i, and K_d coefficients of the PID controller.

The step response of the system will characterize the plant. As mentioned, the heater's output is not linear, but it is reasonably so, particularly for small changes in voltage. After a series of trials, it was found that an input voltage of approximately 7V would place the steady state temperature near 35 °C, near the primary control set point. This was used for determining the step response of the system. To generate a time domain step response, the heater was stimulated with a 7V step input and the output was recorded over a period of approximately 20 hours. The step response of the system is far from smooth, as can be seen in the "true" plot in Figure 3.22.

The instability in output is largely due to shifts in ambient temperature caused by building HVAC, which illustrates the need for a feedback control system. The instability also made an

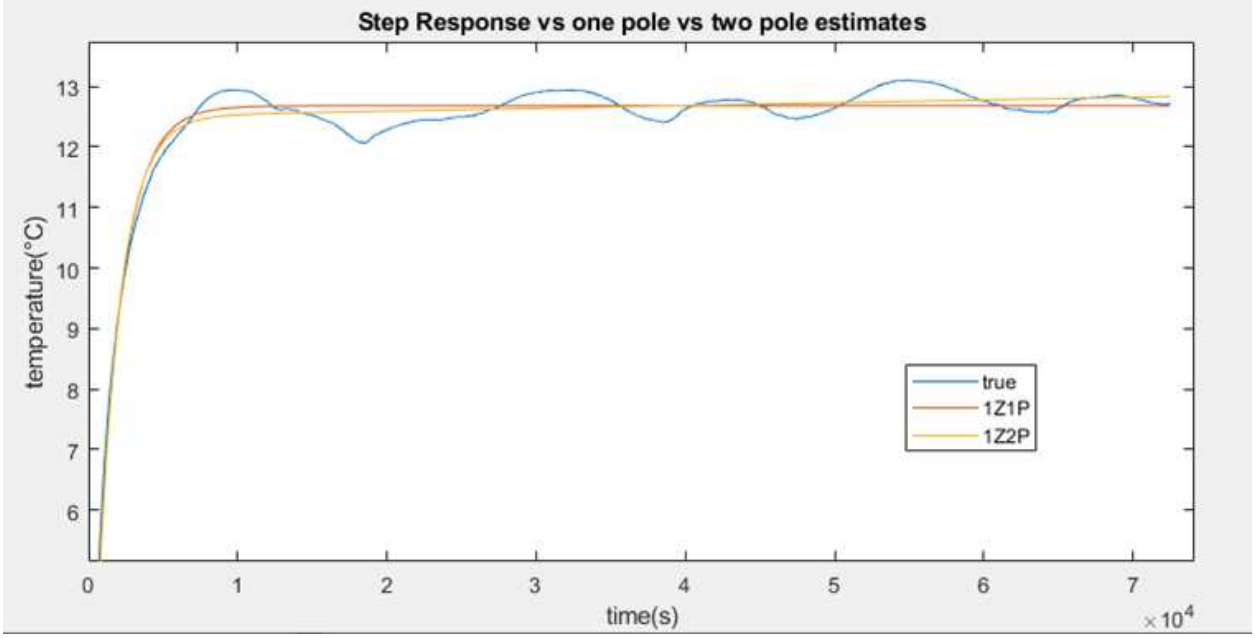

Figure 3.22: Temperature response to a 7V step input compared to step response of single pole and double pole transfer function estimates determined by Matlab's tfest() function. Note that the Y axis is temperature *above ambient*.

accurate estimate of the transfer function difficult. The initial temperature of the box was subtracted from the output, representing the ambient temperature offset. Had the actual ambient temperature been recorded, the output may have been more uniform, but manual tuning of the PID parameters proved subsequent trials to be unnecessary.

Matlab's tfest function was used to estimate the transfer function, both with single and double poles. The single pole fit had only an 82.48% fit to the true temperature, mostly due to the room temperature fluctuations. The second order fit was only slightly closer at 83.62%. Moreover, observing the trend in the plot shows that the first order model better fits the expected behavior of the system, reaching a constant steady state temperature while the second order system continues to grow. As the first order estimate seemed reasonably accurate and mathematical modeling showed a first order estimate was reasonable, this transfer function, $\frac{0.08013s+0.001117}{s+0.0006167}$, was imported into a Simulink model for initial PID tuning, illustrated in Figure 3.23.

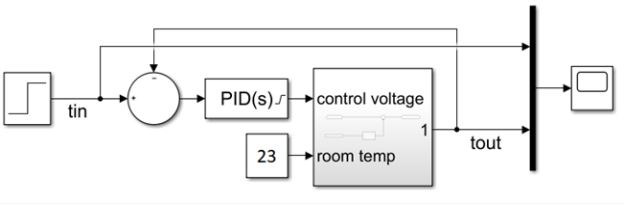

Figure 3.23: Simulink model used to derive initial controller parameters.

With the model established, the Simulink PID Tuner tool was used to generate several potential initial values for the PID coefficients. The PID tuner tool provides two adjustable sliders, one for response time (slower vs. faster), and one for transient behavior (aggressive vs robust). An aggressive response has better disturbance rejection, while a more robust controller will be more resilient against mischaracterization of the plant [72]. Increasing robustness also had the effect of reducing overshoot, which is important because while lower temperatures may be tolerated by a sample, higher temperatures are generally not.

In addition, controllers with the derivative term disabled (set to 0) were considered in Table 3.1: Potential PID coefficients For each set of coefficients, the response time impact is listed with 0 being slow and 4 being fast. Likewise, transient behavior is represented with 0 being the most “aggressive” and 4 being the most “robust”.

Table 3.1: PID Tuning starting points selected from Simulink PID tuning.

#	K_p	K_i	K_d	Response Time	Transient Behavior
1	5.8472	0.073229	0	4	4
2	3.1184	0.0057	0	3	4
3	1.1078	0.00086	0	2	4
4	7.784	0.031627	-357.0727	2	4
5	8.0294	0.0357	-540.7151	4	0

Controller Implementation

The temperature controller is implemented in firmware on the sensor microcontroller. The basic control loop is described by the flowchart in Figure 3.24. The controller enable flag is tested and system flags are configured appropriately. Next the PID values are updated as a function of time in milliseconds. Finally, the power supply is configured based on system state.

Figure 3.24: The high level PID control loop first tests the enable flag for changes. It then updates PID values to determine a new vout for the power supply. Finally, the power supply is updated and tested for faults.

When checking the enable flag, the loop tests against the previous state of the flag to determine if it has altered since the previous iteration of the loop, as seen in Figure 3.25. If the flag has recently been cleared, the controller mode is set to DISABLED and the vout0 supply is disabled. If the flag has been recently set, the mode is set to OFF, and the integrator value is reset to 0 to prevent integrator windup. If the flag is unchanged since the previous iteration, the function returns with no effect.

Even if the mode is disabled, the system will continue testing the enable flag until it has been enabled. If the enable button is checked and the controller has been initialized, the PID loop will update. The update is ignored if less than one second has passed since the last update to prevent flooding the system with unnecessary calculations and messages. The response time of the controller is too slow to justify more frequent updates. If sufficient time has elapsed, new PID values for a given time index t are calculated in 3.5:

$$\begin{aligned} p[t] &= k_p e[t] \\ d[t] &= k_d \frac{e[t] - e[t-1]}{\Delta t} \\ i[t] &= clamp(i[t-1] + k_i \times \Delta \mathrm{t} \times e[t],\ 0,\ \frac{12}{k_i}) \\ output &= clamp(p[t] + i[t] + d[t],\ 0,\ 12) \end{aligned} \tag{3.5}$$

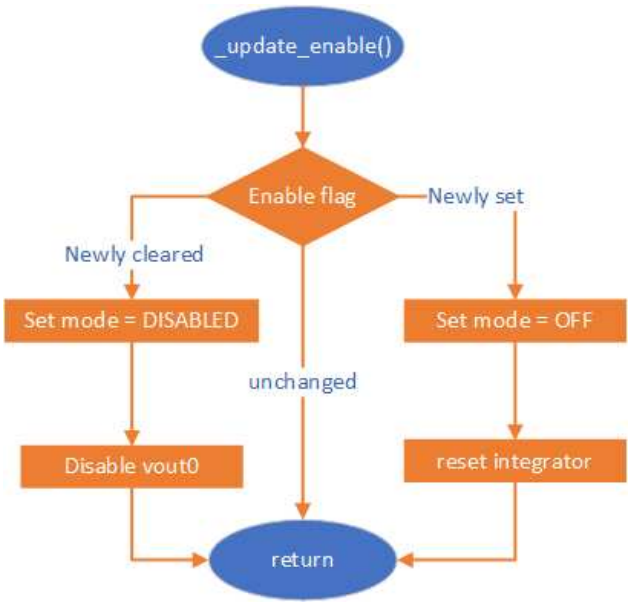

Figure 3.25: The high level PID control loop first tests the enable flag for changes. It then updates PID values to determine a new vout for the power supply. Finally, the power supply is updated and tested for faults.

Where the "clamp" function (1), restricts the returned value to be in the range [min, max]. The integrator is clamped to prevent integrator windup, and the final output is clamped based on the viable range for vout0 as shown in (3.6).

$$\text{clamp}(val,\ min,\ max) = \begin{cases} min & val \leq min \\ max & val \geq max \\ val & \text{otherwise} \end{cases} \tag{3.6}$$

Once the PID loop has been updated, the output value will be set. The main loop then verifies that the determined output level is above the deadzone for the heater. The purpose of this deadzone is to keep vout0 in the programmed range of 2-13.5V for the LTC3886. Additionally, the output is tested for an undervoltage fault. This will occur in the case that the specified voltage causes the current limiter to trigger. This is normal; when the temperature across the TEC, ΔT, is small, more current will be drawn than when in steady state. During initial startup, this current exceeds the programmed limits for the power board output. The firmware responds

by reducing the output voltage during warmup, until the PID determined output can be established without triggering a fault.

Manual Tuning

With the controller designed and implemented, it must still be manually tuned. Tuning a is a slow process due to the long response time of the system. There are tradeoffs in tuning the system. Overdamping may lead to a longer response time on a system which already has a long startup time. An underdamped system will have overshoot. Some overshoot may be acceptable in exchange for a faster response time; however, too much will be detrimental to samples. In the ideal case, the box will be critically damped and rise to the set point with no overshoot. Practically, the repeated trial and error of manually tuning makes it difficult to reach a critically damped state. Instead, the objective was to get as close as possible to critically damped, particularly with the goal of minimizing overshoot, the assumption being that stability is worth waiting an extra hour for the box to warm up.

Methods developed by Ziegler and Nichols are commonly used for manual tuning of PID controllers. Two of these methods are described in [73]; however, each of these methods are intended to be used in isolation, with no prior model. Because a model has already been developed and several viable starting points were determined in Simulink, these methods were not used. Instead, I used the trends shown in Table 3.2 to attempt tuning. The system was allowed to settle to room temperature prior to each trial. In each subsequent trial, the K_p or K_i value was halved or doubled depending on the desired effect on the response. This process was successful after D_d was kept to 0, making the current system a PI rather than PID controller.

The process was repeated using each of the starting configurations obtained from Simulink. Due to the slow response of the system, this process took several days of tuning before an acceptable response was obtained. The final values of the constants were K_p = 2.8263 and K_i = 0.001727. Details of the tuned performance can be found in 4.1.1.

Table 3.2: Relationship of PID constants to tuned response. Adapted from [74].

Response	Rise Time	Overshoot	Settling Time	S-S Error
K_p	Decrease	Increase	No Trend	Decrease
K_i	Decrease	Increase	Increase	Eliminate
K_d	No Trend	Decrease	Decrease	No Trend

3.4 Electrical Design

The electrical system can be divided into four functional subsystems, detailed in Figure 3.26. The user interface system is electrically minor, consisting of a Raspberry Pi 4 Model B and associated peripherals, including a Raspberry Pi Camera V2.0, keyboard, and mouse. The Raspberry Pi coordinates system operation by communicating with the motor control and environment control subsystems. The motor control system is responsible for stage and microscope motor movement and position tracking. The environment control subsystem is responsible for monitoring and controlling the environment within the SBX1. Additionally, it allows communication with external devices via an I^2C port made available in the microscope chamber. The final subsystem is Power Regulation and Distribution, responsible for providing multiple DC voltage outputs for various system components, as well as the variable DC output required for the heater control loop. More detailed descriptions of each section will follow, but first a discussion of various internal communication paths and protocols is necessary. This will facilitate understanding of the overall system.

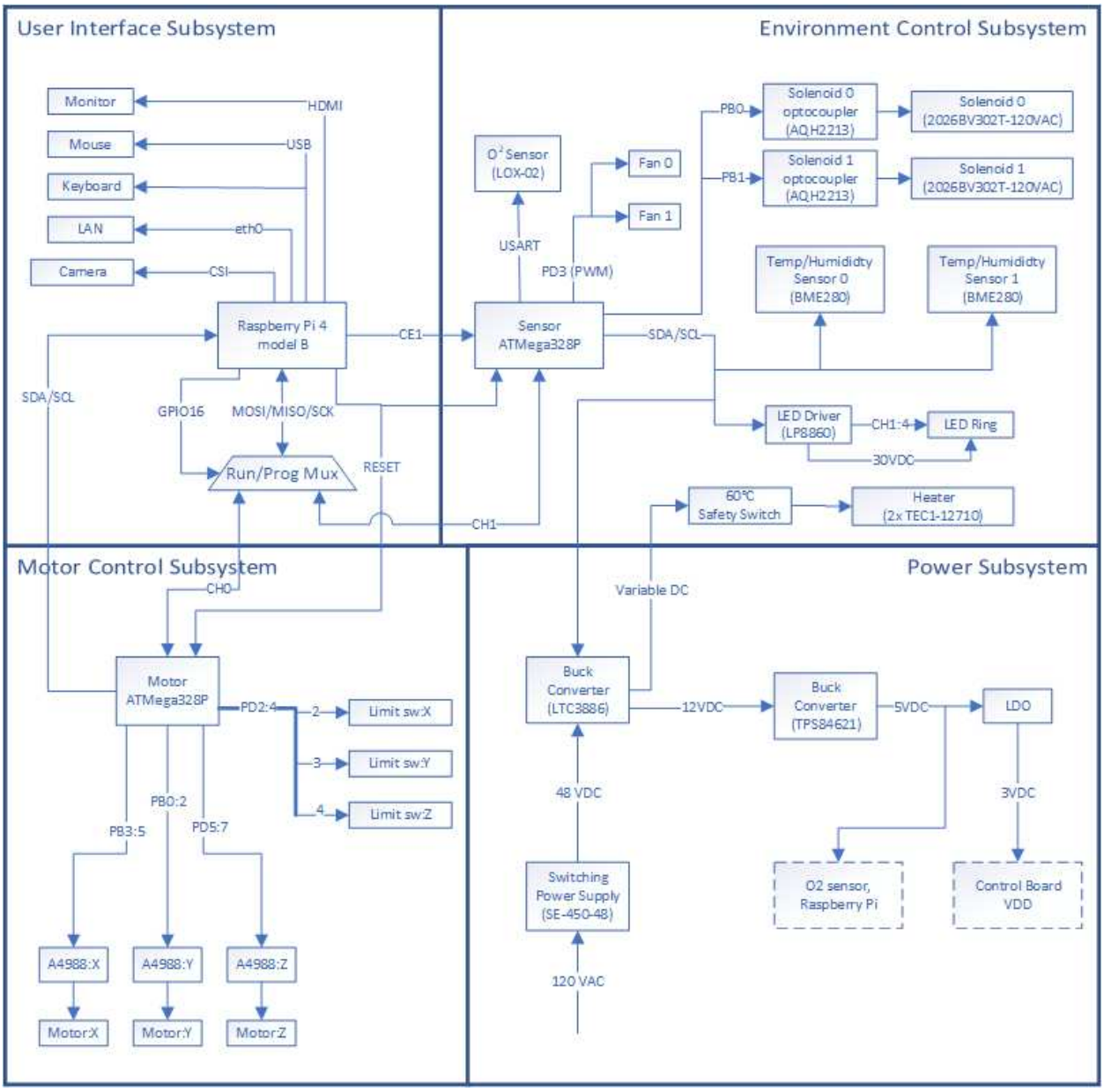

Figure 3.26: The four major electrical subsystems, as well as their major communication and transmission paths.

3.4.1 Inter-Device Hardware Communication Protocols

When discussing communication between hardware, often the terms master and slave are used to denote which device is controlling the communication bus, and which device(s) are controlled by the master. These terms are loaded with social baggage, and instead the terms overlord and minion are used. It's more fun anyway. For overall control of the system, illus-

trated in Figure 3.27, the microcomputer (Raspberry Pi 4) is the overlord, and the microcontrollers (ATMega328P) are minions. Both the motor and sensor microcontrollers require the Serial Peripheral Interface (SPI) pins minus the chip select signal for in system programming. To prevent bus conflicts during programming, the SPI pins excluding the chip select pin are multiplexed from the Raspberry Pi 4 to the two microcontrollers. Since SPI is only ever used for a single controller and is not required for programming, it is wired directly to the sensor microcontroller.

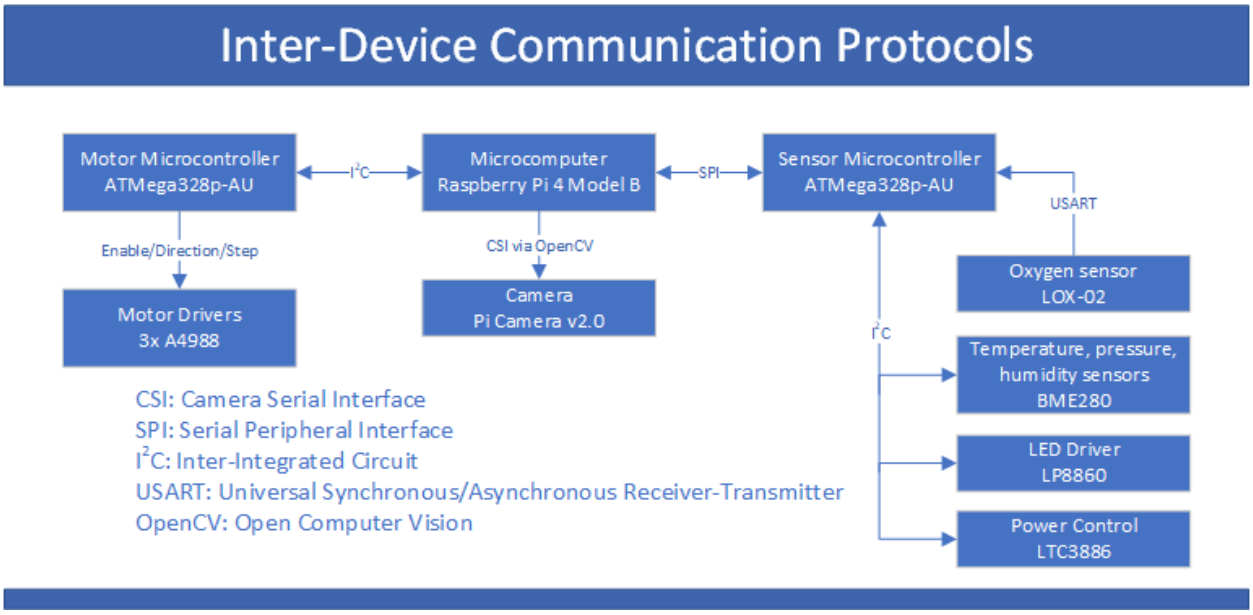

Figure 3.27: Inter-device communication protocols for the SBX1 include CSI, SPI, I^2C, and USART.

When the motor microcontroller is in a "run", rather than "program" state, the hardware SPI pins are utilized for motor control signals, thus precluding SPI from being used to control the motors. On the other hand, the sensor microcontroller must be overlord on its I^2C connection to facilitate communication with the BME280 temperature, pressure, and humidity sensors. For these reasons, communication between the microcomputer and the sensor microcontroller is as a minion on the SPI bus, while communication between the overlord microcomputer and the motor microcontroller minion uses I^2C.

Aside from communication between the microcomputer and microcontrollers, there are a few other protocols in use. The sensor microcontroller monitors its USART connection for formatted strings broadcast by the LOX-02 oxygen sensor. The sensor microcontroller also uses I^2C to control the power system via the LTC3886 buck controller chip, and the ring light via the LP8860 LED Driver. The sensor microcontroller's I^2C bus is also exposed externally for communication with other peripherals such as the BLISS Labs Smart Well Plate. More details regarding communication protocols and the motivation behind their design and use can be found in the software design section.

Finally, the camera is a Pi Camera V2.0, connected to the Raspberry Pi 4 Model B's Camera Serial Interface (CSI) header. With these communication methods established, each component in the system can communicate directly or indirectly with the microcomputer, which can orchestrate environmental control and microscope operation as dictated by the user. The Raspberry Pi 4 also has two USB 2.0 and two USB 3.0 ports and an ethernet port exposed on the front panel of the SBX1. These are used for a keyboard, mouse, and any other peripherals the user wishes to connect such as a thumb drive.

3.4.2 User Interface

User interface software running on the Raspberry Pi is the central access point for any control or monitoring of the SBX1. The user controls the system using a keyboard and mouse connected to the Raspberry Pi's USB ports. Microscope video is received from a Raspberry Pi Camera V2.0, and network connectivity can be established via Wi-Fi or ethernet. This may be helpful if the user wishes to use network storage, or simply needs access to the internet. The bulk of the user interface subsystem lies in software and firmware, discussed later.

3.4.3 Interconnecting Cables and Interface Board

To isolate the environment chamber from the electrical system, an interface board is mounted between the electronics and air exchanger sections. Each side has headers for interconnecting cables. To protect the connections on this board from corrosion, the environment

side of the board is sealed using potting epoxy once the cables have been connected. The individual regions of the interface board are clearly visible in Figure 3.28. The 15 pin FPC cable for the camera is on the left side. To the right of the FPC connectors is the control header. To the right of the control header are the fan fault detection electronics. On the underside are connectors for the high voltage inputs, 24V for the humidifiers, 12V for fans, and the TEC connector. On the top side there are no connectors, instead the wires for power connections (12V/24V/heater supply wires) are soldered directly to the pads prior to potting.

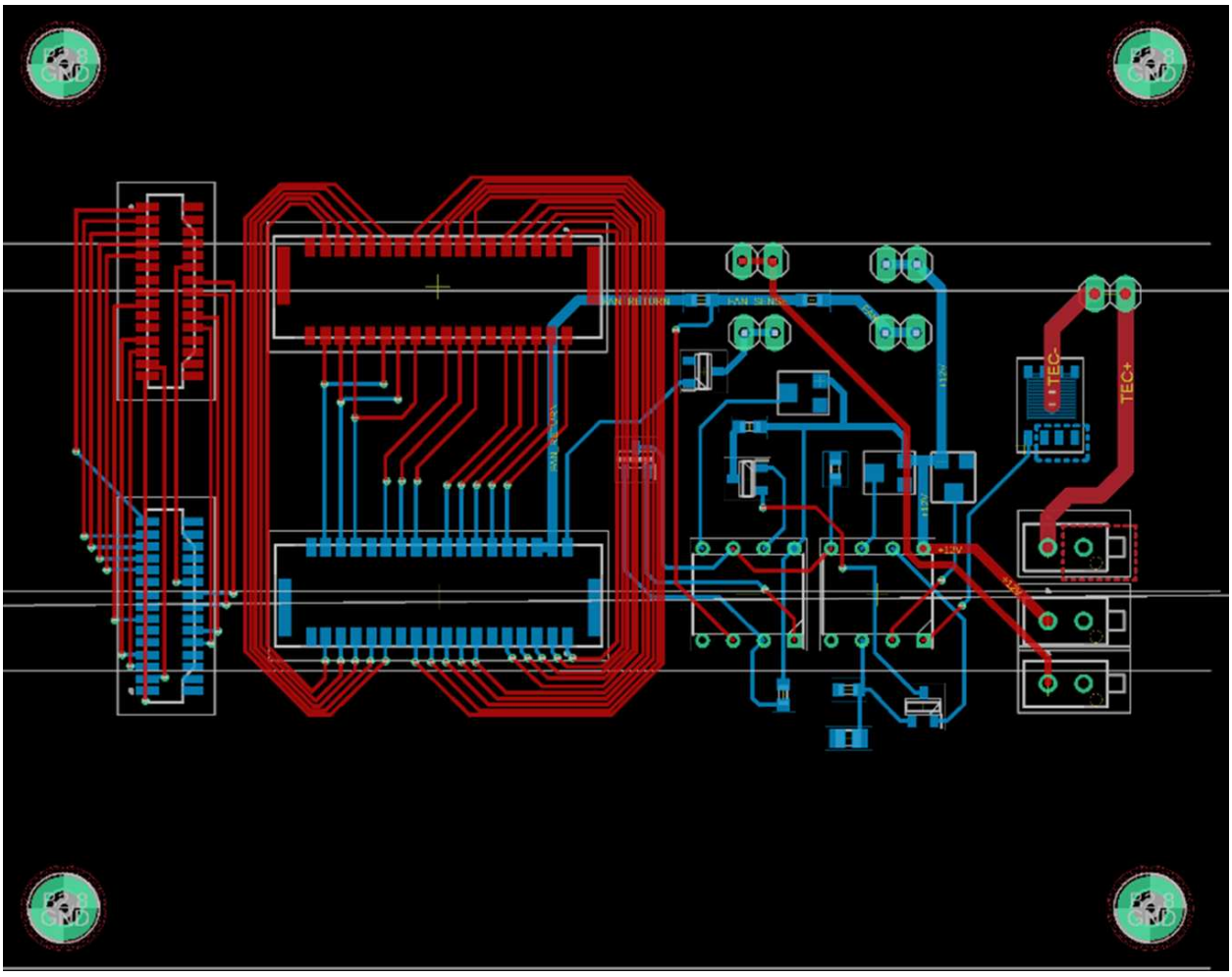

Figure 3.28: The interface board layout shows the camera, data, and power connectors as well as the fan PWM detection circuit.

The pin configuration for the communication header is set up to isolate signals which might interfere with each-other. The motor connectors are on the center pins, with each motor's control pins separated by limit switch pins, one of which is connected to ground and the other pulled up to VDD. ON the outer sides of the connectors are the Serial, I^2C, LED, fan, and humidifier connections, with each circuit separated by a ground wire.

There are two types of electrical connector in the system, with examples shown in Figure 3.29. Molex Micro-Lock Plus for lower current (< 2.0 A) and Molex MicroFit Plus for higher current or high voltage (>12V) applications. Micro-Lock Plus connectors have a variety of desirable characteristics for a broad set of applications. With a pin pitch of 1.25 mm and a current rating per pin of 3.6A [74], they provide a reasonably high current capacity in a small footprint. They are also available with a wide range of circuits per connector, from 2 to 16 circuits in a single row configuration and up to 42 in a dual row configuration.

The versatility of this system makes is suitable for most connectors in the SBX1; however, there are a few circuits with a higher current maximum, or high voltages which would risk arcing due to proximity between pins. For these circuits, the system uses the Molex MicroFit 3.0 connector system, which have a solid latching mechanism and fully obstruct any contacts from wandering fingers. They are rated for up to 12.5A and house from 2-24 circuits. These are used for power supply, heater, and solenoid wiring.

(a) Microfit Plug **(b)** Microfit Socket **(c)** Microlock+ Plug **(d)** Microlock+ Socket

Figure 3.29: To minimize BOM costs, two connector types are used for all connections other than the camera. Molex Microfit connectors handle circuits with greater than 2 A or voltage greater than 12 V, while Molex Microlock+ connectors handle anything lower voltage or current.

Wire diameter is another factor. Thinner wires will have a larger voltage drop as well as reach higher temperatures, but they cost less. There are also restrictions in wire and insulation thickness based on the pins for each connector. 26 AWG MIL-DTL-16878/1 wiring will work with the MicroLock Plus pins. These can be expected to carry up to 3.5A without exceeding 80 °C with 40 °C ambient air [75]. The wire specification ensures that insulation diameter is compatible with the MicroLock Plus pins. For the MicroFit+ connectors, 18 AWG MIL-DTL-16878/1 wire is used, which can pass up to 13.2 A under the same conditions [75].

3.4.4 Environmental Control

Environmental control is managed by the Sensor Microcontroller. Setpoints for environmental control variables (temperature, oxygen, and humidity), are sent to the microcontroller via the user interface over SPI. In its main loop, the microcontroller receives updates from sensors and sends commands to the control devices for each variable.

Temperature

Temperature is sensed by a BME280 sensor placed near the microscope objective. This sensor detects the current temperature inside the chamber. The control loop uses this temperature to determine the setpoint and sends the updated output voltage to the LTC3886 on the power board via I^2C using PMBUS commands. The LTC3886 then adjusts the output voltage to match. The heater is subject to change, but at this time two Heibei TEC1-12710 Peltier devices are used in parallel. These devices are rated for 15.4V and 10A; however, they do not reach this limit. Instead, they are configured in parallel and driven with a maximum of 12V, and current limited by the LTC3886 to 10A total or approximately 5A each.

Fan Circuit and Heater Cutoff

Should the circulation fans fail, the heat sinks will not be able to dissipate heat quickly enough and the heater and heat sinks will overheat. Temperatures will not be high enough to cause fire, even at maximum output for the heaters; however, they will still sufficient to cause

plastics to melt or degrade, and the TEC could be damaged by excessive heat. It is therefore important that the TEC not be engaged unless both internal and external fans are running. For this reason, a detection circuit closes the heater circuit only if the fans are running. The current version of the SBX1 uses two-wire PWM controlled fans. Detecting a fan speed fault is accomplished using a current monitoring. Corrosion on the interface board may increase resistance on the fan line, or a fan may be disconnected, which would cause reduced current through the fans. Alternatively, a fan's bearings may wear out or a fan may stall. In either of these situations, fan current will be increased above nominal levels. The circuit is placed on the interface board and is an analog circuit independent of the temperature control software, this ensures that even in the event of software glitches, the hardware protection circuit will function except in the event of a catastrophic failure. Future versions will incorporate a fan with an integrated tachometer and PWM control, simplifying both fan speed control and monitoring.

Figure 3.30 illustrates the current monitoring circuitry for the fans. Microcontroller PWM is amplified to 12V using an N Channel MOSFET on the low side of the fan. A diode clamp for gate protection and an RC network in series with the fan are not shown to simplify the diagram. The current through the fan is the same as the current through current sense resistor R1. This current is sensed by the monitor circuit consisting of IC2, R1, R2, and R7. The circuit incorporates an implementation of the current monitor circuit found in Texas Instruments AN-31 amplifier circuit collection. The output of the current monitor is the voltage over R7 and is proportional to the current through R1, given by $V_{R7} = I_{R1}\frac{R1R7}{R2}$.

This output is fed into the inverting input of IC1 and the non-inverting input of IC4, which combined create a window comparator with bounds set by potentiometers R4 and R8. The outputs of the comparators are ANDed through Q1 and Q4, with the output taken over R10 and C1. C1 charges quickly through R3 if the output current is in the valid window but discharges slowly if either Q1 or Q4 is off due to the higher resistance discharge path through R10. This converts a PWM input to be converted to a DC output with some ripple and ensures that temporary fluctuations are unlikely to disturb the output. Finally, to prevent the heater from being "partially

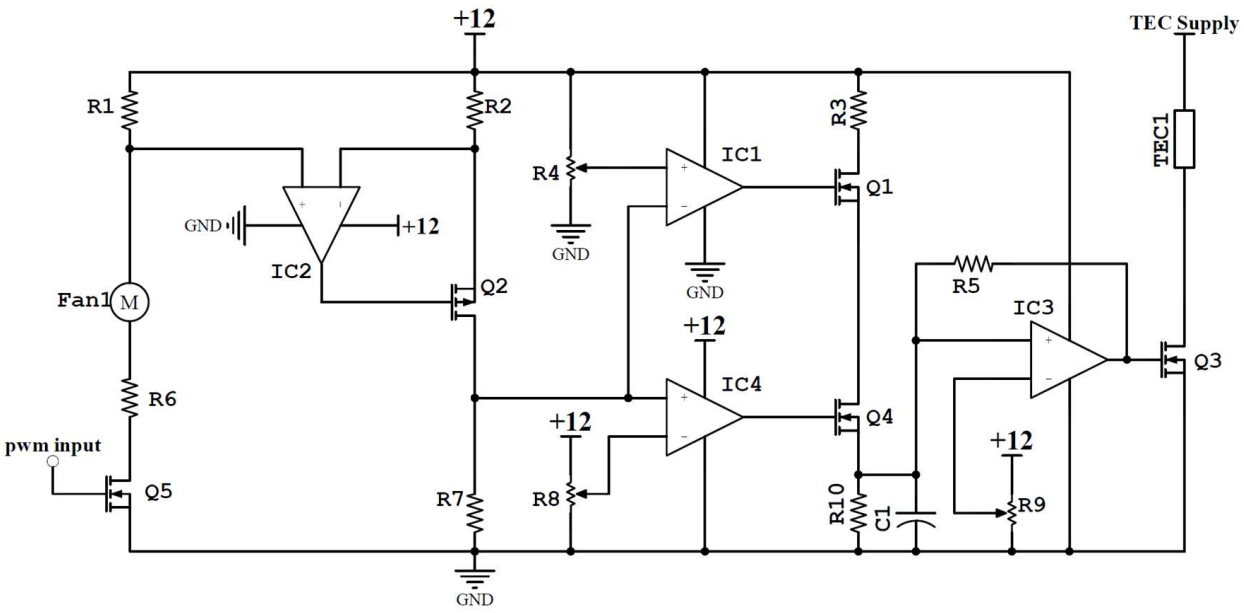

Figure 3.30: The fan circuit includes a PWM detection circuit which monitors the PWM current through the fan motor. A fan fault, either a short or increased resistance, will cause the heater to be disabled, protecting the SBX1 from overheating due to a lack of circulation over the heat sinks.

on", this output is fed into IC3, configured as a comparator with hysteresis provided by positive feedback resistor R5 to prevent ripple from causing the output to oscillate near the threshold. If the output voltage is above the value set by R9, the heater will be enabled, otherwise it will be disabled.

There are three calibrations to perform with the circuit: Lower bound, upper bound, and output cut-off. The lower bound threshold disables the output if current through the fans has dropped below some threshold. For both bounds, the PWM input is set to a DC signal. These amplifiers are calibrated based on the current through the fan.

To calibrate the lower bound:

1. Replace R6 with a 50 ohm (or whatever threshold is desired) resistor.
2. Adjust R8 until IC4 just barely turns off.
3. Replace R6 with a 0 ohm jumper.

To calibrate the upper bound:

1. Adjust R4 until IC1 just barely turns off; note the voltage.

2. Prevent one fan from spinning to produce stall current.
3. Adjust R4 until IC1 just barely turns off; note the voltage.
4. Release the fan and ensure it begins spinning again.
5. Adjust R4 to approximately halfway between the voltages from steps 1 and 3.

The cut-off amplifier requires somewhat more finesse due to overcurrent faults. In the event of an overcurrent condition, current will be within the valid window during the rise and fall of a PWM pulse and thus the amplifiers will output a brief spike. The duration of this spike is determined by the slew rate of the amplified PWM signal and should be minor; however, these spikes will likely still accumulate some DC input to the final amplifier. The cut-off amplifier must be calibrated so that this DC level is insufficient to enable the heater, but valid PWM signals do.

To calibrate the cut-off amplifier:

1. Set the fan PWM duty cycle to 20%.
2. Adjust R9 until IC3's output just barely turns off
3. Set the fan PWM duty cycle to 30% (the normal operating duty cycle)
4. The output of IC3 should go high. If it does not, lower R9 until it does.
5. Stop the fan from spinning on one motor to produce a stall current. The output of IC3 should go low, possibly after some delay as C1 discharges.
6. Release the fan. Spin it manually to start it again if it is still stalled.
7. The output of IC3 should go high again.

Humidity

Humidity can be passively elevated using wicking filters in water baths, or actively with the use of ultrasonic misters. For active control, humidity is sensed via a BME280 sensor in the left rear air column. This position is to ensure an accurate measurement by placing the sensor's vent hole such that it faces the rising air within the column. If active control is used, the misters are enabled or disabled by controlling the gate of an N channel MOSFET to control power to

each mister. The misters themselves are cheap generic fountain misters from Amazon used as a proof of concept.

Gas

Gas control relies on a Luminox LOX-02 oxygen sensor. It is capable of reporting concentrations in ppm or percent. The latter is used for the purpose of environmental control, as it is the more relevant factor for biological experiments. The relative concentration is maintained by controlling a pair of Panasonic AQH2213AZ optoisolators which switch the gas solenoids on or off. The primary consideration for this device is its output capacity. The chips are rated for a peak repetitive off state voltage of 600V and an on-state RMS current of 900 mA [76]. They are more than up to the task of sustaining the 8.3 mA RMS expected from the solenoids, which are labeled as drawing 5.5VA at 120 VAC RMS.

The chip also has integrated zero crossing detection to minimize switching surges. As an additional failsafe the solenoid control circuit, shown in Figure 33, includes a TVS diode (D) to prevent surges caused by switching the solenoid load when relatively large current is flowing through it, which might damage the from damaging the optoisolator or solenoids. To protect the optoisolator's LED from overcurrent damage, a 100 Ohm resistor (R) is placed in series with the input to limit current through the internal LED to 21mA. There are two instances of this circuit, one for each solenoid.

3.4.5 Lighting Subcircuit Design

The driver circuit for the LED ring is based on a Texas Instruments LP8860-Q1 Low-EMI Automotive LED Driver. This chip has four independent 150mA current sinks and can control the current through each channel independently to within 0.5% of the set point [77]. In addition to the current sink outputs, the chip has an integrated boost controller to provide the high voltage required to drive long serial strings of LEDs, with an input range of 3-48V and a conversion ratio of 10. Finally, the chip supports I^2C communication, a requirement as the microcontroller is a minion on its SPI and there are limited pins on the microcontroller for controlling peripherals.

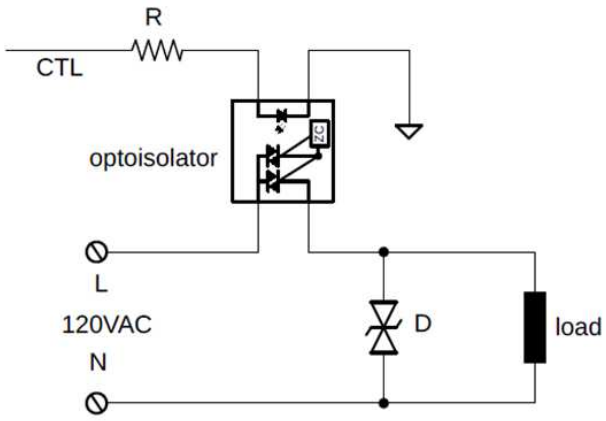

Figure 3.31: The gas control circuit is very simple. An opto-isolator is driven by control from the microcontroller to make the connection from the 120V AC input to the load. A TVS Diode protects the load and the optoisolator from surge currents.

Configuration

Prior to designing the electrical circuit for the driver, the chip's EEPROM must be configured. Multiple variants of pre-programmed chips are available, but none match the requirements for the SBX1. Programming is performed using the firmware and software discussed later in the thesis. Key parameters are shown in Table 3.3. While the driver can sink 150mA per channel, each channel is limited to 60mA. The UV LEDs on the ring light are quite sensitive and have a 60mA current limit, and the other LEDs in the system are sufficiently bright at this level. Restricting all channels to this level protects the UV LEDs in the event of miswiring.

Circuit Design

The electrical schematic for the control circuit can be found in Figure A.1 in Appendix A. Most of the circuit makes up a boost converter to raise 12V to the 30V necessary to drive the ring light. Many of these components are shared with the power board to keep the number of BOM line items small, allowing reduced cost from bulk pricing. The bulk of the circuit is centered around the boost converter for providing the LED string supply voltage. VDD for the system is 3.3V, which is insufficient to drive the switch N channel MOSFET's gate. Fortunately, the LP8860-Q1 has an integrated charge pump for this purpose, although it requires external

Table 3.3: Key Texas Instruments LP8860-Q1 LED Driver EEPROM settings.

Register	Value	Effect
LED_STRING_CONF[2:0]	111	all channels in cluster mode
EN_EXT_LED_CUR_CTRL	0	Use internal current limit scaling
DRV_LED_CURRENT_SCALE[2:0]	011	per channel current limit = 60 mA
EN_CL_LED_FAULT	1	Enable open/short fault detection
BRT_MODE[1:0]	10	brightness is controlled via register
CP_2X_EN	1	Enables charge pump
BOOST_GD_VOLT	1	Use charge pump output for gate driver
BOOST_INITIAL_VOLTAGE	11100	Set boost voltage to 30V
BOOST_IMAX_SEL	111	9A boost current limit
BOOST_EXT_CLK_SEL	0	Use internal clock for switching
BOOST_FREQ_SEL	010	303 KHz switching frequency

output and flying capacitors. The charge pump output then provides approximately 6.6V for the gate driver, more than sufficient for the 3.6V threshold to bias the transistor.

The most important characteristic for component selection is maximum inductor current. First, the inductor is selected to prevent saturation at the maximum inductor current. This can be calculated based on switching parameters and input/output characteristics; however, the datasheet [77] recommends a more conservative and straightforward solution of ensuring inductor saturation is above the switching current limit programmed in EEPROM, which is 9A. It also recommends inductors from 22uH to 33uH, with a DC resistance less than 300 mOhm. A 22uH inductor was chosen to keep component size to a minimum. The datasheet also suggests using the fault switching current as a conservative minimum for the saturation point of the inductor. This is configured at 9A. The Bourns SRP1265A-220M meets these specifications.

The guidance in the datasheet for the rectifier diode suggests that “peak repetitive current” should match peak inductor current; however, this appears to be a typo. It should likely be “peak current” instead. [78] provides clearer guidance for selecting a rectifier diode, advising a Schottky diode with an average current rating higher than the maximum output current of the boost converter, and suggests that the peak current is easily accommodated by the high surge current rating of Schottky diodes. The B1100-13-F used in the power board is rated for 1.0A

average forward current, easily above the 600mA maximum output and can be reused for this converter.

The other important requirement is the output capacitor. For a 600 mA output (all four channels at maximum), the datasheet recommends a 33 uF electrolytic bulk capacitor with < 500 mOhm ESR and a 10 uF ceramic filter capacitor. While none of the channels are expected to draw more than 60 mA, these values are still taken to ensure the driver is capable should the load increase. The input capacitors can be the same components/values; however, because ceramic capacitors are more expensive for higher voltages, a different model was chosen for C14 with only a 16V rating, as opposed to the 50V rating for [77].

The design guidelines in [77] recommend a VDS breakdown of 5V higher than the output voltage, which would be 35V, and a current rating to match the inductor peak current (9A). The NFET chosen for the power board is suitable for this application.

LED Ring Design

The ring light for the microscope is a relatively simple design. The top side layout of the board can be seen in Figure 3.32. It consists of four channels of 8 LEDs each. The choice of LED was limited by the LP8860 LED driver on the control board: each channel can sink a maximum of 150 mA, which limits the specification for the LEDs. Another feature is that the forward voltage of the LEDs should be less than 3.5V. This voltage ensures a buffer of 2V from the 30 Volt maximum of the LED circuit's boost converter. This is to ensure that manufacturing variances in diode forward voltage do not exceed the 30V supply. Additionally, each string has a 2512 resistor which can be selected to tune the drop over a string at maximum current to 29V with a current of 60mA. The objective of these resistors is to minimize power dissipated by the LP8860 for current limiting: by placing the maximum voltage drop over the load (resistor + diodes) near the voltage peak, less power must be dissipated by the current sinks in order to maintain the set current, instead dissipating excess heat over the chip resistor. The remaining 1V is left to accommodate variance in forward voltage over LEDs. Each board has pads for one ring each of UV LEDs, white LEDs, and two additional single-color LEDs. For white LEDs, Luminus Devices

MP-2016-1100-40-90 for their high color rendition index (CRI) of 90% and typical intensity of 23 lumens [79].

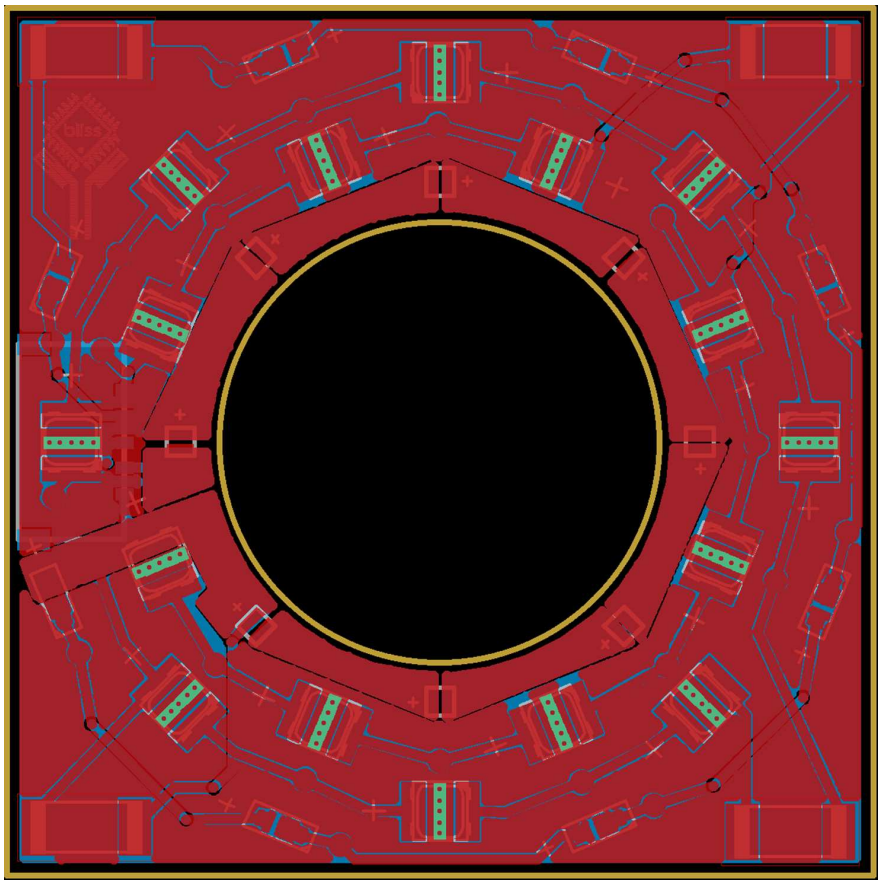

Figure 3.32: Ring light board layout showing 4 channels, current limiting resistors, and heat dissipation pours.

The CRI is important to ensure colors are accurately rendered across the full visible light spectrum. CRI itself is a quantitative value, obtained by measuring the chromaticity of samples illuminated by the source under test with respect to the chromaticity when illuminated by a blackbody source [80]. An example of the effect of CRI on images can be seen in Figure 3.33. Note that low CRI poorly renders the skin tone of the woman in the image, and the colors in the pastel palette do not match the more accurate high CRI image on the left. There are other, arguably better, standards for measuring color fidelity, but the LEDs surveyed during part sourcing report CRI as a metric.

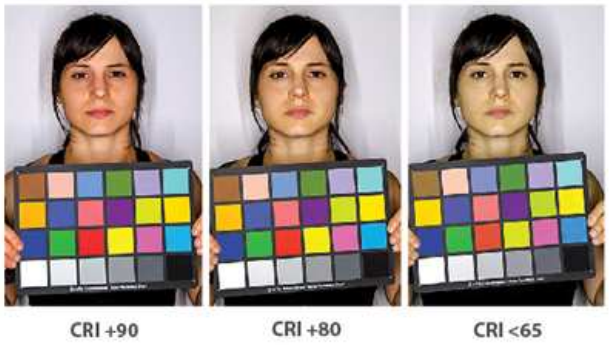

Figure 3.33: Qualitative demonstration of color fidelity for images, illustrated by LEDs with different CRI. Source: [80]

.

These LEDs are placed on the outer ring of the light board. The selection for UV LEDs is limited. UV LEDs are used for exciting DAPI stains, with an emission peak with excitation at 358 nm. There are several options for LEDs around this wavelength, but most have a fairly high current requirement (greater than 500 mA). At the time of developing the ring light, the Vishay VLMU1610-365-135 was the only LED near 365 nm listed on Mouser or DigiKey with a forward current of less than 150 mA. These LEDs are rated for 60mA forward current. At this maximum output, they produce a typical 63 mW of 365 nm light [81]. The remaining two single color LEDs can be any Cree XLamp ML-E series LEDs. This series has a typical forward voltage of 2.4 V to 3.4 V, depending on the color selected [82]. To make isolating damaged LEDs simple, test points are placed between each LED for easy access by a diode tester.

3.4.6 Motor Subcircuit Design

Stepper motors require precise outputs on multiple phases for control of the stepping action. The waveform generation for stepper motors in the SBX1 is handled by COTS stepper motor drivers based on an Allegro Microsystems A4988 microstepping driver IC. Each driver exposes direction, enable, and step pins to the motor microcontroller for commanding movement. The drivers are capable of full steps or $\frac{1}{16}$, $\frac{1}{8}$, $\frac{1}{4}$, and $\frac{1}{2}$ microsteps. Three zero-ohm jumpers allow configuring the microstep settings of each driver according to Table 3.4. The presence of a resistor pulls the pin to 3.3 V. In the current configuration, X and Y drivers are

configured for $\frac{1}{16}$ microsteps while the Z driver is configured for $\frac{1}{4}$ microsteps. Apart from the obvious benefit of more granular and therefore more precise positioning of the gantry, smaller microsteps reduce motor noise and vibration during movement, at the expense of a slower maximum rate of travel. The Z axis is at $\frac{1}{4}$ microsteps rather than $\frac{1}{16}$ to reduce the time it takes to focus.

Table 3.4: Configuration of jumper resistors for A4988 Microstep size.

MS1	**MS2**	**MS3**	**Microstep Resolution**
L	L	L	Full Step
H	L	L	Half Step
L	H	L	Quarter Step
H	H	L	Eighth Step
H	H	H	Sixteenth Step

3.4.7 Power Subcircuit Design

The power electronics in the system reside in an off-the-shelf 24V power supply, the power board, and a power conditioning section in the control board. There is also the boost converter section of the LED controller previously discussed. Power must be distributed throughout the system for the SBX1 to function. It is also important to understand the power consumption of each section both for design purposes as well as for system specification for end users.

Circuit Design

The largest custom portion of the power subsystem is the power board, responsible for providing a stable 12V DC supply to the control board, and variable 12V DC for controlling the environment heater. The circuit diagrams for the power board are shown in Figures A.4 through A.6. They are based heavily off of the channel 0 portion of the Analog Devices DC2155A-A evaluation board for the LTC3886 [83]. Primarily the differences are in part selections for passive compo-

nents, less expensive chip capacitors and resistors were used where possible. In the reference design, parallel N Channel MOSFETs are used for the top and bottom switching transistors. In the power board, these are replaced with single high power SIR186DP-T1-RE3 transistors. The remainder of circuit modifications have more to do with layout than circuit design and are discussed in Chapter 3.5. Each channel has an LED tied to the power good indicators. If illuminated the channel has a fault or is disabled.

The control board houses additional step-down circuitry based on a Texas Instruments TPS84621. This circuit can be seen in Figure A.2. The chip is a monolithic buck converter which includes all of the buck circuitry interally; however, it still requires input and output filtering and bulk capacitors, as well as configuration resistors. The undervoltage lockout is configured to disable the chip if supply voltage drops below 6.6V. Output voltage is configured to output 5.0V with a 780 KHz switching frequency. This rail is primarily used for the Raspberry Pi. With the filtering capacitors, the output voltage is sufficiently stable and clean for powering the microcomputer's digital circuitry. One final low dropout regulator (LDO) drops the 5.0V to 3.3V. An LED over the power good output of the TPS84621 serves as an indicator for the 5V rail, and another at the output of the 3.3V LDO indicates power good for the 3.3V rail.

Distribution and Regulation

Power distribution through the system is shown in Figure 3.34. The box runs on mains power, 110 V AC or 220 V AC, which enters the system through a fused power entry module. This is routed to the control board for use by the gas mixing solenoids as well as to a 24V, 450W linear power supply (Mean Well SE-450-24). This is the primary power source for the DC components of the system. There are five DC voltages in the system: 30V, 24V, 12V, 5V, and 3.3V, all derived from this power supply output.

The 24V signal has two branches. One provides power to ultrasonic humidifiers, and the other is the supply voltage for the power board, which implements dual channel buck converter with adjustable voltage output and current limiting capabilities with a 12V/10A maximum per channel. Channel 0 is connected to the heater; its set voltage is varied with the PID output to

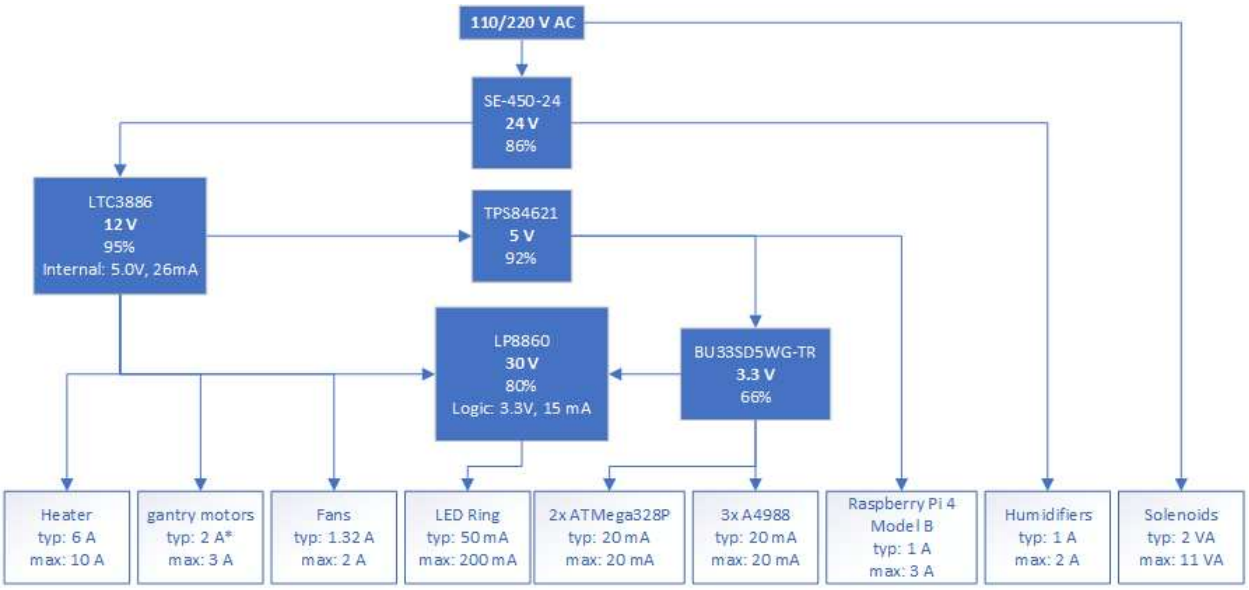

Figure 3.34: Power Distribution in the SBX1. Multiple DC levels are used throughout the system. Primary power consumers are listed with typical operating consumption as well as the design maximum. DC/DC converters are listed with part number and estimated efficiency.

control temperature. Channel 1 delivers a fixed 12V to the control board and to the interface panel to provide 12VDC to the heat exchanger fans and to a 12VDC jack on the gantry stage.

On the control board, the 12V rail is distributed to three subcircuits: the LED driver, the motor drivers, and digital voltage regulators. The motor drivers utilize 12V directly for coil supply. The digital voltage regulation subcircuit consists of two stages. First, 12V is reduced to 5V using a Texas Instruments TPS84621. It is configured to produce the 5V rail, which is primarily used as the supply voltage for the onboard Raspberry Pi 4. It also serves as the supply voltage for the oxygen sensor. The 5V rail is also delivered to a 3.3V LDO regulator, whose output is the logic level supply for the microcontrollers, LED driver, motor drivers, and the I^2C bus. The final voltage conversion in the system is performed by a boost converter centered around the LED driver, which has an integrated boost controller. This is used to boost the output voltage to 30V, the supply voltage for the LED ring light.

Power Consumption

450W is more than sufficient for powering the system; however, it is still useful to have an idea of overall power consumption in the system. Table 3.5 lists maximum operating current for major power consumers in the system and the maximum current expected from that device. Current consumption for microcontrollers does not account for switching current on output pins, as the frequency is quite low and will be negligible relative to other power consumers in the system. There are other power sinks in the system as well, such as communication busses, passive components, and discrete ICs; however even in aggregate they are not significant enough to consider individually.

Table 3.5: Current draw for the SBX1

Device	Voltage	Max Current	S-S Current
ATMega328P (2x)	3.3V	20mA (10mA each) [84]	20mA
Motor Drivers (3x)	3.3V	36mA(12mA each) [85]	36mA
LP8860	3.3V	15mA [77]	15mA
LTC3886	5.0V	26mA [83]	26mA
Raspberry Pi 4 Model B	5V	3.0A [86]	1 A
Motor Coils (3x)	12V	3.0A (1.0A limited per motor)	0 A
Fan1	12V	1A	0.66A
Fan2	12V	1A	0.66A
Heater	12V/10V	10A	7A
Humidifier 1	24V	1A	0.5A
Humidifier 2	24V	1A	0.5A
LED Channels	30V	200mA	50mA

In addition to maximum current consumption, Table 3.5 shows the expected current consumption with environmental controls in steady state. For the Raspberry Pi, the 3.0 A estimate is based on the power adapter it is supplied with. Its actual consumption is dependent on the connected monitor and USB peripherals, but is typically closer to 1A. The motors only run intermittently, and the Z axis is programmatically incapable of running simultaneously with the X and Y axes. 10 V indicated for the heater is because its voltage fluctuates. With stable ambient

temperatures, a typical steady state consumption for the heater is 7A at 10V. The humidifier on-time is reduced near the target humidity and temperature. Additionally, the fans never run at 100% PWM, but rather runs at 66% during environmental control. Finally, only one LED channel will be active at any given time, consuming only 50mA. This means that while the maximum power consumption of the system is 262.53 W, during steady state it will consume less than half of that, near 116.6 W, with the bulk, by far, coming from active temperature and humidity control. If using passive humidity control, this is further reduced to 92.6W.

In addition to the endpoint power consumption for various ICs, sensors, and peripherals, there are conversion losses at each voltage reduction stage. These conversion losses must be taken into account to estimate total power consumption. This calculation is shown in (3.7), where P_x is the power consumption at voltage level x, not including consumption by other rails, and E_x is the efficiency of converting to voltage level x. Essentially, each rail's power consumption is calculated as the sum of its own power consumption plus the power consumption of its derivative rails, adjusted for efficiency: $P_{x_{tot}} = P_{derivative} + P_x$. This is a recursive calculation, which expands to:

$$P_{tot} = \frac{\frac{\frac{P_{3.3}}{E_{3.3}} + P_5}{E_5} + \frac{P_{30}}{E_{30}} + P_{12}}{E_{12}} + P_{24} + P_{AC} \tag{3.7}$$

Using values from Table 3.6 in (3.7) yields a conservative maximum power consumption estimate of 342.4 W, and steady state of 148.76W.

[4] No power factor is listed for the solenoids, but real power must be less than the apparent power of 5.5VA.

Table 3.6: Power consumption for the SBX1

Voltage (V)	Converter Efficiency(%)	Max Power(W)[4] [11]	S-S Power(W)
3.3	66 [86]	0.23	0.23
5.0	92 [87]	16.3	5.03
12/10	90 [83]	192	85.84
24	86 [88]	48	24
30	80 [77]	6	1.5
120	N/A	5.5	.55

3.5 PCB Design

For cost optimization, PCB size is restricted to 100x100 mm. Additionally, higher copper weight necessary for high current traces significantly increase PCB costs. For these reasons, the control and power management circuits are on separate boards. Finally, the control and power electronics must be physically separated from the high humidity environment, but must still communicate with the sensors, motors, and camera within the chamber, which led to the design of the interface board whose primary function is simply to act as a barrier between the electronics enclosure and the controlled environment. To further ensure no corrosion occurs which might damage the interface board, the connectors on the environment side of the board are sealed with potting compound.

3.5.1 Trace Size and Spacing

When current passes through PCB traces, their temperature increases. The degree of increase is dependent on a trace's current carrying capacity and the acceptable temperature increase above ambient. A low temperature increase is important not only to prevent immediate damage or fire from burned traces. Even if the circuit is functional, elevated board temperatures can significantly reduce the lifetime of components such as electrolytic capacitors. Additionally, elevated temperatures derate components, negatively altering circuit characteristics.

The amount of heat generated by a trace is primarily dependent on the trace's cross-sectional area and the current through that trace. [89] provides charts for temperature increase

as a function of cross-sectional area; however, a more useful tool is an adaptation provided by [90], which provides a calculator based on a curve fit from the charts in [89].

Most traces in the control and power boards draw low enough current that the restriction on size is the minimum of 8 mil imposed by the PCB manufacturer used by our lab. This includes communication between microcontrollers and the Raspberry Pi, SPI/I^2C traces, and control lines for the three buck and boost controllers in the system. These lines will draw no more than 50mA of continuous current, which amounts to only a 4 °C temperature rise [90].

Higher current traces have varying widths dependent on their maximum current potential and the copper weight of the board. For the power board, copper is $2\frac{oz}{ft^2}$. There are two outputs, each capable of delivering 12A maximum. These high current traces are a minimum of 200 mil for a 6 °C temperature rise [90]. These wide current paths are clearly visible as copper pours in regions A, B, and C of Figure 3.36 in Section 3.5.2. Upon entering the control board, the 12V rail splits into two branches, with one branch leading to the LED driver and stepper drivers, and the other supplying the 12V to a TPS84621 monolithic buck converter which steps down to 5V. The current maximum for the 12V rail on the control board occurs where both the LED driver and all three motors may pull at their maximum draw: 1A for each motor and 1.5A for the LED driver, and 1A for each fan at maximum. None of these should occur simultaneously; however, the design accommodates the maximum draw of 6.5A for this rail in case of faults or firmware bugs. The calculator yields a minimum trace width of 150 mils for a 10 °C temperature rise at 6.5A, but space constraints on the board do not accommodate a rail of this width Instead the rail was laid out as 100 mils but mirrored on the bottom copper and joined with vias and through-hole connectors, effectively doubling the cross-sectional area for the rail.

While each LED trace carries only 150mA at most, the diodes themselves have a significant heat output, as any power not emitted as light is emitted as heat. This heat must be dissipated to prevent damage to the board or diodes. In the case of the ML-E series LEDs, this is accomplished by connecting their thermal pad to the bottom side ground pad. The white and UV LEDs do not have thermal pads; instead, they are simply given wide (20mil) traces, and many

thermal vias which connect to large bottom side pours. The bottom side is then connected via a thermal pad to the aluminum ring light housing to act as a heat sink for the entire ring light PCB.

Other wide traces include the supply and output traces for the LED boost converter, motor coil traces, and the 5V bus, all of which are 20 mil to accommodate up to 1.5A of continuous current with less than a 10 °C temperature rise. The fan PWM line is 30 mil for the 2A maximum at 100% duty cycle.

There is also an isolated section on the board carrying 120VAC, with 30 mil traces. The current through these traces is not sufficient to require such wide traces. More important is the wide clearance of 50 mil between these traces to prevent arcing, which meets the IPC-2221 standard for trace clearance on a bare board with peak voltage of 170V on a trace [89]. Finally, on the interface board, 2 oz copper is used to allow narrower traces due to space constraints. Fan and humidifier circuits are 30 mils to accommodate up to 2.5 amps with 10 °C rise. The more important traces are for the TEC connections. These traces are 50 mil on top and bottom copper, joined with vias and through-holes. With the maximum 10A through the heater, this will result in a 20 °C rise over the trace. While this is higher than on other boards, there are no other heat producing components on the board other than the fan fault detection circuit and humidity switching FETs, which are kept well distant from the high current heater traces.

3.5.2 Layout

In addition to trace size and spacing, positioning of sub-circuits on the PCB is important to isolate digital, analog, and power circuits. Buck/boost circuits and motor control circuits produce high voltage, high frequency PWM signals which can cause interference with other circuits. This section discusses the layout considerations for the control and power boards.

Control Board

Each of the sub-circuits in the control board can be seen in Figure 3.35. Factors driving region placement include heat dissipation, ease of routing, and access when installed. Further discussion of each region follows the figure.

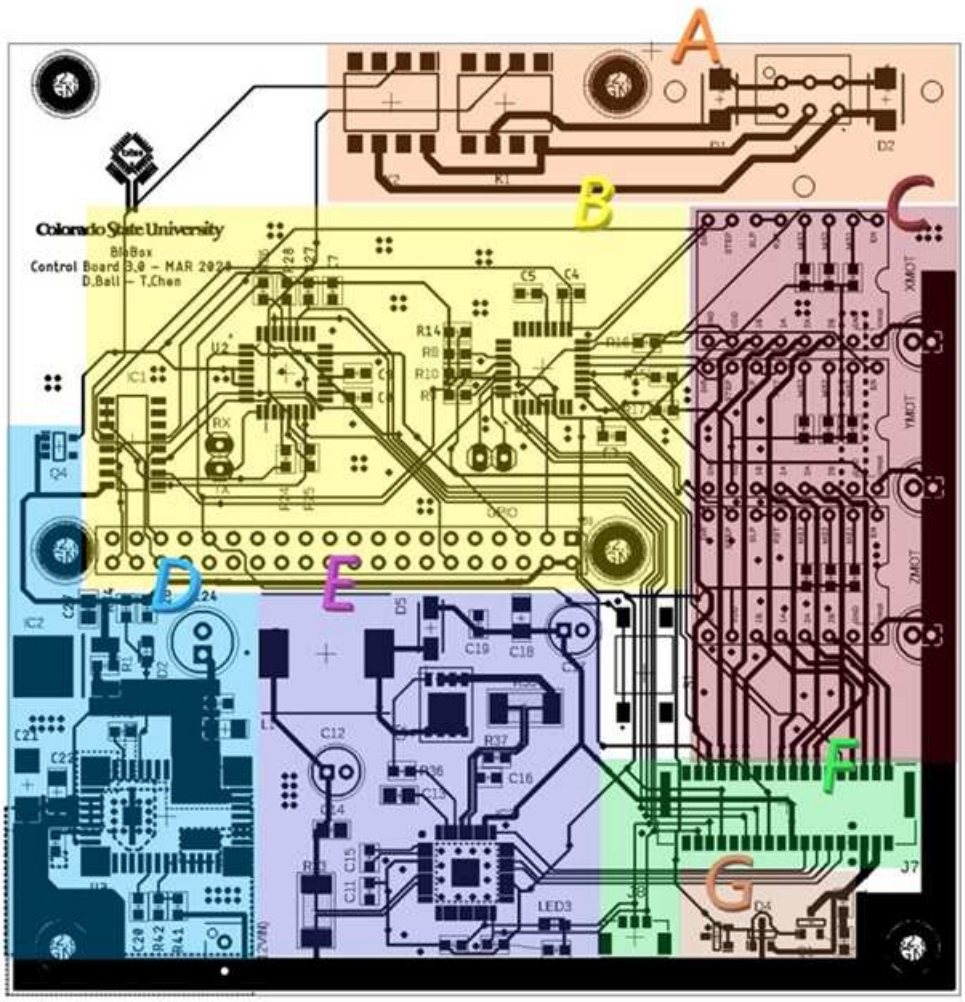

Figure 3.35: The layout of the control board, divided into functional regions. A) Solenoids, B) Control Circuitry, C) Motor Drivers, D) Power, E) Lighting) F) Headers G) Fan driver.

Region D is the power supply for the board. Thick copper pours provide high current distribution to the rest of the board. The power ground for this region is isolated from the rest of the board ground, joined only by a small bridge at the upper left corner of the TPS84621 buck

module. The other high frequency switching circuit on the board is to the right in region E, the LED driver circuit. In this circuit, the inductor is kept toward the other high-EMF components on the left half of the circuit, with the boost output, LED channels, and the I^2C connection on the right side of region E.

Another relatively high voltage and noisy PWM signal is that of the fan driver in region G. Most of the circuit is not particularly high voltage, and the frequency is only around 35KHz. The higher voltage portion of the circuit is 12V PWM, but this segment is kept short and next to the communication header where it exits the board. Region F is simply the headers for interconnecting cables, the control cable to the interface board, and the smaller I^2C cable to the power board for power monitoring and controlling the heater.

The other potentially noisy section of the board is above this section in region C. There is little here other than the sockets for the A4988 motor controller daughter boards. These are kept separate from the control board in case they burn out or are otherwise damaged. Under each daughter board are spaces for three 0603 chip jumpers. These correspond to MS[2:0] for each motor driver, controlling the microstep size for each axis.

Region B is the digital section of the board. The two QFN-32 footprints are for the sensor microcontroller (left) and motor microcontroller(right), with the 40-pin header below being used to mate with the GPIO header on the Raspberry Pi 4. To the left of the microcontrollers is the SPI mux used to select each microcontroller during programming.

Finally, region A is the 120VAC header and optoisolators, kept well above the other components. Additionally, the connector for the header is a Molex Microlock connector with no exposed conductors, and the optoisolators are beneath the Raspberry Pi when it is installed. These steps were taken to help prevent accidental contact with mains voltage during maintenance or assembly. There is exposed metal on D1 and D2, the TVS diodes; however, there are three holes in the PCB for mounting a shroud to cover these components.

Power board

The power board, shown in Figure 3.36, has a simpler layout than the control board. Discussion of each region follows the figure.

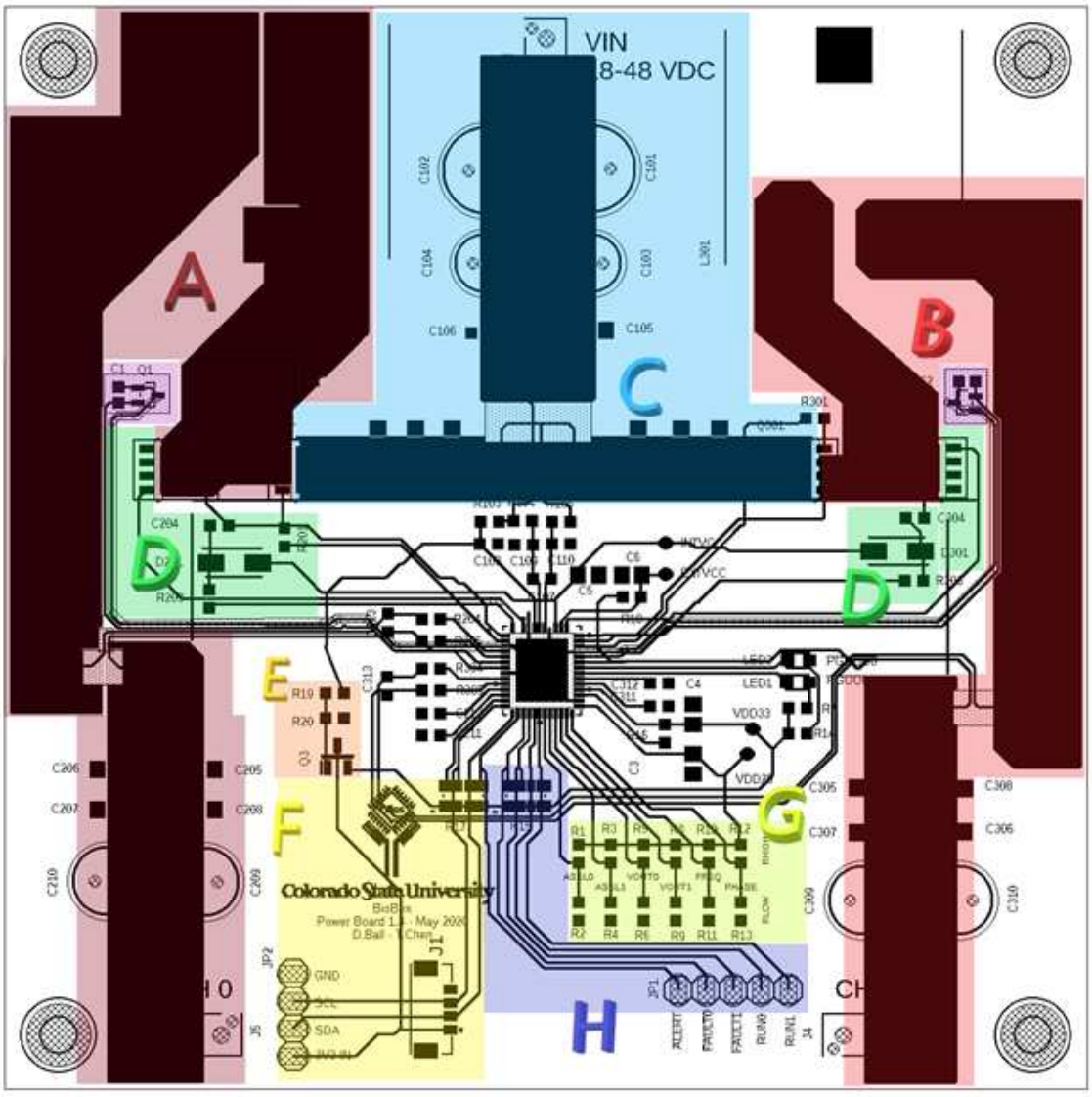

Figure 3.36: The power board consists of several regions. A and B are output channels 0 and 1 respectively. C is the input conditioning circuitry. D are the switching nodes for the output channels. E is to provide power for programming when no input power is supplied. F contains headers for programming and communication. H provides monitoring test points. G are unpopulated pads which may be used for hardware programming of each channel.

Input power from the system's primary power supply enters input conditioning region C at the Molex Microlock terminal VIN. The board can run on inputs from 18 to 48V, but if active humidification is required, this will be 24V as the humidifier supply taps directly from the primary power supply.

A high current rail delivers this power through the bulk and filter input capacitors to the switching nodes in region D. Regions A and B include the output components for channel 0 and 1 respectively. The inductors are situated to the top, well away from other components to help keep their dissipated heat well away from other components.

The highest temperature area on the PCB will be between the inductors and the switching nodes, near the FETs, which is the rationale for placing the diode connected transistors used for overtemperature fault detection in this region.

Below the input node and between the two output channels is the controller. The ground for this region is isolated except for two small junctions near the switching nodes. Here, region E contains a transistor used to route external 3V3 to the chip for offline programming. Region F is the communication channel, providing I^2C access to the chip. Region H provides access to fault monitoring pins. Finally, region G contains unpopulated 0603 chip resistor footprints. These may be used for overriding EEPROM output configuration.

3.6 Software Design

There are three main programs used in the SBX1. The graphical user interface (GUI), which runs on the Raspberry Pi 4, the sensor control firmware, and the motor control firmware, which reside on their respective microcontrollers. The heart of the system is the GUI running on the Raspberry Pi 4. In addition to the GUI, the Raspberry Pi 4 is responsible for programming each microcontroller using its SPI 0 connection.

Figure 3.37 shows the data flow through the system. The sensor controller firmware retrieves power status from the power supply chip and sends current voltage targets for the heater in accordance with the temperature control loop. Additionally, it receives gas concentration data

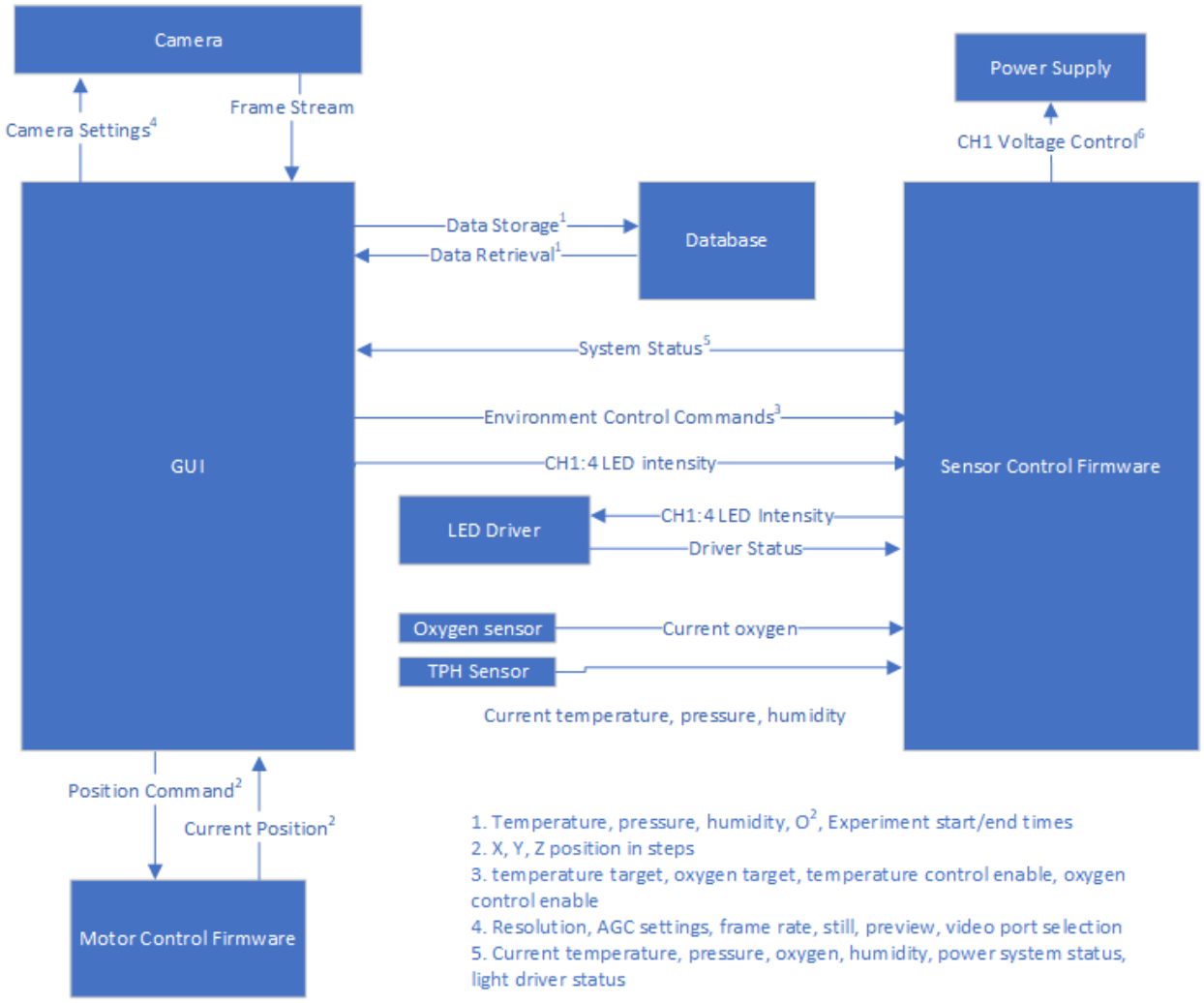

Figure 3.37: Data flow in the SBX1.

from the oxygen sensor. The motor controller receives control signals for motor movement and responds with the current motor position.

In the original software design, a database kept history in a MySQL database; however, the current version of the software has removed the database connection. While not in the current interface, it remains an intended feature for a future version of the interface. Finally, the camera provides a frame stream to the GUI. The GUI itself sends motor commands to the motor microcontroller, and environmental control and light level commands to the sensor controller. Combined with the data received from microcontrollers and the video feed from the camera,

the GUI presents a snapshot of system status to the user and allows controlling both the environment and the integrated microscope.

3.6.1 User Interface

The graphical user interface (GUI) provides a control and monitoring interface to users. It is divided into two tabs: main and automation. The main tab is used for manual control of the chamber and monitoring current system state. It provides a camera feed for the microscope, environmental control and monitoring, and microscope stage and focus control. Automation provides routines to the user for stitching and time-lapse.

GUI Layout

The main page, shown in Figure 3.38, provides quick access to commonly used features. The environment pane allows monitoring and control of the environment. Checking enable will enable control for that variable. Clicking apply will apply the current target value to the control variable. For all variables, the “current” column displays the current value reported by that sensor. Light controls allow controlling each LED channel independently. The positioning panel gives control over the motors. Users enter the desired target and move either by absolute or relative position by clicking the appropriate button. The bulk of the main page is taken up by the camera feed from the microscope. This feed has entries for the current stage position and a focus adjust on the right-hand side. In the lower left are quick access controls for video recording, a snapshot, and autofocus.

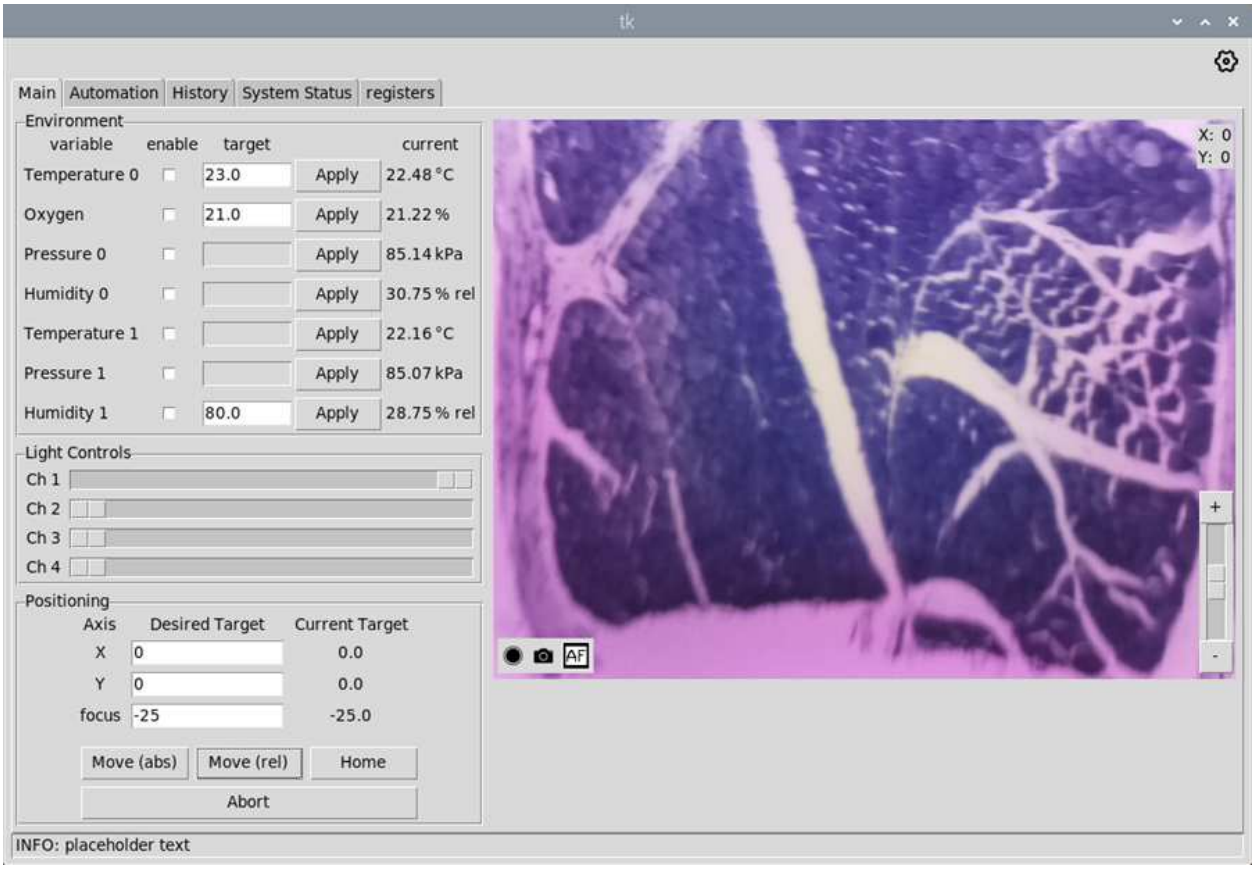

Figure 3.38: User interface displaying the main tab. The display is focused on cross-section of dog skeletal muscle from Amscope prepared slide set PS25.

The Automation tab is selected in Figure 3.39. This tab is the work of Ryan Barnes, one of the BLISS labs Senior Design students for 2020-2021. Ryan implemented several functions for the SBX1. First, an image scanning algorithm which will take a series of images over a pre-defined region. The user sets the upper left and lower right corners of the scan range, as well as the microscope objective. The system will then automatically scan over the region to capture a grid of overlapping images.

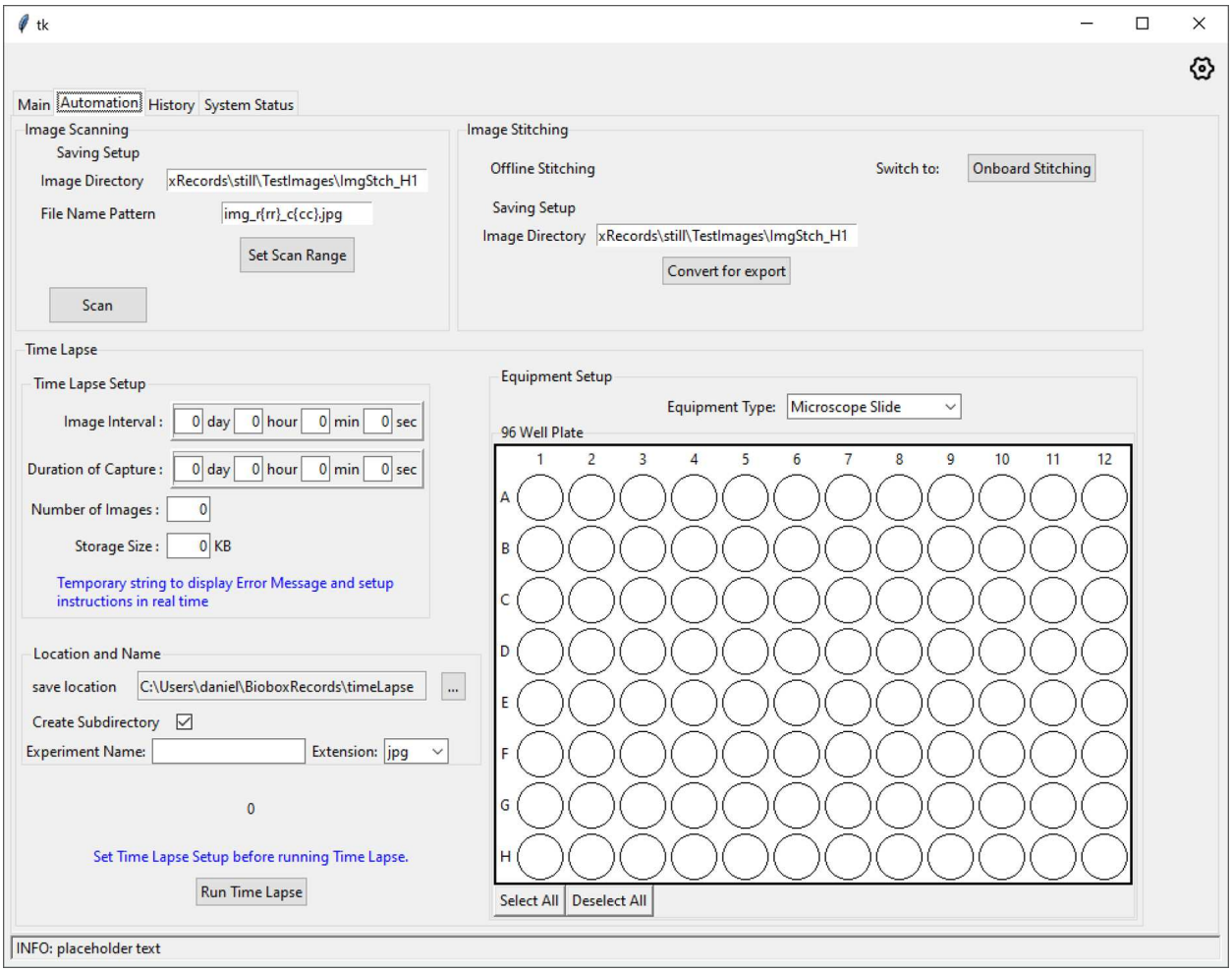

Figure 3.39: GUI with Automation tab selected.

These images can be used with an external image stitching tool to create a high magnification image far larger than the field of view of the microscope. Finally, time-lapse images can be taken for a variety of equipment types. The user selects which wells or the region they wish to capture, followed by the interval between images and the duration of the time-lapse. The system will scan over the specified areas once per interval, creating a time-lapse series at each location.

Program Structure

The GUI is written in python using the tkinter library, which is an interface for the TK GUI toolkit. The program functions through a single main loop which handles events triggered since

the last entry into the loop. Classes are compartmentalized to provide specific functionality to sections of the GUI. The typical pattern for a class is to inherit the tkinter Frame class to be placed within the GUI. Some classes are passed as objects. These may or may not also inherit from Frame and have a user facing interface.

Config Config is an extensible class which uses the tkinter Tree to create a popout window for configuration when the gear in the top right corner is clicked. It allows configuring system parameters which will be less commonly used, such as resolution and file automatic numbering behavior. The interface is constructed as a dictionary internally, then the tree is built by recursively traversing the tree to build the user facing interface, seen in Figure 3.40.

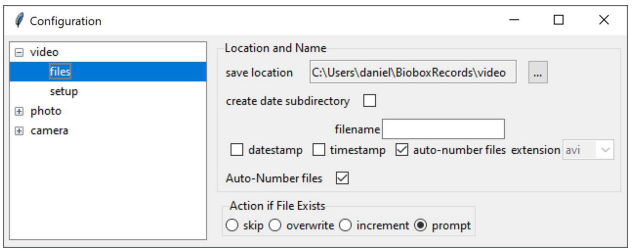

Figure 3.40: The GUI configuration popup window.

SpiComm The *SpiComm* class provides a handle for communicating with the sensor controller. This class is responsible for communication with the sensor microcontroller. It implements several wrapper functions for performing reads/writes with the software registers, as well as calculating the 8 bit 1's complement checksum for SPI transactions. The datagram format as well as the parsing flowchart is described in paragraph 3.6.2. The SPI interface itself is built around the *pigpio* library and requires the *pigpiod* daemon to be running on the Raspberry Pi. This daemon must be added to the pi's startup services to ensure it is launched at boot.

Motor Control The *motor.Controller* class implements communication and control for the stage and focus motors. It implements the I^2C protocol for motor control and position track-

ing. An instance of the class exposes wrapper functions to send commands to move, home, and abort. It provides error handling as well. Unlike *SpiComm* which has a checksum, motor commands are sent unchecked. The largest reason for this is simply that motor commands must be received and quickly processed to minimize interruptions in travel. It is unlikely to be an issue due to the small datagram size and the repeating nature of motor commands. The *motor.AxisFrame* class provides tracking for current and target position, and a validated numeric entry field for position entry by the user. The *motor.ControlWindow* class combines one *motor.AxisFrame* instance per axis and an instance of *motor.Controller* to provide motor position tracking and a user interface for motor control in the form of absolute or relative step movement inputs for each axis. Absolute moves, aborts, and home commands are sent directly to the microcontroller. Relative moves perform the calculations based on current position to send an absolute position move command.

Lighting One of the simpler portions of the code, the lighting classes implement LED adjustment sliders. Each slider sends its value whenever movement in the slider is detected to ensure LED intensity adjusts smoothly. Slider scales from 0 to 255 (4095 for channel 1) to allow directly passing LED current values directly to the controller chip without additional processing on the sensor controller.

Registers This file contains a map which matches the registers' associated address offsets stored in a header file, "registers.hpp". The registers are listed listed in Table 3.7. It is important that this file matches the GUI's "registers.py" file to prevent reading/writing incorrect locations on the sensor microcontroller. The registers class also contains a bit mapping enumeration for system control bits.

BMEx registers provide temperature, pressure, and humidity data from the BME280 sensors. GAS_0 provides oxygen measurements, while GAS_1 is a placeholder for an additional sensor in a future version. LED1:4 provide control over LED intensity. SBX1_STATUS contains system flags. Currently it is only used to test whether sensors are responding, and to retry if they

Table 3.7: Software registers for the sensor microcontroller firmware. These registers provide a communication interface between the Raspberry Pi and the rest of the SBX1, excluding motor control.

BME0_T	PWR_STATUS_INPUT
BME0_P	PWR_STATUS_CML
BME0_H	VOUT_SET_ATMEGA_0
BME1_T	VOUT_SET_LTC3886_0
BME1_P	VOUT_CURR_0
BME1_H	IOUT_CURR_0
GAS_0	STATUS_WORD_0
GAS_1	STATUS_VOUT_0
LED1	STATUS_IOUT_0
LED2	STATUS_TEMP_0
LED3	STATUS_MFR_SPECIFIC_0
LED4	VOUT_SET_ATMEGA_1
SBX1_STATUS	VOUT_SET_LTC3886_1
CONTROL	VOUT_CURR_1
SET_T	IOUT_CURR_1
SET_G	STATUS_WORD_1
SET_H	STATUS_VOUT_1
PID_kP	STATUS_IOUT_1
PID_kI	STATUS_TEMP_1
PID_kD	STATUS_MFR_SPECIFIC_1
PID_e	
PID_P	
PID_I	
PID_D	

are not. CONTROL contains a bit mapping for enabling or disabling environmental controls. SET_x stores environment variable target values. PID_kx are PID controller constants. Using registers for these values rather than hardcoding them allows live tuning of the system. PID_x are the actual PID variables. VOUT_SET_ATMEGA_x is the voltage setpoint for channel x set in the microcontroller, while VOUT_SET_LTC3886_x is the setpoint in the power controller itself. VOUT_CURR_x is the measured voltage for channel x, and IOUT_CURR_x stores the measured current for channel x. The remaining registers are used for detecting power faults and debugging.

Environment Panel The classes on the controller side of the environment panel are responsible for relaying updated sensor data to the user and relaying user commands to the sensor microcontroller. User updates are immediately relayed to the sensor microcontroller to facilitate a responsive experience for the user. The sensor microcontroller is polled every second. In the event of a read failure, the microcontroller will be polled again every 100ms until successful.

Camera and Display The display frame gets its images from the system's camera 0 input. It uses a python implementation of OpenCV (https://pypi.org/project/opencv-python/) to pull images from the Raspberry Pi Camera V2.0 connected to the computer's MIPI-CSI2 port.

Upon instantiation, the class's loop function is initiated and a frame capture thread is spawned. The frame capture thread launches an update method. This will first ensure that a camera feed has been acquired. If not, it will attempt to acquire (or re-acquire) the feed. It will load a dummy image as the next frame to notify the user of the issue acquiring a camera, then return. If the feed has been acquired, the thread will begin acquiring the next available frame at 3280x2464 pixels, which is saved as a cv2 array. This raw frame is stored for full resolution tasks. Additionally, the frame is resized and saved as a 640x480 PIL image. Should any errors occur, the dummy image is loaded and the thread begins attempting to reacquire the camera. Back in the main thread, the camera loop tests to see if the update thread is still alive. If the frame has terminated, then a new frame has been acquired and the display will be updated with the new frame.

In addition to the video feed, the display has a few additional controls for quick access. Movement and motor position widgets have been implemented graphically but they currently do not update positions or send movement commands at this time. Development on these features ceased due to plans to transition the interface to the Qt toolkit; however, their current implementation will still be useful for future versions of the GUI. If the user moves the cursor over the display, the cursor changes to a cross as an context clue to the user that the effect of a mouse click has changed. On a mouse down event (i.e. clicking but not releasing the mouse button), the cursor changes to a Fleur. When the mouse is dragged, a line is drawn between he

initial point and the current position. At subsequent drags, previous lines are erased and a new line is drawn, creating the effect of a line with a fixed start and an endpoint which tracks the cursor. In future implementations, the direction and length of this line will cause the stage to move at a correlated vector, creating the effect of the user "dragging" the stage with the mouse. For Z axis control, a tkinter slider widget was modified to snap back to the center when the slider is released. The relative position of the slider would determine the direction and speed of the Z axis motor.

The display frame class provides a modular widget toolbar which allows creation of a button and a custom callback for each button. At this time, these buttons are a record feature which will initialize a video recording when pressed and stop the recording when pressed again. The snapshot button stores the latest full frame as an image. The file formats for image and video are determined in system configuration. Video configuration additionally allows changing the frame rate of recordings for quickly starting time-lapse video at the current location.

Automation

Time-lapse, image stitching, and autofocus algorithms were implemented in the user interface by Ryan Barnes for his Senior Design project, part of the Electrical and Computer Engineering curriculum at CSU. Ryan had minimal guidance from myself and Professor Chen beyond providing design specifications and advice for optimization. For manual use, autofocus is merely a convenience. But when the system is performing automated tasks with no user input, it becomes a necessity. For example, when performing time-lapse imaging over multiple regions, even if the user specifies a depth for each position, samples may move vertically through a suspension. Autofocus would allow attempting to track movement vertically as well as horizontally through the medium over time. XY stitching is a common task for large samples, allowing the creation of a composite image from multiple images taken over a large area. These images are useful for visual analysis by the microscope technician, as well as for computer vision tasks over a large area while maintaining a high magnification. Time-lapse imaging is useful for following trends or monitoring cell growth.

Autofocus A focus measure for an image is a mapping of an image to a value which quantifies the level of contrast in the image, representing the degree of focus in the image. This score can be obtained by convolving a kernel over an image, then summing the values of the convolution [91]. The kernel used in this implementation is a 1D gaussian derivative, and only a fraction of columns are convolved to save time. Once focus scores have been calculated over a range of Z heights, the scores are interpolated, and the global maximum of this interpolation is computed. This determines the focus point, and the Z axis moves to that position. The flowchart for autofocusing is shown in Figure 3.41.

Backlash compensation is accomplished by always approaching target positions from below. For autofocus, sample images are taken at regular intervals starting from relative position 0 and moving up until some total number of steps Z have been taken for the final image. After interpolation determines the distance to the point of maximal focus f . The Z axis then reverses direction and travels $f + B$. where B is some distance greater than backlash in either up or direction. This movement is subject to backlash $b1$, incurred by transitioning from upward to downward movement. Thus, the microscope will be at position $f - (B - b1)$. The Z axis then reverses direction again and moves up by distance B, incurring backlash $b2$ from transitioning from downward to upward movement. The final position is therefore $f - (B - b1) + (B - b2) = f + b1 - b2$.

In the ideal case where $b1 = b2$, the backlash is fully cancelled, and the final position will be exactly at the calculated point of maximum focus. In reality, the final position will be offset by $b' = b1 - b2$. There is also some lateral movement caused by the carriage rocking clockwise or counterclockwise against the dovetail guide, depending on upward or downward movement; however, this error will be negated because travel will always be in the upward direction for the stopped position.

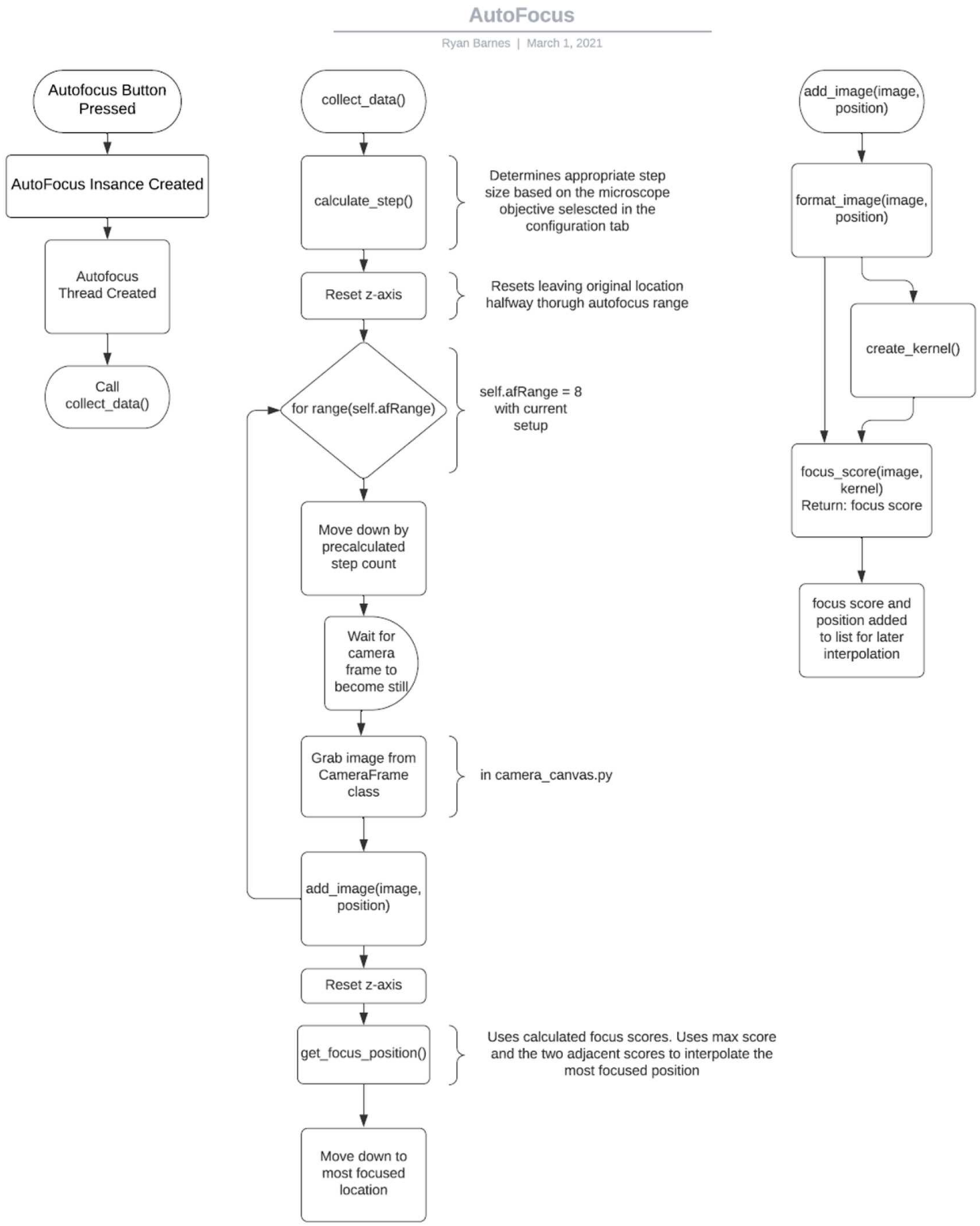

Figure 3.41: Flowchart depecting the basic process of the autofocus algorithm.

XY Stitching XY stitching requires a set of overlapping images. By clicking "set scan range" in the scanning panel (Figure 3.42) in the automation tab, the user is presented with a pop-up allowing motor control and instructions to select an upper left corner. Once the user has selected the corner, they are then instructed to move the stage to the lower right corner of the range to be scanned. Once the user has selected the scanning area, they should close the popup and click the "Scan" button to begin automated scanning of the specified region. The distance to travel per image is then calculated based on the currently selected objective lens to create sufficiently overlapping images for MIST, named by row and column.

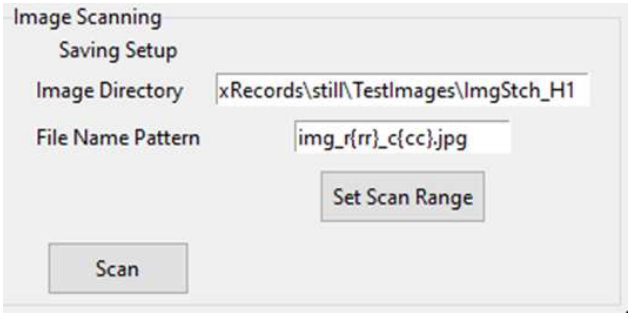

Figure 3.42: The image scanning section image stitching configuration is used to capture a series of images over a two dimensional region of the sample at a fixed depth.

Images must be exported from the SBX1 to a Windows PC via thumb drive or network connection. From there, they can be imported into the image stitching tool for processing. The stitching GUI is a wrapper, written by Ryan Barnes, for the open-source Microscopy Imaging Stitching Tool (MIST) developed by the National Institute for Standards and Technology (NIST). The GUI is shown in Figure 3.43. Users can specify which rows and columns to use out of the set, and the formatting of the filename pattern. They can also configure the blending of image edges for a more uniform appearance of the stitched imaged.

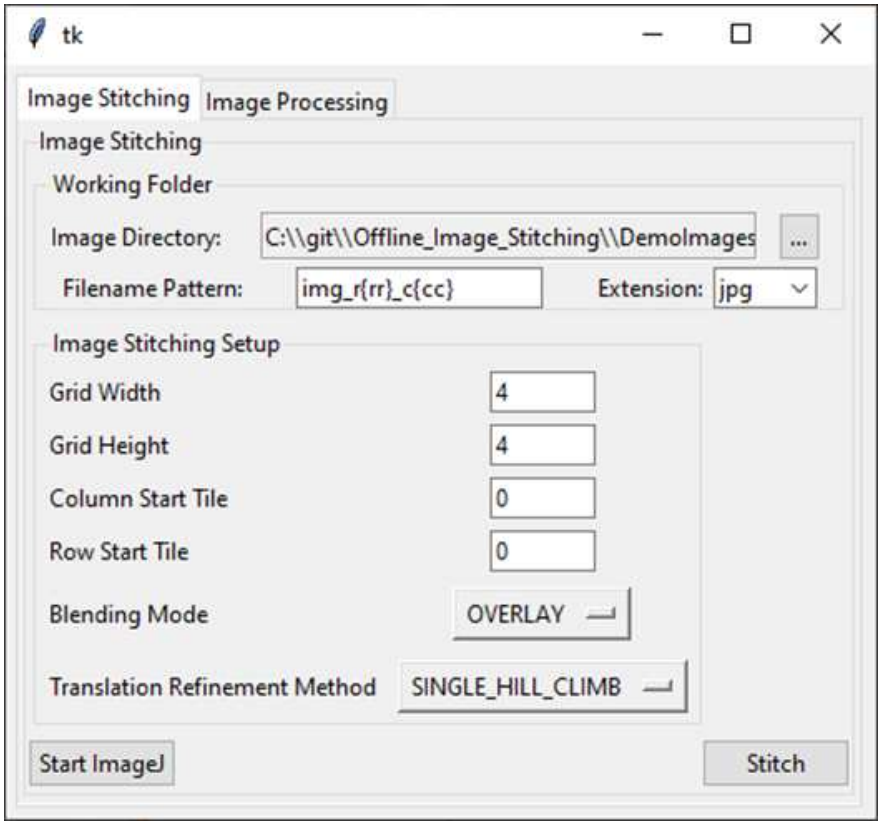

Figure 3.43: The user interface for the image stitching program.

Time-Lapse Imaging Time-lapse images can be taken over a range of positions selected by the user. Options for positions are determined by the equipment pane in the automation tab of the UI, shown in Figure 3.44. For a well plate, users are able to select which wells they would like to be imaged. Slides and dishes are not yet implemented, because the stage is not keyed and it is not possible to accurately orient the dish/slide for the UI to "know" where it is. Once the keyed stage has been manufactured that algorithm will allow selecting from a grid of positions for larger wells, dishes, and slides. In the short term we may implement a region to scan as with XY stitching.

Once the positions to be captured are selected, users fill out an image interval and duration of capture or number of images per position. To prevent the user from specifying an interval which the system could not accommodate due to excessive travel time, Ryan developed an algorithm, seen in Figure 3.45, which would estimate the total time for a full set of images at all

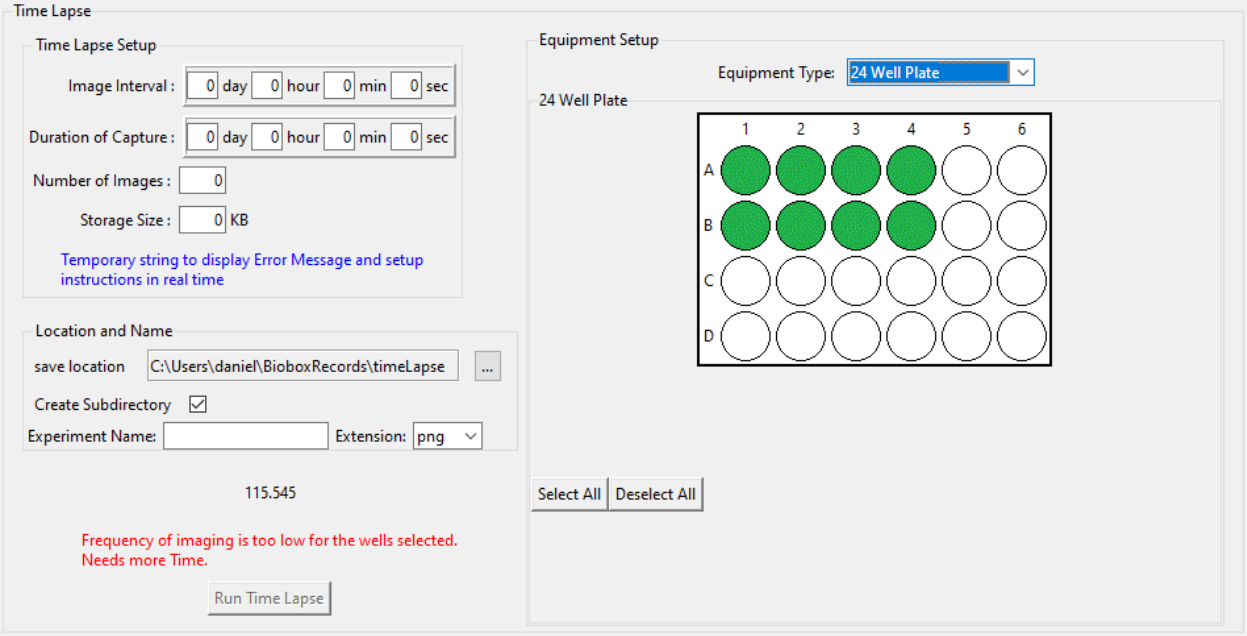

Figure 3.44: Interface for configuring time-lapse scanning with 24 Well Plate selected.

positions. The algorithm sums the total distance traveled, the number of turns, and the number of stops. Each value is assigned a time multiplier to determine the total time per cycle. When the user's inputs are accepted, they must then specify a location to save the file and can then begin the time-lapse. From this point, every time the image interval is passed, the system automatically moves to each successive position, capturing an image at each stop. In this way there will be a time-lapse series with the specified interval for each location.

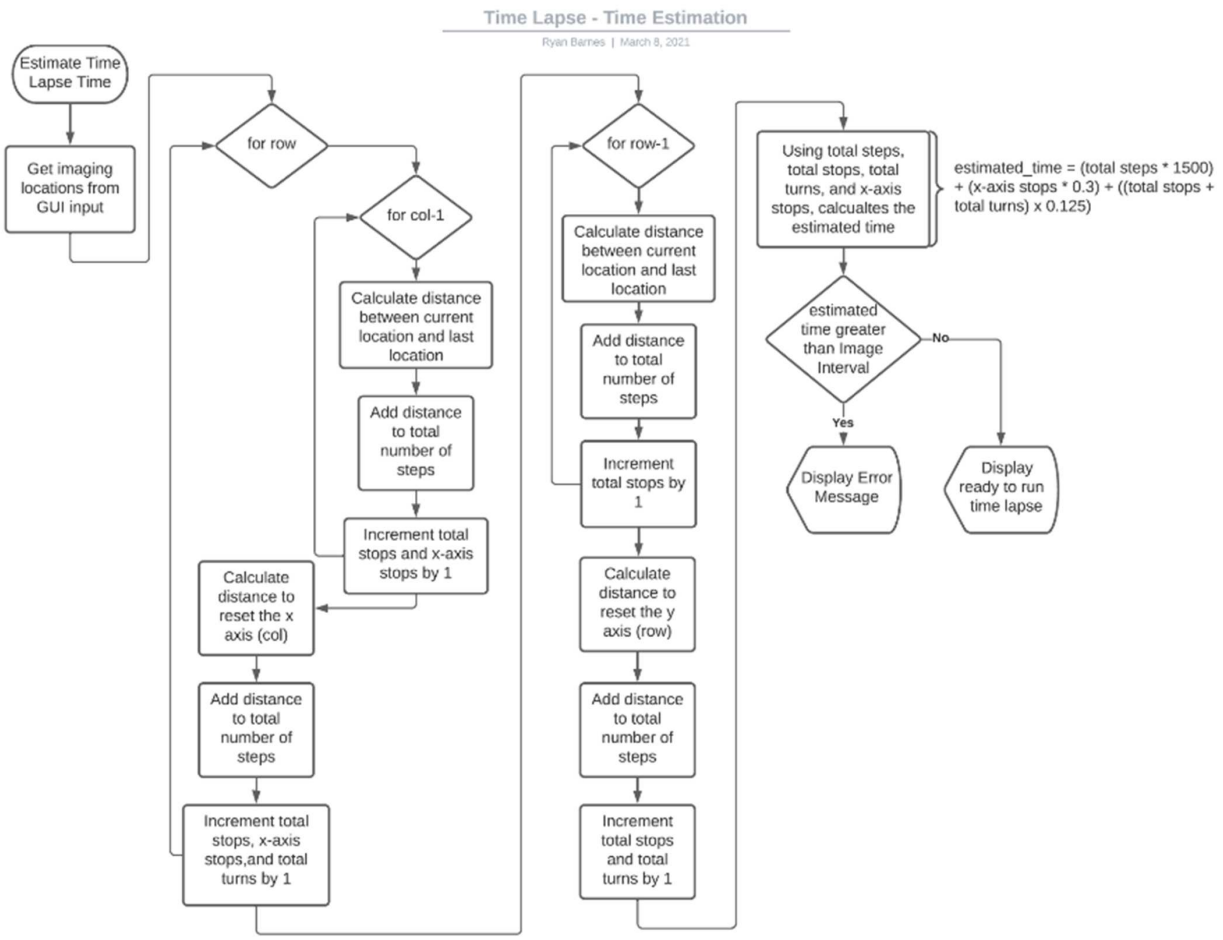

Figure 3.45: The algorithm flowchart for time-lapse estimation, used for determining the minimum interval for time lapse automation based on the distance the stage must travel per interval.

3.6.2 Firmware

Firmware for the system resides on the sensor and motor microcontrollers. It is programmed in C++, compiled with AVRGCC, and programmed using AVRDUDE.

Sensor Microcontroller

The sensor microcontroller is responsible for all sensor monitoring and environmental control systems. Each controller and sensor is designed as a class with an init() and a loop() function, which are to be called in the respective segments of the main loop.

Sensor Monitoring There are three sensors in the system. Two are Bosch BME280 temperature, pressure, and humidity sensors on I^2C channels 0x76 and 0x77. Sensor data is retrieved using the Adafruit BME280 library. The third sensor is a Luminox LOX-02 sensor. The LOX-02 sensor broadcasts a string matching "O xxxx.x T yxx.x P xxxx % xxx.xx e xxxx\r\n" using RS232 protocol every 2 seconds. The relevant section is the substring matching "%xxx.xx", which is parsed into a float for the current oxygen percentage. All of these values are stored in their respective state registers.

Controllers Each environmental control drives a different actuator to influence an environmental variable. Temperature is controlled using I^2C to command the power board's LTC3886 buck controller to set the channel 1 voltage level, adjusting the output of the heating element. If active humidity control is configured, then pins 4 and 5 are used to control the humidifiers. Gas concentration is controlled via pins 12 and 13, controlling oxygen and fill gas solenoids, respectively. LEDs are controlled using I^2C to communicate with the on-board LP8860 LED driver chip, which in turn sets output levels for each LED channel. Fan PWM for air circulation (both internal and external to the box) is directly applied to pin 1.

The actual environmental control algorithms are simply software implementations of the flowcharts from the environmental control section. In addition to these algorithms, there are control loops for the LEDs and fan speed.

Fan speed is controlled using the ATMega328P's Timer2, configured as seen in Table 3.8. The waveform generation mode (WGM) bits are set to 7 to enable fast PWM mode. COM2B1 is set to enable toggling pin1 whenever OCR2A matches the timer counter. Finally, clock select (CS2) bits are set to 0x01, indicating no clock prescaler. Timer2 runs on a 256-bit counter, and the system is running on an 8MHz internal clock, thus the PWM frequency is 31.25 KHz. The PWM duty cycle is configured by setting the timer counter to a value less than 256, with 0 being 0% and 255 being 100%.

LEDs are configured by setting a brightness value to its associated register. This value will be read during the loop and sent to the LED driver. For values greater than 0, the value is written to

Table 3.8: PWM timer configuration enabling a 31.25KHz output for driving the system fans.

Setting	Value	Effect
COM2B	0b01	Pin 1 toggle on limit reached
WGM	0b111	Enable fast PWM mode
OCR2A	MAX_PWM	Initializes duty cycle to 100%

the corresponding current control register for the channel. For a value of 0, the PWM is instead set to 0% to protect the chip, per [77]. Current rather than PWM control is used to prevent banding in the camera feed. One important consideration is that the channel 1 brightness register has 12 bits, while channels 2, 3, and 4 have only 8. The number of bits transferred is restricted in the GUI by the maximum value on the brightness slider for each channel. For all channels except channel 1, the LSB is written to the register. For channel 1, the MSB of the brightness value is written first, followed by the LSB. This order of writing must be followed, or the driver will not accept the value.

Timing Except for the LEDs and SPI communication updates, all control and sensor updates rely on an instance of the *EggTimer* class set to two seconds for timing. The class's ding() function will return true if the configured time has elapsed since the timer was set or since the last time it was called and returned true. LEDs and SPI communication must be as close to real time as possible. In the case of SPI a fast response is vital to prevent communication errors. In the case of LEDs, a fast response is necessary to ensure light intensity transitions smoothly in sync with the GUI slider moving.

Communication Protocol There are a several considerations for the communication protocol. Special care must be taken during SPI communication as there is only a single register on the ATMega328P. The byte in the SPI register will be transferred and replaced with the incoming byte from the GUI. Further, the SPI interrupt subroutine is triggered for each byte received, meaning the subroutine will return to the main loop after each byte is received, making

read-while-write errors a possibility in the control loop if a register is updated. In addition to limitations in hardware, errors may occur during transfers. Corrupted transfers could result in incorrectly reported information at best, and incorrectly set target registers at worst, resulting in incorrect or invalid set points or configuration. There are also varying numbers of bytes to be written or read based on the intended operation.

A software register based protocol for communication was developed to address some of these issues. The syntax for MOSI and MISO data for a message with a payload of length N is laid out in Table 3.9.

Table 3.9: Structure of a SPI interaction between the GUI and the sensor microcontroller on MOSI and MISO lines

Position	**0**	**1**	**2**	**3**	**3+N**	**4+N**
MOSI	RD/WR	Start	Length	Data	Checksum	0x00
MISO	ACK/NAK	0X00	0X00	Data	TX checksum	RX checksum

For the incoming message, the first byte indicates that the specified registers should be read or written. The second byte indicates the starting register number. The second byte indicates the number of bytes to read/write starting from that number. This is not specified as a number of bytes because register length is not fixed. The third block is the data itself, containing a number of bytes equal to the specified length. Current register contents are transferred regardless of whether a read or write is specified. The penultimate byte is the checksum for the message. The final byte should always be 0x00.

Because the byte in the SPI data register is shifted out when a new byte is received, the "byte out" must be pre-loaded. The first byte sent when the read/write byte is received will be ACK(0x06) or NAK(0x15), which indicates the current state of the message handler. ACK indicates the previous message was successfully processed. NAK indicates there was a fault in the previous message processing (likely due to a checksum failure but could indicate other

protocol issues). Starting at the second byte received the next byte of the requested register will be preloaded into the SPI data register on the microcontroller. This way, starting at byte 3 the response byte will be the requested data, up until the penultimate response byte. This will be the TX checksum. This value is the checksum for the outgoing message. The final byte will be the RX checksum, which is the result of the checksum for the incoming message, which should be 0x00 unless a checksum error occurred. This allows the Raspberry Pi to identify when its message was corrupted on the microcontroller as well as verify the integrity of the response data.

When the final byte is received (4+N), post-processing must be performed. First, the status byte must be pre-loaded for the next message. 0x00 will be sent for a read. For a write, ACK is used to indicate a successful write, while NAK indicates that registers were not written due to a checksum failure. Finally, the rx checksum is reset and the tx checksum is set to the preloaded first byte.

Registers To conserve memory, firmware registers use datatypes only large enough to store the required values. This structure means that extra processing is necessary when reading or writing to registers to ensure the correct data type is written to the correct index of the register array. This is accomplished using a register class. The class provides three features:

- A register array containing all software registers sequentially.
- An enumeration, associating each register with its starting index within the register array.
- A set of template accessor functions which simplify reading and writing variable length registers.

The accessor functions, listed in Table 3.10, are used to reduce the likelihood of memory access bugs in the firmware. This is accomplished by obfuscating reinterpret casts necessary to write values of any type at a specified memory index in a byte array. During compilation, the type is inferred by the function parameters and left side of an expression, so the type need

not be specified by the programmer. The result is more readable code which is protected from memory access errors common to pointer manipulation.

Table 3.10: Register accessor functions in sensor microcontroller firmware simplify accessing data of different types stored contiguously in a byte array.

Position	**0**	**1**	**2**	**3**	**3+N**	**4+N**
MOSI	RD/WR	Start	Length	Data	Checksum	0x00
MISO	ACK/NAK	0X00	0X00	Data	TX checksum	RX checksum

There is still some risk if the programmer specifies a register which does not match a destination type for a read, or an incorrect parameter type for a write. In the best case, the returned or written value will be incorrect for the register. In the worst case, it will cause a memory access fault by reading or writing beyond the bounds of the array. It is possible to check for these faults, but the program space on the microcontroller is limited, so instead the programmer must simply take care. It is equally important that the specified start indices are correctly enumerated for each register, or other registers might be overwritten, or a memory access error might occur.

Motor Microcontroller

The motor microcontroller is intentionally simple, with the expectation that the GUI will handle backlash compensation and position tracking. The control loop is driven by I^2C communication initiated by the system GUI. A motor control message is an SMBus style block write:[command][data length][data].

The receipt of an I^2C command or request triggers an interrupt. The high level flowchart for the interrupt handlers is shown in Figure 3.46.When a block write is received, the command is recorded, and any command parameters are written to the receive buffer. Finally, a flag is set to notify the main loop that a new command has been received and must be processed. The

only other communication is an I^{2}C block read. When this occurs, the system will update the transmit buffer with the current position and write the transmit buffer to the I^{2}C bus.

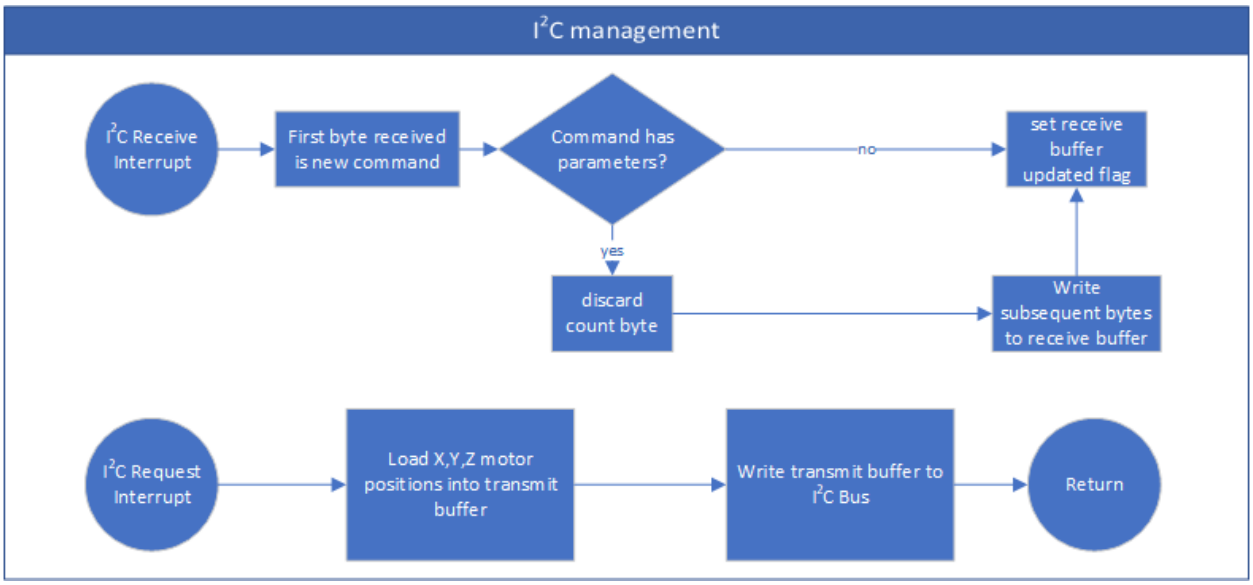

Figure 3.46: Motor controller interrupt subroutine flowchart. An I^{2}C receive or request triggers their respective interrupt subroutines. Data is processed quickly if possible, or a flag for processing is set if not

The main loop is very simple. If a command was received since the last pass through the loop, the new command will be processed. Move commands trigger a move to a specified absolute position. Abort commands send a stop command to each motor, causing them to immediately decelerate to a velocity of 0. A Home command initiates a homing cycle for each axis.

After any new commands are processed, the Z axis is commanded to "run". If the trigger time for a step has been passed, the motor will be commanded to step. If the motor is currently homing, the limit switch will be queried. If reached, the current position will be set to -100 and a new position of 0 will be commanded to back off of the limit switch. Finally, the next step time is then calculated based on configured acceleration and maximum velocity settings. If the Z axis has reached its destination, then the X and Y axes will be commanded to run. The main loop then repeats.

The current acceleration and stepping control is managed by the AccelStepper class from AirSpayce (https://www.airspayce.com/mikem/arduino/AccelStepper/index.html). This library is GPLv3 licensed; which is not viable for closed source software. This means that should the product be shared, either the commercial license for the library must be purchased, or the motor control code must also be GPLv3 licensed and made freely available. This is unlikely to be an issue in the future as the gantry (and its controller) will be redesigned prior to a commercial model being available.

3.6.3 Utility Software

Several utility programs were written to assist with setup, control, or troubleshooting of the SBX1. These are not intended for use by an end-user.

The LP8860 EEPROM manager, shown in Figure 3.47, allows direct control and manipulation of the LP8860 LED driver. This software requires its own firmware (manualcontrol.cpp) to pass data between the Raspberry Pi and the LED driver. It is only necessary during initial setup of a control board or to troubleshoot a malfunctioning driver.

Programming the microcontrollers is done using the open source software AVRDUDE ([92]). The program is used to upload .hex files exported from the Visual Studio Code plugin PlatformIO to program the motor and control chips. Frequent firmware writes were necessary during develoment and command line entry became cumbersome particularly ensuring the correct controller was selected to program. To streamline microcontroller programming, a GUI wrapper, shown in Figure 3.48, was written for AVRDUDE. It allows quickly and easily testing the connection from the Raspberry Pi to the microcontrollers, writing the fuses with the correct internal clock configuration, and writing firmware.

The System Status and Control program works with the production firmware. It allows direct monitoring, logging, and manipulation of each software register in the sensor controller, as well as live monitoring plots for each register. This software is vital for both troubleshooting and system tuning and calibration. It functions by providing a mirror of the registers in the

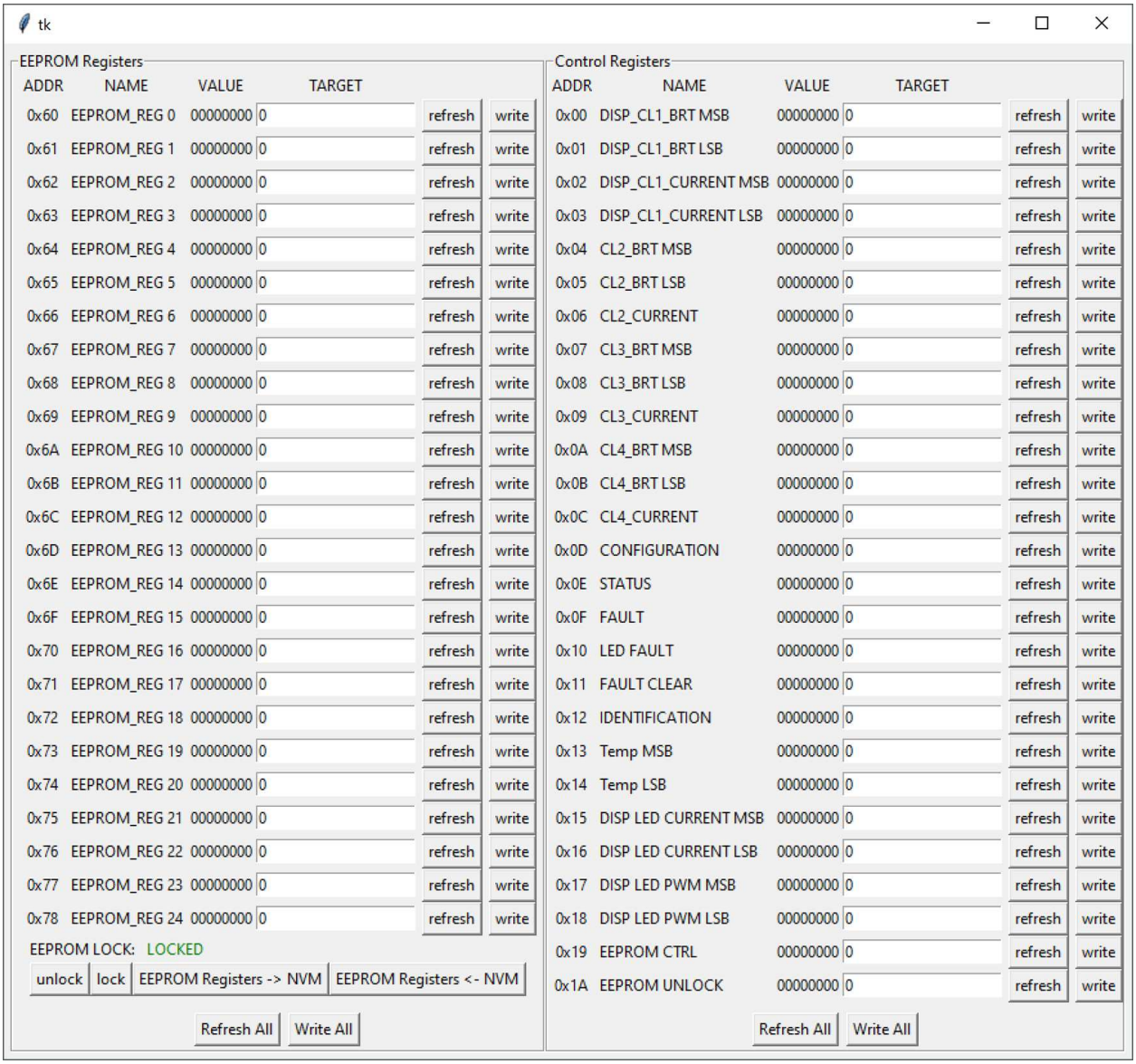

Figure 3.47: The GUI for the LP8860 EEPROM Manager is used only during initial configuration of a control board, when the EEPROM is flashed.

sensor microcontroller. Current values are displayed to the user, as seen in Figure 3.49, and each register has an entry which allows writing to registers for direct control. It can also log any selected registers to a file for later processing.

This software also provides an interface for logging the values of selected registers to a file. These logged values can then be used for plotting and analysis in external software. This feature was used during the calibration of the temperature sensor by logging the sensor and voltage

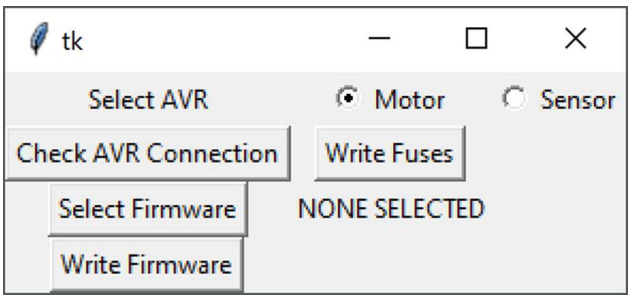

Figure 3.48: The GUI wrapper for AVRDude allows quickly selecting the desired AVRDude operation and provides a file browser to locate the .hex file target.

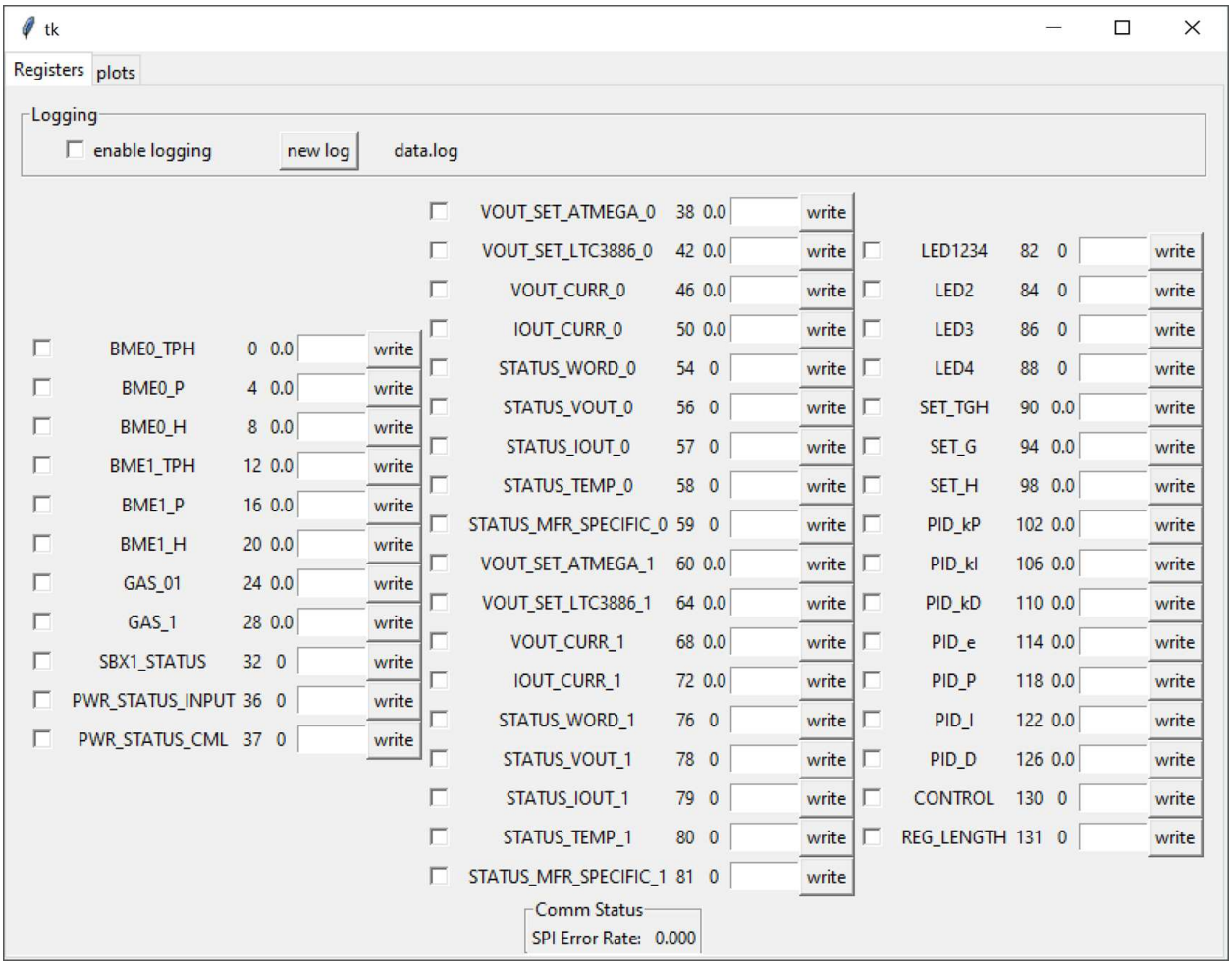

Figure 3.49: The system Status and Control program displaying register monitoring and control as well as logging configuration.

outputs with a step input to characterize the plant. There is also a live plotting tab which can display historical plots for up to 6 registers, with two registers per plot on three plots, as seen in Figure 3.50.

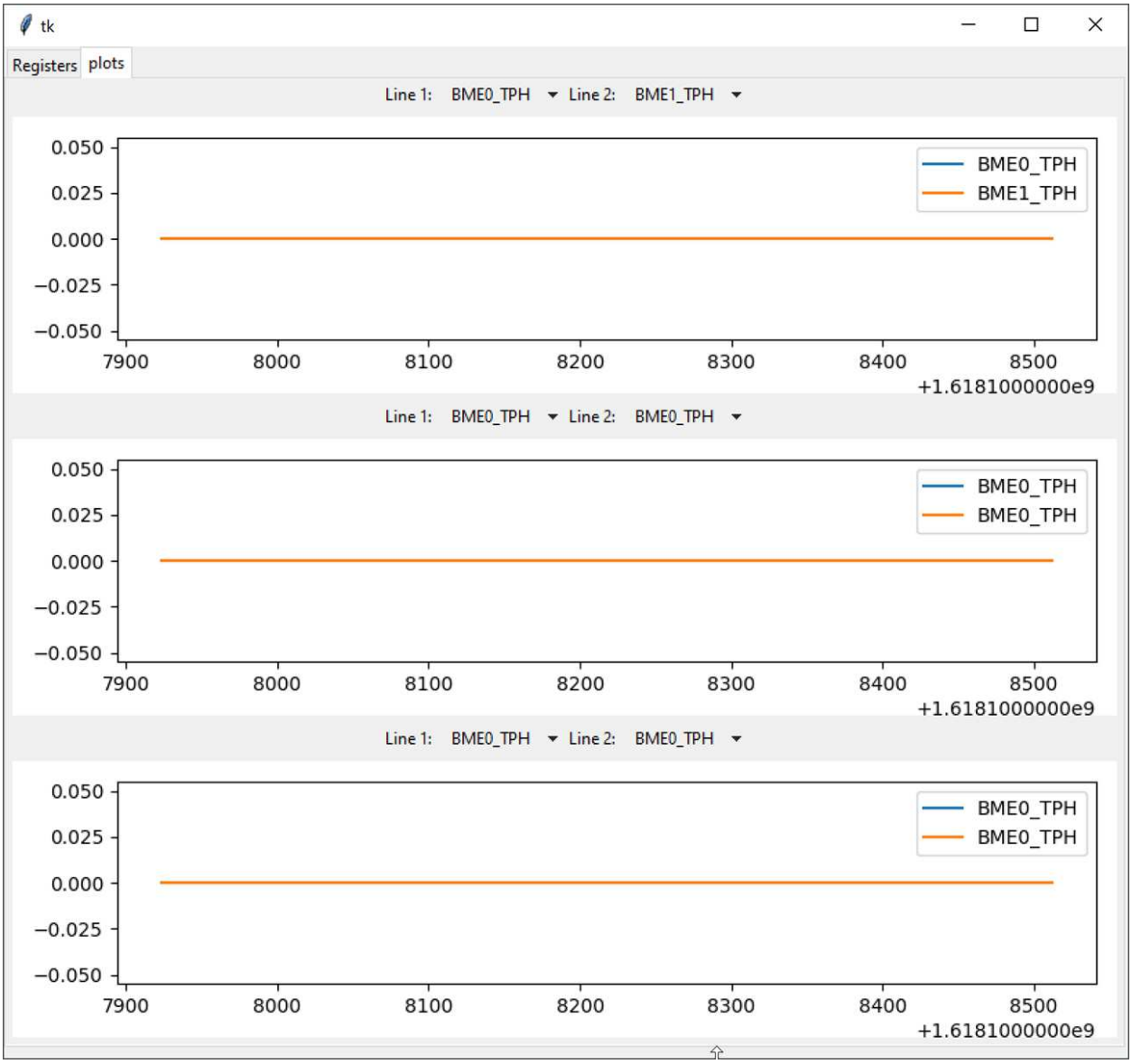

Figure 3.50: The system Status and Control program displaying default state of the plots tab.

Finally, the thermometer standard did not have a data output, so a program was written to read the screen and synchronize thermometer measurements with those of the thermocouple and BME280. This program, shown in Figure 3.51, uses a computer vision algorithm to isolate and identify digits in the thermometer by comparing segment locations to a mapping for seven segment digits. The temperatures from all three sources can be logged to a file, this was used for calibrating the BME280 as well as demonstrating the inadequacy of a thermocouple for precise temperature control.

Figure 3.51: Thermometer screen reader used to synchronize measurements from three sources for calibration.

Chapter 4

Results and Discussions

Aside from the user interface, the SBX1's functions can be categorized between environmental control and the microscope. Environmental control pertains to temperature, humidity, and gas concentration regulation within the chamber. The microscope includes the movement capabilties of the stage itself, magnification and resolution of the optical train, illumination and filtering, and automation features.

4.1 Environmental Control

The first prototype of the SBX1 is complete. A summary of tested control capabilities are shown in Table 4.1. The details of control capabilities are more complex, with a number of caveats and conditions where these specifications apply.

Table 4.1: A summary of environmental control capabilities for the SBX1

Variable	Control Range	tolerance
Temperature	ambient to ambient + 25 °C	± 0.12 °C
Humidity(passive)	50-90% relative humidity	N/A
Humidity(active)	50-90% relative humidity	± 5%
Oxygen	5%-ambient	± 2%

4.1.1 Temperature Control

Temperature control is precise and resilient. Once in steady state, temperature can be maintained to within ± 0.03 °C of the target value as measured by the BME280 temperature sensor, illustrated by the steady state temperature shown in Figure 48.

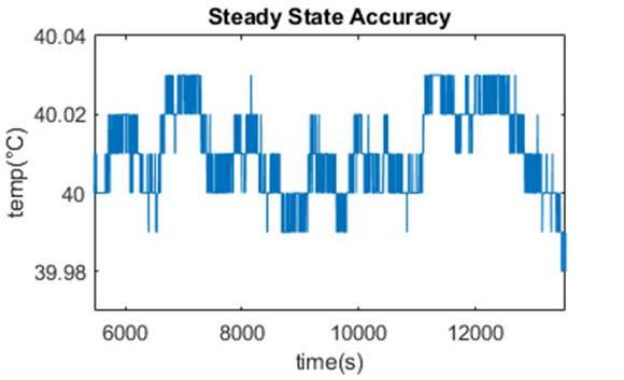

Figure 4.1: Steady state temperature of the SBX1 environment as measured by the internal BME280 over 3.5 hours shows precision of ± 0.03 °C.

As previously determined, when calibrated the BME280 sensor is accurate to ± 0.09 °C, giving overall temperature control an accuracy of ± 0.12°. The box behaves differently during initial heating (Figure 4.2a) and during a small step near the control point (Figure 4.2b). During initial heating, there is an overshoot of 3.93 °C (24.21%), while with the smaller step there is only an overshoot of 0.13 °C (4.33%).

Once in steady state, the control response is very nearly critically damped, with only a minor overshoot. This can be seen in Figure 4.2.The two curves also have a clearly different profile. This large overshoot and different shaped step response are caused by the output railing at 12V. During this time, the integrator continues accumulating error, which must then be removed as the chamber cools to the target. This is important because it means that while the box has a long warm-up period, it can be adjusted by relatively small increments in a shorter time; only 13:57 to reach 0.1 °C of the setpoint as opposed to 2:04:37 for system initialization.

When subjected to a significant disturbance, such as the incubator drawer or microscope door opening, the controller can compensate to a significant degree. Figure 4.3 shows the system response to the door being opened for 5 minutes.

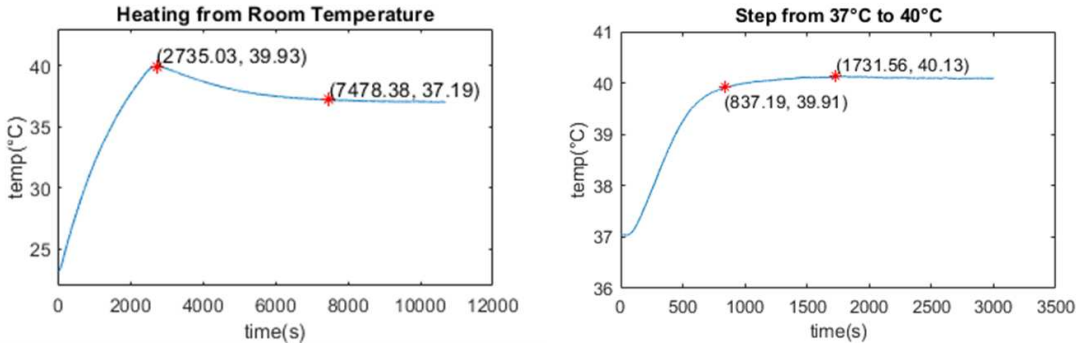

(a) Initialization **(b)** After Initialization

Figure 4.2: The control output is only linear between 2 and 12V. This causes integrator windup and overshoot during initialization (a), but once intialized adjustments can be made with minimal overshoot (b).

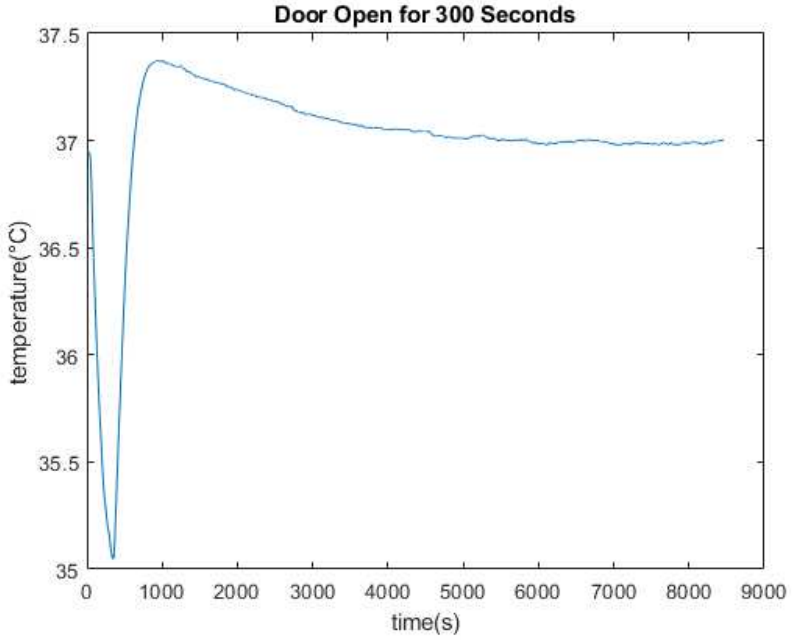

Figure 4.3: The system response to the door being opened for 300 seconds. Other durations are similar, but with an overshoot proportional to the duration of the door being opened.

The timing of the response will be similar for longer disturbances; however, two factors limit the recovery of the system. First, if the door is left open long enough, integrator windup will cause a significant overshoot, proportional to the duration of the open door. The overshoot in with relation to the duration of disturbance is shown in Figure 4.4.

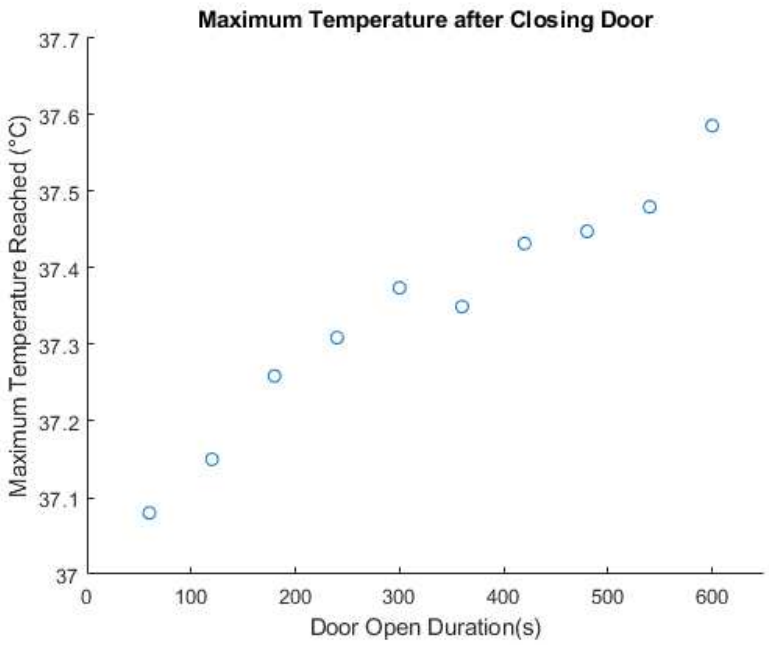

Figure 4.4: Maximum overshoot in the chamber after the door was opened for a fixed duration, then closed. This overshoot is caused by integrator windup as the controller attempts to compensate for the plant change.

There is some advantage to leaving the controller running while the door is open. The heater will attempt to maintain the target temperature, and will at least keep the box from cooling completely. It is able to maintain approximately 35 °C at the sensor with the door open, as seen in Figure 4.5, which shows the minimum temperature reached with the door open. The actual minimum will depend on ambient temperature, but approximately 34-35 °C is feasible. A more powerful heater would allow higher temperatures to be maintained with the door open. Future designs should account for this, to ensure temperature can be maintained with the door open, to minimize the disturbance to the system while the microscope or sample are being adjusted.

In addition to the large overshoot, integrator windup requires a long wind*down* as well, which causes a delay before returning to steady state proportional to the duration of the door being left open. Figure 4.6 Shows the time to return to 0.5 °C, 0.2 °C, and 0.1 °C tolerance in response to disturbances of up to 15 minutes. More minor disturbances, such as a shift in ambient temperature, can be compensated by the controller and will not noticeably impact the temperature within the chamber. One possible solution to the overshoot and long settling time

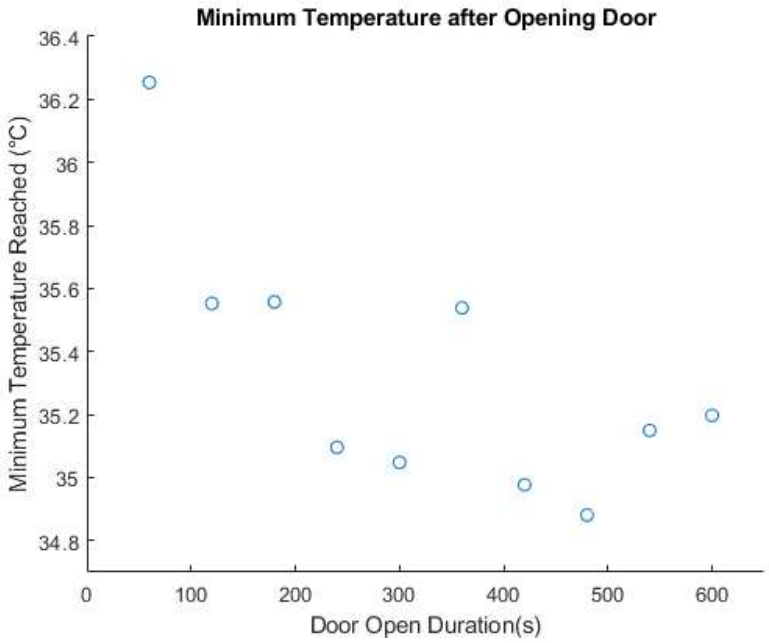

Figure 4.5: The minimum temperature reached with the door open for a fixed duration.

is to detect the drawer or door opening and recording the PID values at that time. When the door is detected as being closed again, the system can restore the controller to those conditions. There will still be some recovery time as residual heat from the heat sinks dissipate and the system returns to steady state, but it should alleviate the massive overshoot and eliminate the integrator windup from the prolonged disturbance. Data is missing for Figure 4.6c for datapoints 60s, 120s, and 180s, they were not allowed to run long enough to recover to that level. Regardless, it is reasonble to claim that if the duration of the door being left open is less than 10 minutes, the system will recover to ± 0.5 °C, ± 0.2 °C, ± 0.1 °C in less than 1200, 2500, and 4000 seconds respectively.

Aside from the door issue, the system has another flaw in the long response time, particularly during initialization.Taking hours to reach steady state on startup is undesirable, but this can be worked around by ensuring the box has been brought to a stable environment prior to a planned experiment. In addition, there is significant overshoot in the system, particularly when initializing the environment from room temperature. It may be possible to improve the

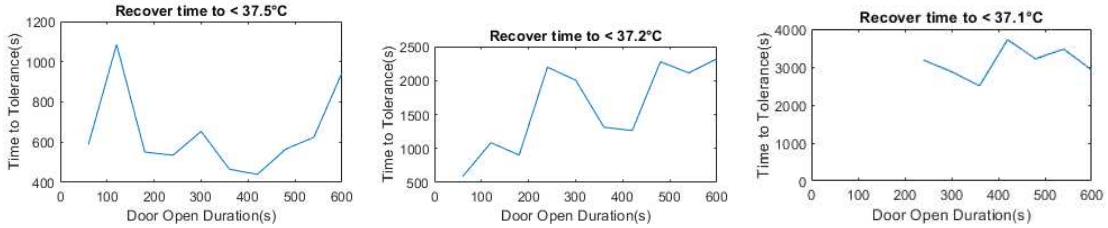

(a) $T < 0.5$ **(b)** $T < 0.2$ **(c)** $T < 0.1$

Figure 4.6: Integrator windup after the door is open will cause the system to take time proportional to the duration of the door being open to recover. Data was missing for the shorter duration trials.

response of the system; however the current tuning is very near critically damped and improving the response manually is difficult due to the slow response of the system.

There are two solutions for the slow response. First, increasing the power of the heater will allow a faster temperature increase. Ideally, the available output power of the heater should be enough that the heater input never rails, introducing a nonlinearity at the output and causing integrator windup. The steady state power consumption of the system would not change, but the step response will be faster. The other solution is to lower the power required to heat the box. Improving insulation in the chamber and reducing the volume will both reduce the heat required to reach steady state, allowing a faster response.

Another issue is transitions between manual and PID control for the output. Consider two scenarios. First, PID control is briefly interrupted and resumed when the internal temperature has fallen by a small amount. Second, when PID control is disabled and the system is allowed to cool significantly, approaching room temperature. The simple solutions to each of these scenarios are contradictory. For the first scenario, simply retaining the previous state of the controller allows the controller to resume as though a minor disturbance occurred. Unfortunately, if the system has cooled substantially, then re-enabling the system will result in significant overshoot caused by integrator windup from the initial conditions. On the other hand, the PID values might be reset whenever control is disabled. In the case that the system has cooled to room temperature, these are the expected initial conditions for the controller and control resumes as normal. But if the system resets to 0 for a short interruption of control, then a large

sag will be incurred, requiring the integrator to build back up to normal operating levels, which may take as long as restoring the system from room temperature.

The current solution is to artificially change the target value on a reset. When the enable flag transitions to false, the controller sets its target temperature to 15 °C, a value which can reasonably be expected to be below room temperature. PID values will then track to this lower temperature, eventually reducing the integrator value to 0. This will allow the integrator to remain relatively high after a brief interrupt to the enable state, reducing the sag after a brief recovery, while preventing overshoot from longer delays. The trend is still to sag after longer delays, but it will not be as severe as directly setting the integrator to 0 on reset.

A better solution is to implement a bumpless transfer, handing off control from the PID controller to a standby controller which keeps PID values updated appropriately based on current system state, which can then be used as new initial values should control be re-enabled. This is one planned improvement for the next version of the prototype.

4.1.2 Gas Control

Gas control tests successfully brought O_2 concentration below 5% and maintained that level to within 0.5%. Future versions should have a better gas seal to prevent leaking, to reduce the amount of displacement gas necessary to maintain this hypoxic environment. Additionally, they system cannot reliably maintain CO_2 levels at 5%. The system has no CO_2 sensor; the intent for CO_2 control was to monitor oxygen concentration when CO_2 is used as a displacement gas, however this proved untenable. The current system is incapable of this task. An attempt was made to do so by approximating the oxygen concentration required, based on atmospheric concentrations of 20.9% O_2 and 0.03% CO_2. The atmospheric concentration of CO_2 is two orders of magnitude lower than the target of 5% and within tolerance for control, so it can be ignored in the calculation. In order to displace 5% of the gas in the environment with oxygen, 5% of the oxygen must be displaced, i.e. oxygen must be lowered to $0.95 \times 20.9 = 19.86\%$. This level of control for O_2, with a tolerance of ± 0.5%, would lead to a CO_2 concentration of 2.6% -

7.3%. This in and of itself is a broad range, though better than nothing. Unfortunately, in practice even this proved an impossible objective. When the system is in steady state, maintaining humidity and temperature, internal oxygen concentration was reported as 19.8%. Since this is not the expected atmospheric concentration of 20.9%, it calls into question the accuracy of the oxygen sensor. The sensor datasheet says it will function from 0-99% RH, (noncondensing) and from -30 to 60 degrees Celsius. The sensor should be functional under the conditions within the chamber, so this discrepancy is unexpected, and more investigation is required to determine the source of this error and if it can be calibrated out. In the long term, an additional sensor for directly measuring CO_2 should be added to the system for more accurate gas mixing.

4.1.3 Humidity Control

The system has proven capable of maintaining greater than 90% humidity for 24-48 hours between well refills using passive or active humidification. With active humidification, control is accurate to within ± 5%. While the humidification control is sufficient for long term incubation (with periodic well refills), it requires further work for future versions. Despite the insulated walls, high humidity caused condensation on chamber walls and the dome, which led to corrosion on various hardware within the box, at one point even corroding a fan connection and causing the heater to melt adjacent walls. This was the motivation for the fan current monitor circuit.

Humidification could be restricted to a sealed chamber on the stage; however, this is essentially the same solution provided by other commercial incubators, leaving little to set the SBX1 apart. Instead, solutions which still increase internal humidity but prevent or redirect condensation are required. Condensation occurs when a surface has a lower temperature than the dew point of the gas in the chamber. One solution is to ensure that condensation will run down of the walls and into reservoirs near the base, rather than dripping onto electronics or the microscope. Another solution is to create an actual vacuum between walls, which may allow the wall temperature to be maintained closer to the air temperature in the box. This is impractical, par-

ticularly for a low-cost device. Another solution is to place heaters within the walls themselves. This may be feasible using silicone heaters. A combination of the two solutions may also help, with channels to collect condensation on lower walls, with heaters between the dome walls to prevent condensation from dripping onto the stage or electronics.

4.2 Microscope

The microscope's capabilities can be classified as mechanical, optical, and software. Mechanical capabilities center around the motorization of the stage and focus. Optical capabilities include the magnification, resolution, illumination, and filtering capabilities of the microscope itself. Software capabilities have to do with recording and automation functions.

4.2.1 Gantry and Movement

The gantry has a theoretical step resolution of $1.562\,5\,\frac{\mu m}{\mu step}$ for X and Y axes and $0.232\,\frac{\mu m}{\mu step}$ for the Z axis. Machining tolerances and fabrication errors mean this will not be exact. These errors may also lead to an angular error between the X and Y axes.

The exact distance traveled is not important; only that the microscope can focus on a 5 µm object and that it can return to a prescribed (X, Y, Z) position and height during automation. Focusing can be accomplished, but it is finicky, particularly at higher magnificiation. As discussed in the optics section,.there is significant backlash in the Z axis. First, the inherent backlash of the linear guide is amplified by the 1:27 ratio of the gearbox. Second, the gearbox itself introduces $\leq 1°$ backlash of its own. Combined this results in backlash of approximately 2000 steps. The autofocus algorithm compensates for this, but manually focusing can be quite challenging, as going past the point of focus requires reversing direction and attempting to manually remove backlash. Overshooting requires repeating the process. Because of the backlash problem, focus is best achieved by approaching carefully from one direction to avoid overshoot. However this can be problematic when trying to find a single small subject, where frequent manual focus "scanning" is useful. Introducing an anti-backlash nut to the linear guide would help with the

backlash in the linear guide; however, that will not resolve backlash in the gearbox, which is inherent in the reduction gears.

In a future version, one solution would be to use a different method of reduction which can be backlash compensated, such as a timing belt with reduction gears and a lead screw with a smaller lead. High precision linear encoders are available, but they are expensive. A rotary encoder could also be added to the output axis for backlash compensation; however, a high precision rotary would be costly, and at that point it would likely be better to simply use a servo motor. For example, the relatively low-cost ($271) CPM-SDSK-2310D-RLS from Teknic has a resolution of 0.057°, with 0.03° repeatability [93]. By comparison, the stepper motor currently in the system with a 26.85:1 reduction and a 1.8°, giving a 0.067° output with significant backlash. The downside to a servo motor solution, apart from higher cost, is a larger size and more complicated control.

4.2.2 Optical Limits

Direct magnification in the microscope is the same as that of the objective lens. The digital magnification of the microscope is dependent on the pixel size of the monitor being used. More meaningful metrics are the diffraction limit and spatial resolution associated with each lens. These characteristics are shown in Table 4.2: Calculated field of view for each objective.

Table 4.2: The calculated field of view and Rayleigh Resolution at 500nm for each objective.

Objective	**Spatial Resolution**	**Field of View**	**Rayleigh Resolution at 550** nm
4x/0.10	1.12µm	918 µm x 690µm	3.69µm
10x/0.25	0.448µm	367 µm x 276 µm	1.47 µm
20x/0.40	0.224µm	184 µm x 138 µm	0.921 µm

Spatial resolution is simply determined by the sensor itself. Each pixel of the image is mapped to a segment of the object, proportional to the magnification of the objective. Regardless of the quality of optics, resolution of the system can never be better than this value, because the pixel density of the sensor is not sufficient. The Raspberry Pi Camera V2.0. is used in the SBX1. This camera has a Sony IMX219 sensor, which has a 3280x2464 resolution, or 1640x1232 with binning [94]. Binning sums neighboring pixels to create one superpixel, which allows a lower signal to noise ratio (SNR) and better exposure. Because low intensity light is likely when using fluorescence microscopy, the maximum binned resolution of 1640x1232 is used for this calculation, which has superpixels (a 2x2 group of individual pixels) of 2.4 µm x 2.4 µm. Capturing detail in the image is dependent on the Nyquist criterion, which requires a sampling frequency twice that of the highest spatial frequency in the object under observation [95]. This means that the spatial resolution in both X and Y is $r_{x,y} = \frac{2*d_{x,y}}{M}$ where M is the magnification of the objective and $d_{x,y}$ is the dimensions of a single pixel in the sensor. These calculations for each objective lens in the system are listed under Spatial Resolution in Table 10: Calculated field of view for each objective.. Note that for each objective, the resolution is still smaller than the Rayleigh resolution, which means that the optical train rather than the sensor is the limiting factor for minimum resolvable feature.

Rayleigh Resolution is a measure of the diffraction limit optical train, which determines the minimum resolvable feature of the object which will not blend in the image. The Rayleigh Resolution limits the proximity of two features to approximately the width of one Airy disc [96], ensuring that each point will be distinguishable in the image. This can be calculated using the numerical aperture (NA) of the system and the wavelength of light used to generate an Airy disc. The NA is listed next to the lens magnification in Table 4.2. The Rayleigh Resolution for a specific wavelength is $\frac{0.61\lambda}{NA}$. Rayleigh Resolution near the center of the visible spectrum at 550nm is listed in Table 10: Calculated field of view for each objective. These values provide a theoretical minimum resolvable feature for a given wavelength. An empirical measurement to demonstrate the optical capabilities of the microscope using a resolution test target.

4.2.3 Color Accuracy

The camera has shown to be suitable where color accuracy is not important. 4.7 shows magnification at 4x, 10x, and 20x of a test target with 10 µm minor divisions and a 100 µm spaced grid in the center. While the magnification appears to agree with the theoretical resolution limits previously determined, there is significant chromatic aberration, particularly in the Y direction. There is also significant discoloration and vignetting visible in what should be a white background.

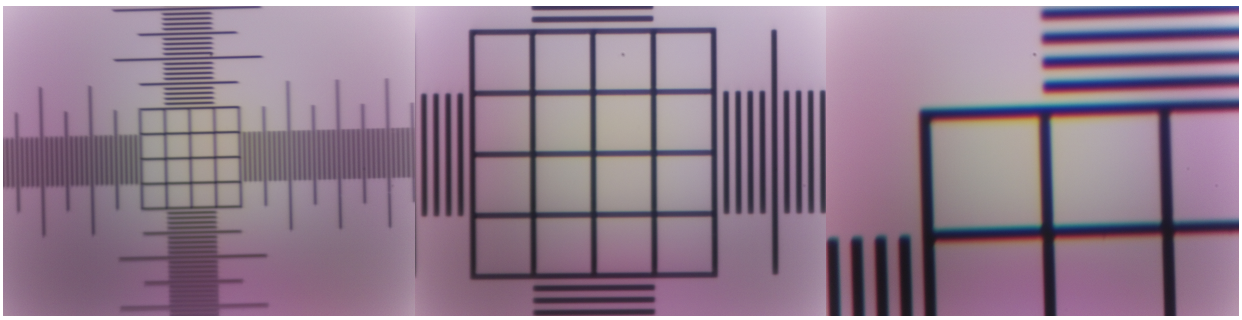

(a) 4x **(b)** 10x **(c)** 20x

Figure 4.7: Images of a micrometer test slide. Minor divisions are 10 µm, major divisions are 100 µm. Chromatic aberration may be due to the lack of a coverslip or misalignment in the microscope's mirror.

The primary source of the discoloration and color crosstalk is firmware lens correction in the Pi Camera V2. Normally, camera firmware corrects for lens distortions and vignetting from the lens housing that are normally installed on [97]. By removing that lens, the correction introduces color error in the camera output. To illustrate that this is the issue, Figure 4.8 shows an image captured in [97] to demonstrate the issue, which veery closely resembles the distortion seen in Figure 4.7.

Another factor in chromatic distortion is the sensor's sensitivity to light outside the visible spectrum. The spectral sensitivity of the sensor is shown in Figure 4.9. Observe that blue pixels apparently have significant sensitivity below 400nm, enough to be sensitive to UV-A light sources. Observe also that the red pixels appear to have sensitivity well past the visible spectrum into the infrared. This sensitivity is often compensated by applying filters or lens coatings

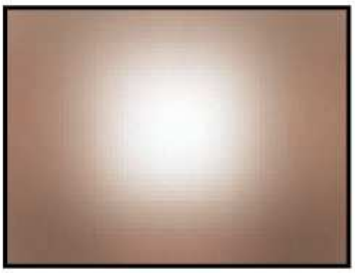

Figure 4.8: Direct white illumination vignetting and color distortion caused by firmware color correction in the Pi Camera V2. Adapted from [97].

to block UV and near infrared light. The lens on the Raspberry Pi camera has been removed, directly exposing the sensor. This means that the lens will interpret UV light as blue and infrared light as red, which may add a cast to images.

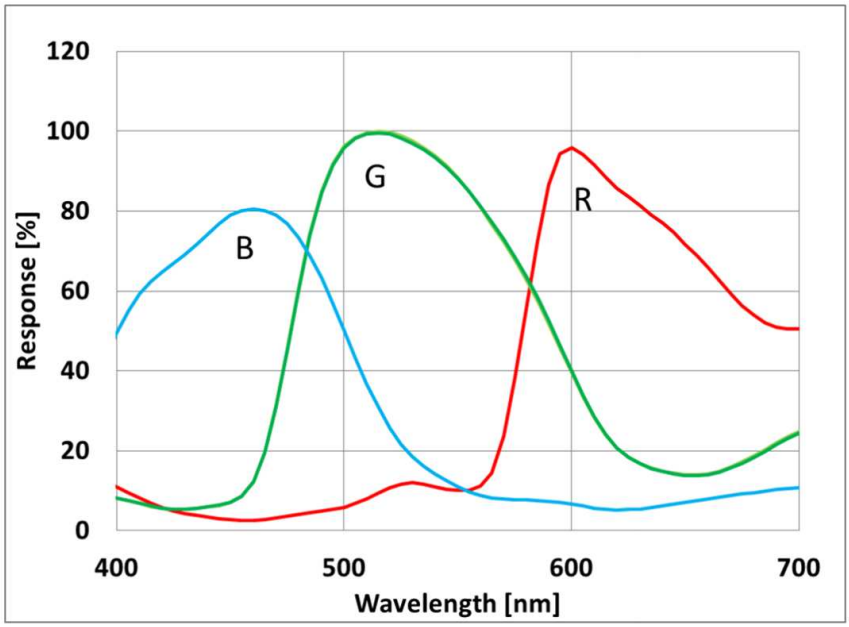

Figure 4.9: Spectral sensitivity of IMX219. Note the trend at red wavelengths is not declining. Adapted from [95].

This is not an issue for the SBX1 because the LED sources do not produce light in these wavelengths, as can be seen in Figure 4.10. On the other hand, if there is fluorescence in the infrared band or excitation in the UV band, the sensor will still detect them as red or blue re-

spectively. This is actually be beneficial in the case of fluorescence which passes above 700 nm as it will be more intense to the camera than to the naked eye.

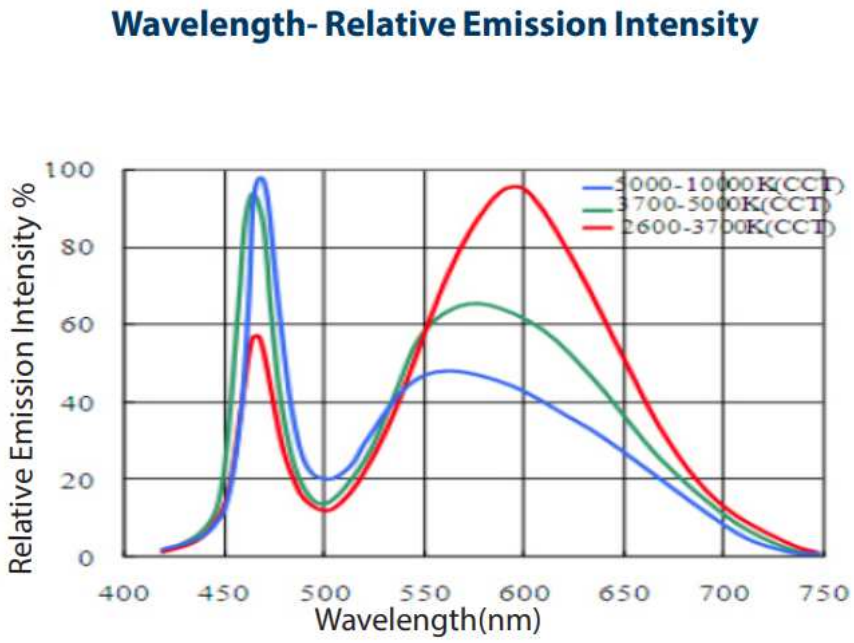

Figure 4.10: Spectral power density for MP-2016-1100 series white LEDs. Observe that output is fully in the visible spectrum between 400 and 700nm. Adapted from [79].

The firmware lens shading table can be corrected as described in [97]; this will be performed for a future version of the microscope. A simpler strategy is to image a gray target and add the difference from the average value to a correction map, which can be used to update each pixel value in captured images for color correction. IR/UV filters may be used in the filter wheel. This would only work for white light, but this is probably OK because the other filters would only be used for fluorescence microscopy which would not be subject to chromatic distortion anyway, since the light source would not have energy in the problematic bands anyway.

4.2.4 Illumination, Fluorescence, and Filtering

The LED ring provides multiple illumination options. The white LED has a broad spectrum of illumination with a 90% CRI. It is useful for traditional white light illumination. Single color

LEDs in the ML-E series emit as shown in Figure 4.11. These LEDs provide emission peaks at 365, 465, 480, 535, 595, and 630 nm. These colors have significant overlap with the excitation bands of a variety of common fluorophores, including DAPI, Alexa Fluor 488, Alexa Fluor 647, Cy3, and many others. LED Illumination excites the fluorophores in a sample, which fluoresces with an emission wavelength dependent on the fluorophore. To show only emission and not excitation band light, an appropriate longpass filter must be placed in the optical path with a cut-on frequency between the LED's output band and the fluorophore's emission band. Available longpass filters for the lab are from 400 to 700 nm in 50 nm increments. An initial test to prove the concept was performed using FocalCheck Test Slide #1 from Invitrogen. The beads have a nominal 15 µm diameter and FocalCheck green, orange, and far thin rings [98].

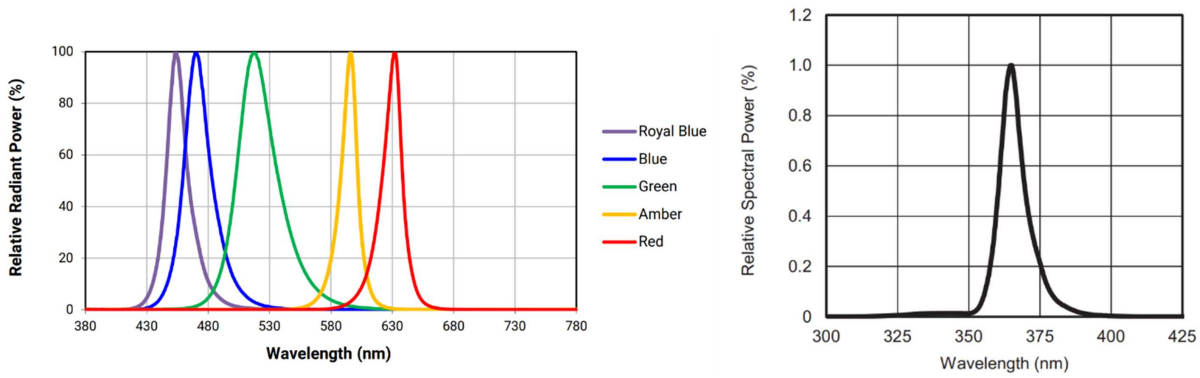

(a) MLE Series, adapted from [84]

(b) VLMU1610-365-135, Adapted from [82]

Figure 4.11: Spectral power density for MLE series (a) and VLMU1610-365-135 (b) LEDs. Each has a full width half maximum of approximately 25nm, wtih the exception of green which is closer to 50nm.

The expected spectral plot for this setup is shown in Figure 4.12, with the exception that the blue laser at 480nm is representative of the blue LED, which actually has the shape shown in Figure 4.11a, with a Full Width Half Maximum (FWHM) of approximately 25 nm. Excitation curves are dashed, while emission curves are solid with a fill. The blue LED only partially overlaps the excitation band of the green stain and just the tail of the orange stain. Moreover, the emission filter (ET525LP) has a sharp cut-on at 525nm, above the emission peak for the green stain.

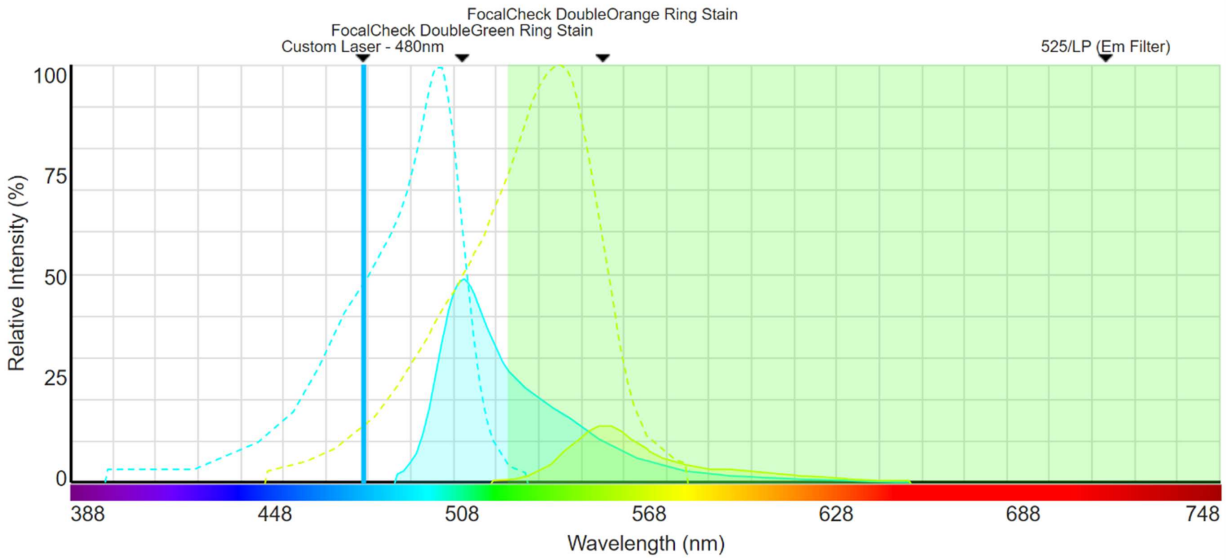

Figure 4.12: The setup for illuminating FocalCheck #1 test slide illustrates excitation and emission bands of the microbeads as well as a blue laser line at the peak wavelength of the MLE Blue LEDs. An ET515lp 525 nm longpass filter was used to isolate the emission band for the camera.

The image captured with this setup is shown in Figure 4.13. The beads can be clearly seen in the left image, illuminated with white LEDs. The right image shows the fluorescing LEDs through the emission filter. The dimness of the beads is due to the combination of inadequate overlap of the illumination band with the excitation band, and the longpass filter cutting off a significant portion the green fluorophore's emission band.

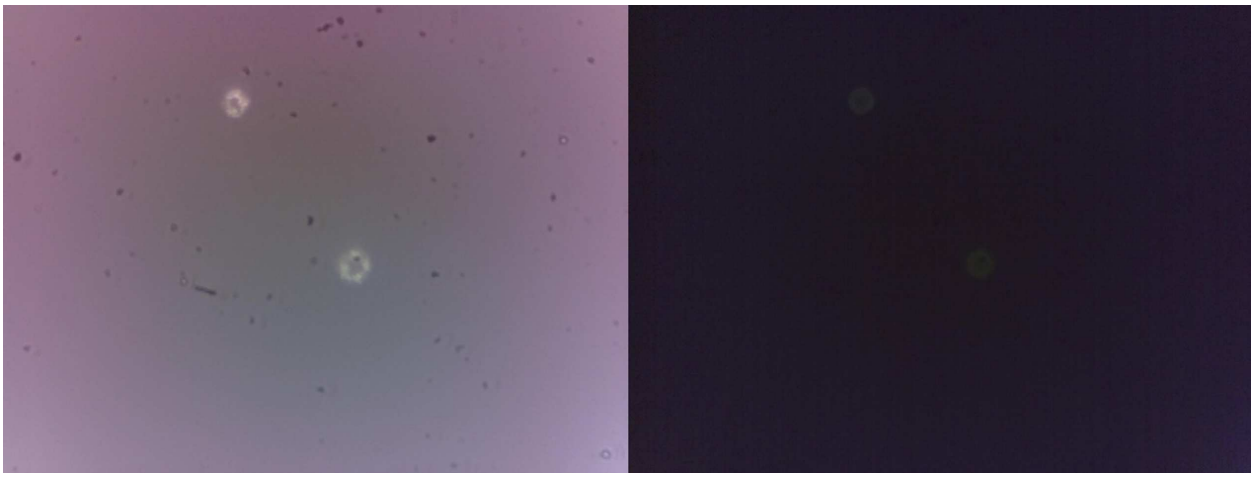

Figure 4.13: The FocalCheck #1 slide with brightfield (left) and fluorescence (right).

CSU's Stasevich lab graciously provided us with an additional set of prepared slides as well as a "TetraSpeckTM Fluorescent Microspheres Size Kit", with beads from 1-4um. Z axis backlash has proved to be an issue for not only focusing on subjects, but for finding them in the first place. The microbeads proved too difficult to find with the microscope. The samples presented a different issue. Table 4.3 shows the dyes used in the provided samples and the "best fit". The only filters available for this test were the FEL500 and FEL550. The FEL550 has a cutoff too high to pass the emission spectrum of Whereas the FEL500 significantly overlaps the tail of the blue LED's bandwidth, which is still at approximately 20-30% of peak power at 500nm. This causes a green light to bleed through the longpass filter. Given the intensity of the blue light, this could easily wash out the dim emission of the samples.

This highlights the largest issue with the fluorescence illumination and filtering configuration with the SBX1. The LEDs have long tails in their emission spectra. While these tails are low power relative to the source, they are still intense relative to the fluorescence of the sample. Thus, the emission filter must cut on at a much longer wavelength than the excitation band's peak to prevent low intensity background illumination in the image.

This restricts viable fluorophores to those which have a large separation between excitation and emission peaks. While there are fluorophores where this is the case, this greatly restricts fluorescence capabilities of the microscope, and even with fluorophores which can be successfully illuminated, much of the emission band may still need to be cut off to minimize the intensity of excitation light passed through the filter.

In addition to difficulties with isolating the light source from the fluorescence, there are also concerns with photobleaching caused by prolonged illumination over the entire sample. When fluorophores are in an excited state, they may interact with other molecules to permanently disable excitation of the particle. This phenomenon is known as photobleaching [99]. When subjected to continuous illumination, this effect occurs in nearly all fluorophores [100]. While there are methods to slow the process such as limiting exposure to oxygen quenching the more reactive triplet state, it cannot be completely prevented [99] [14] This is of particular import

for the SBX1's lighting system because rather than using a directed light source, it uses a light ring, exposing an entire sample to the excitation band of the fluorophore, so even portions of the sample not under observation will be subject to photobleaching. For this reason, only methods which limit exposure time, take preventative steps to mitigate photobleaching, utilize photobleaching as a metric, or use more photostable dyes such as the Alexa Fluor series [100] are considered viable for the SBX1's imaging system.

These problems and concerns must be addressed in the next version of the SBX1 prototype. The major issues to address are the bleed from LEDs through the emission filters, and photobleaching of fluorophores caused by prolonged exposure of the entire sample to the excitation band. Preventing light bleed can be accomplished with the addition of a shortpass excitation filter between the light source and the sample, with a cut-off wavelength slightly below the cut-on wavelength of the emission filter. This way it is guaranteed that the light entering the sensor is only from the fluorescing sample.

This can be accomplished by moving the light source to the opposite side of the sample, for transmitted rather than reflected illumination, and placing the filter between the sample and the light. Another method of creating coaxial illumination would be to use a collimator to parallelize the LED sources. This source can then be injected into an infinity corrected optical path. By using a half mirror (dichroic mirror) the excitation band can be directed onto the sample through the objective, while the emission band passes through the mirror and to the sensor. This is the configuration used in epifluorescence microscopes, illustrated in Figure 4.14. Both solutions will also help with the photobleaching issue by only exposing the region of the sample in the field of view, and they will increase the intensity of excitation and emission by focusing the source's power into a smaller region. The epifluorescence setup has the added advantage of minimizing emission spectrum bleed-through due to the dichroic mirror prior to the emission filter.

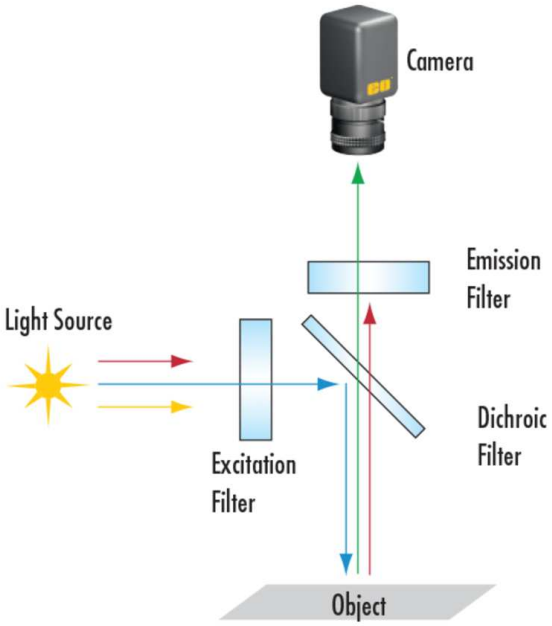

Figure 4.14: Example of the proposed epifluorescence configuration which could replace the current optical system. Rather than ring illumination as in the current system, the source light passes through an emission filter and is reflected onto the subject via a dichroic mirror. The emitted light passes through the dichroic mirror and is further filtered through an excitation filter. This setup ensures that only fluorescence from the subject is detected by the sensor. Adapted from [101]

.

Table 4.3: Fluorescence Capabilities during trial with stained samples.

Fluorophore	**Excitation peak**(nm)	**Emission peak**(nm)	**LED peak wavelength** (nm)	**Longpass Cutoff** (nm)
DAPI	358	461	356	400
Alexa Fluor 488	499	520	475	500
GFP	488	508	475	500
Alexa Fluor 594	590	620	590	600
Alexa Fluor 568	578	603	590	600
Alexa Fluor 647	650	670	No Option	650

4.2.5 Video and Time-lapse

Video and still images can be captured by clicking their respective buttons on the user interface. The record button will begin a recording in the location specified in settings, likewise with the snapshot function. The record function will also adjust recording and capture framerates

to capture fast or slow motion (e.g., time lapse video). This is restricted by the maximum capture rate of the video. If specified, the record button may record a series of snapshots, a video file, or both. In addition to the quick access recording functions, Ryan's time-laps automation successfully scans and captures images at a specified interval. For a well plate, the user can specify which wells should be captured. The spacing of wells is built into the program based on standard well plate dimensions. The program develops an estimated time for a single cycle of images and will prevent time-lapse from starting until the user adjusts the image interval to greater than this time. They may then specify the duration of capture, experiment name, and save location. When the "Run Time Lapse" button is pressed, the automated task begins. When the specified interval has elapsed, each indicated well will be imaged and saved in the specified save location. The automation routine will begin assuming the objective is centered over the A1 well, or the desired location on a slide.

Future versions of the time-lapse capability will include user-specified arbitrary locations, and grid scans for slides, petri dishes, and larger wells such as 4, 6, or 12 well plates. It may also include focus position or an autofocus enable option for each position to allow depth tracking over time. In its current capacity, a fixed focus is used, so if the focal points of wells differ, those wells will not be in focus. Because of this, time-lapse is most useful for a single position capture or for samples which are fixed on a uniform plane.

4.2.6 Autofocus

The autofocus algorithm works well for prepared slides with the sample fixed to a surface. Samples in suspension were not available to test an example which would have multiple local maxima. The focus score calculation for a prepared slide of a human blood smear can be seen in Figure 4.15.

Representative images from several points and the final focused image can be seen in Figure 4.16. The final image is focused on the blood smear, demonstrating a functional algorithm.

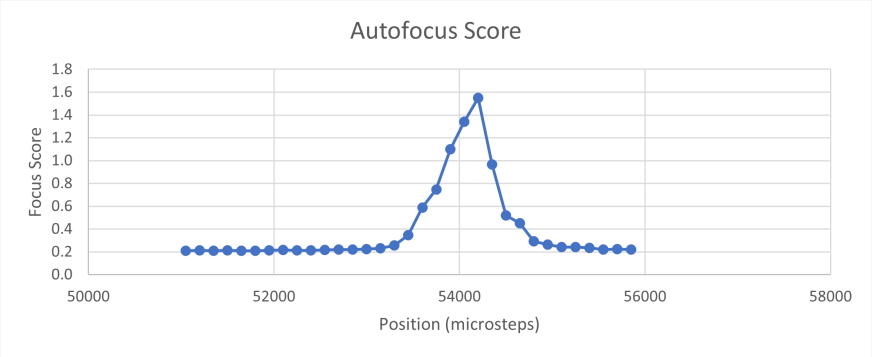

Figure 4.15: A plot of focus scores for a human blood smear sample slide. The maximum of the interpolation of the focus scores is used as the point of optimal focus.

There are some discolorations and distortion, but these are artifacts of the microscope itself rather than the algorithm.

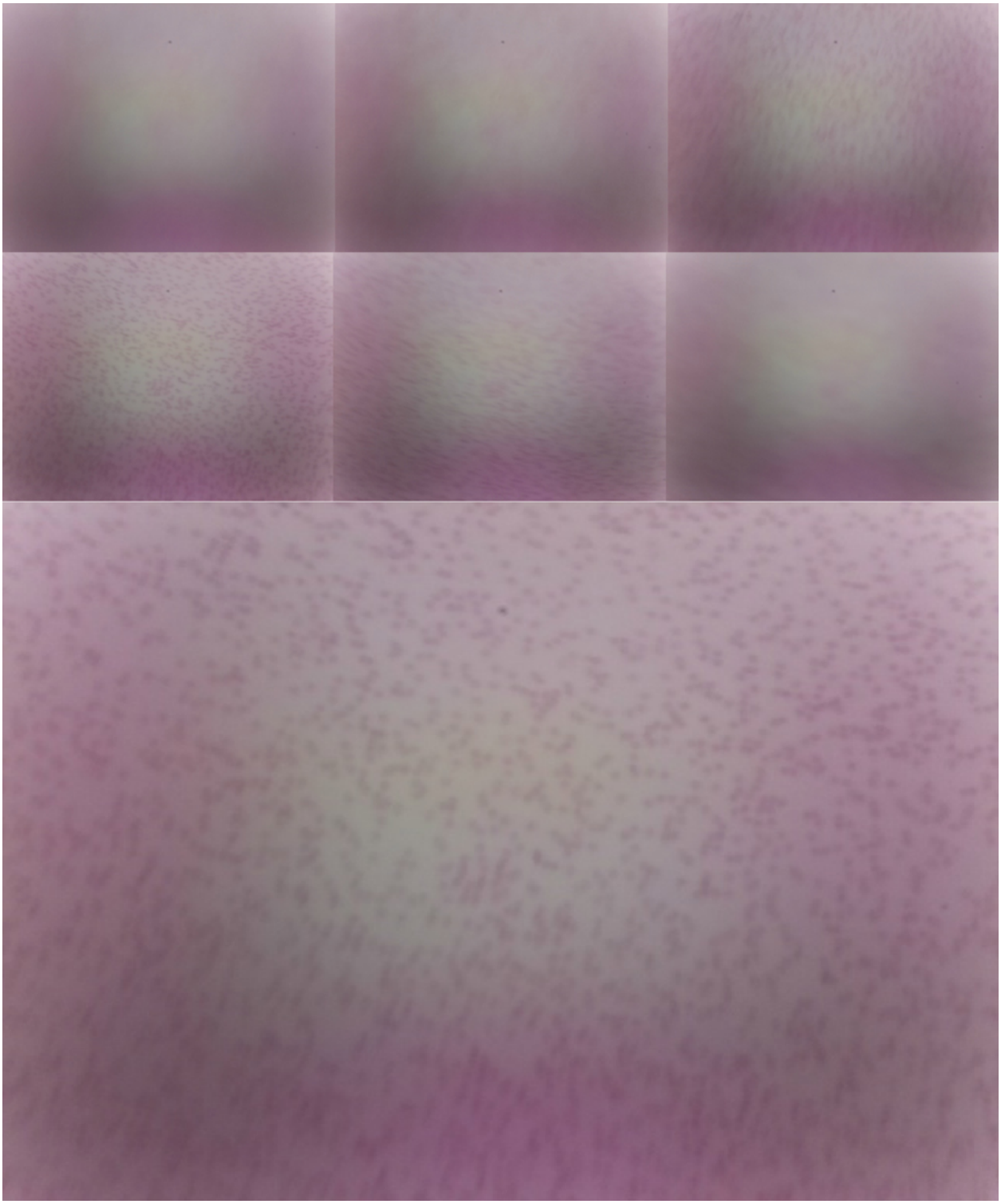

Figure 4.16: A demonstration of autofocus, showing multiple sampled images along the path and the final focused image.

The primary opportunity for improvement in autofocus is processing time: this example took 64.35 seconds, which does not include the initial motor movement. This may be accomplished by increasing parallelization in the autofocus algorithm and possibly by upgrading to a faster computer. This might be another single board computer with GPIO such as an Asus UP-squared, or more likely traditional PC communicating via a USB to SPI/I^2C interface based around an FT232 or similar chip. Improvements to the stage and motor system would help, particularly better backlash compensation, faster motor movement, and stabilization in the Z axis to prevent rocking with direction changes.

The current program only has an autofocus profile for slides. More scanning profiles need to be added for wells and other equipment, such as well plates or petri dishes. Another useful profile would be a "full sweep" starting from the current position of the objective and raising the Z axis to its upper limit. With the current motor this would take a significant time, but a shift to a servo motor drive for the Z axis would allow rapid but precise position changes.

4.2.7 Image Stitching

The stitching algorithm has proven to be effective for "easy" tasks. For example, Figure 4.17 shows a stitched image of a longitudinally sliced basswood stem. This image has clear lines which continue through each tile, and each tile is visually distinct from its neighbors. Linear edge blending helps to further merge the tiles into a single coherent image. The diagonal edges are an artifact of the edge matching algorithm. Because of this, it is important to capture an area larger than the area of interest if possible.

Figure 4.18 illustrates the effectiveness on a sparser image, in this case a human blood smear. There is still the red/blue cast to the image as well as vignetting discussed in the color accuracy section. This cast will appear over different locations in the image as it the stage scans, resulting in the blotches of color seen, particularly apparent in the blood smear which has a uniform background.

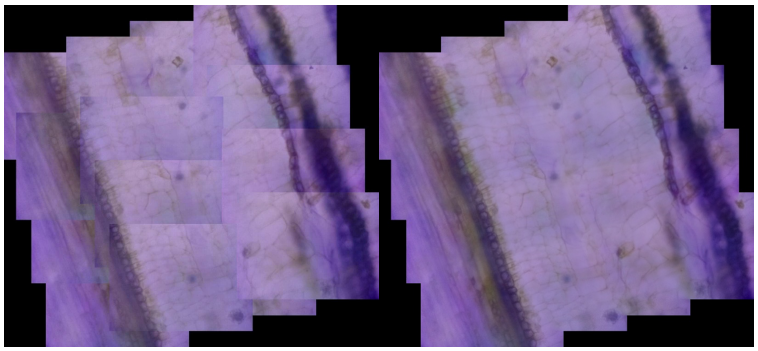

(a) **(b)**

Figure 4.17: Stitching example. The sample was a prepared sample slide containing a longitudinal slice of basswood stem. The left image is a direct overlay of the images at the overlapping positions. The right image includes linear blending.

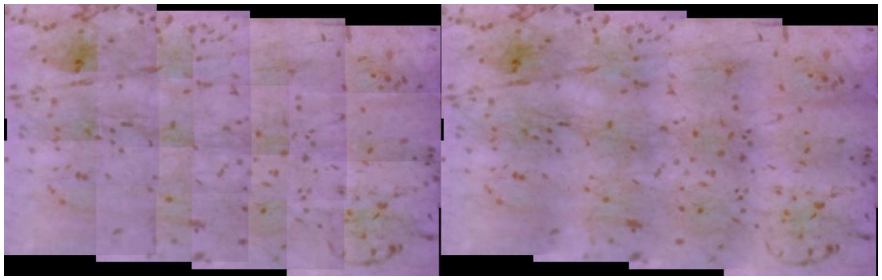

Figure 4.18: Stitching example using a human blood smear. Left image is raw, right image includes linear blending. This demonstrates the stitching program's capability even when there are relatively few landmarks to align.

Chapter 5

Conclusions and Future Work

The SBX1 is a prototype solution to a problem in biomedical industry research and development: quality incubation and imaging systems are extremely expensive. There are a variety of devices, commercial and custom built, which provide live environmental control and live cell microscopy. The primary issue with these devices is in their costs. The simplest devices available are bench-top and portable incubators, starting around $3000. Stage-top incubators which allow observation of samples under a microscope cost as much as $12000, and advanced live-cell imaging systems cost anywhere from $50,000 to $700,000 depending on incubation capability, microscope quality, and software packages available. By contrast, the total cost for an SBX1 prototype is $2134.66 (see Appendix C). The cost of the SBX1 prototype is competitive when compared to commercial offerings, but it must meet environmental control and microscopy needs of most users to be viable. The system shows promise, and each subsystem provides at least some functionality., but the SBX1 is not ready for a commercial trial. Each of the major components of the system have issues which leave significant room for improvement. This includes the user interface, environmental control, and the microscope.

The user interface provides simple, fast access to the box's functions, including motor movement, illumination control, environmental control, and the camera feed, including quick access buttons for snapshots and video recording. It also provides an interface for image stitching and multi-point time-lapse imaging. While functionally sufficient, the GUI is visually unappealing and somewhat unintuitive. This is particularly true for image stitching and time-lapse functions. This can be addressed by changing to a more modern GUI toolkit such as Qt and providing better integrated instructions and user feedback to the interface. Additionally, the Raspberry Pi has proven to be underpowered or inadequate for intended uses. This has resulted in slow autofocus calculations and an inability to perform image stitching with the qual-

ity expected from a windows PC due to a lack of ARM libraries for some of the MIST blending functions.

An appealing solution to issues aesthetics of the user interface, while also providing performance improvements is to remove the Raspberry Pi entirely and use an x86 based PC, connected to the control board via a USB to I^2C protocol adapter chip such as an FT232H or an MCP2221A. This would allow image stitching to be fully integrated with the software and provide additional computing power. It would also accelerate the autofocus function both due to the faster processor and access to CUDA or OPENGL for graphics processor acceleration of matrix operations. It would reduce the cost of the system by requiring the user to supply the PC. One important feature to add is a "click , drag, and zoom" paradigm for microscope control, allowing the user to navigate the stage in the same way one would navigate common map software, by "dragging" the stage with the mouse and using the mouse wheel to adjust focus.

The current prototype is partially successful at maintaining a suitable environment. Temperature control is precise and robust, capable of maintaining up to 25 °C above ambient with an accuracy of ± 0.12 °C at the sensor. Relative humidity can be maintained above 85% with passive or active humidification. Internal gas mixing allows maintaining oxygen concentrations as low as 3 ± 2%. It can also accept premixed gasses.

Environmental control issues include some of the simplest and the most difficult issues to tackle for the next version of the prototype. Temperature control is stable but suffers from a large overshoot and a long time constant during initial heating, taking as long as two hours to reach steady state within tolerance. Additionally, the system is particularly prone to windup caused by significant disturbances or control changes. If there are significant disturbances to the system such as the door being left open for a prolonged time, or the system being stopped and started without fully resetting to ground conditions, temperatures are prone to excessive overshoot. There are also issues with humidification causing condensation, potentially contaminating samples, and corroding hardware. Finally, the chamber is also not sufficiently airtight, leading to a high average flow rate of fill gas required to maintain setpoints. Additionally,

only an O_2 sensor is available currently. This allows the creation of a hypoxic environment, but there is no sensor for CO_2, which is another desirable environmental control.

The long startup time and large startup overshoot of the temperature controller, as well as condensation from the humidifier, can be at least partially addressed with several of the same potential solutions. The issue with condensation is that however efficient the insulation of the system, unless the walls have a vacuum or a low molecular weight gas fill, the surface of the walls will be cooler than the air in the chamber. This means that the walls are likely to be below the dew point for increased temperature and humidity, leading to condensation. One solution is to heat the walls themselves, perhaps with a large silicone heater, to raise them above the dew point. Another option would be a separate channel, presenting a false inner wall to the internals of the system. Condensation may still occur on the outer wall, but that would be acceptable, provided there is adequate collection below the walls to collect condensate. Should a two-hour startup time prove unacceptable, it can be improved by increasing the available output power in the heater so that the output does not rail. This would also reduce the startup overshoot. Additionally, the door and drawer opening must be detected and handled differently to prevent overshoot caused by integrator windup when the door/drawer are closed again.

The simple solution to gas mixing inaccuracies is to inject a premixed gas rather than mixing gas directly in the environment chamber. Even with a premixed gas, concentrations may not be accurate due to poor sealing of the box. This leads to diffusion through the chamber and concentrations different from the premixed canister. Even with the current internal gas mixing the poor seal is an issue due to the high flow rate required to maintain the target concentration. If the chamber is expected to maintain a gas concentration throughout, it will require significantly better seals to mitigate diffusion. The ideal would be to purge the chamber, then fill with a premixed gas. This still leaves an issue with the door or incubator drawer opening, which will cause the internal gas to rapidly equilibrate with atmospheric concentrations.

The SBX1 microscope has a sufficient resolution and diffraction limit for imaging features as small as 0.921 µm and, with a minimum Z step of 0.232 $\frac{\mu m}{\mu step}$, it can focus on those subjects

as well. A combination of the filter wheel and a ring light which can illuminate at single color wavelengths allow for fluorescence microscopy. The stage can move in 1.56 $\frac{\mu m}{\mu step}$ increments, providing fine control for stage positioning. The current stage has protruding mounting screws which make positioning well plates difficult, but it can easily hold 100 mm dishes and slides. A new stage has been designed and can accommodate standard well plates in addition to 100 mm dishes and slides. It also has an adapter plate to ensure equipment is aligned with the stage's movement axes.

Experiments showed fluorescence in a microbead, albeit dimly. The limits of using only an emission filter rather than an emission filter in conjunction with an excitation filter restricts which fluorophores can reliably be detected with the optical system. Additionally, the ring light exposes all samples simultaneously, potentially photobleaching samples that are not even being observed. While it will be more expensive, it is apparent that a more robust system of illumination is required. Additionally, a survey of similar devices and the needs of collaborators has revealed that an upright microscope will be unsuitable for many tasks required of the microscope for this system.

Considering this requirement for an inverted configuration for the microscope, the XY stage and possibly the Z axis will need to be redesigned. At a minimum, the microscope must be redesigned as an inverted microscope. Ideally the microscope could be configured as either upright or inverted. Lighting needs to be changed as well, to accommodate a more common epi-fluorescence setup. This will likely additionally require converting the microscope to an infinity corrected system. The stage design will need to change as well, particularly if the new design is capable of transillumination as well as direct illumination. Because the light source would be opposite the stage from the objective, the stage could not be supported from the center. Due to the complexity of the design and the importance of a well-designed microscope to the system, this will likely require a consultant to assist with the microscope design. Another option would be outsourcing the microscope design to an Original Equipment Manufacturer (OEM). One newcomer to the scene that could be promising is Discover Echo Inc., which man-

ufactures microscopes which can be quickly and easily reconfigured as upright or inverted and have many of the desirable features of other commercial products reviewed such as an automated stage, Z stacking, and autofocus [102].

In addition to the issues which must be resolved in the current prototype, other opportunities have presented themselves for design variations. For example, users may not wish including the microscope and utilize only the incubation capabilities of the box, or they may not want the incubator drawer, with only a requirement for microscopy. There may be needs for a custom microscope, or accommodations for a particular lab's hardware to be enclosed in a low cost, small footprint chamber. A customer might require vibration damping for the microscope such as an integrated air table, or a custom ring light using wavelengths other than those available for the current ring. By incorporating a battery sufficient to power a smaller unit without the microscope, the enclosure can be made into a portable incubator which would be useful for transport of sensitive samples such as semen or oocytes as well as serve as a battery backup in the case of power interruption. Some changes, such as making a smaller incubator only design, or designing a custom light ring, are straightforward and could be accomplished in days or weeks. Others are more challenging, such as a custom enclosure or different environmental control requirements.

In conclusion, the SBX1 meets its individual design goals of environmental control, imaging, and cost. There is still work to be done to resolve condensation and gas sealing issues, and improvements are necessary for the optics; however, on the whole the prototype can be considered a success.

Results presented in this thesis are based upon collaborative work supported by a National Science Foundation NRT Grant No. 1450032. Any opinions, findings, conclusions or recommendations expressed in this paper are those of the author(s) and do not necessarily reflect the views of the National Science Foundation.

Bibliography

[1] Fisher Scientific. Incubators.

[2] Chiara Schiraldi and Mario De Rosa. Mesophilic Organisms. In Enrico Drioli and Lidietta Giorno, editors, *Encyclopedia of Membranes*, pages 1285–1286. Springer Berlin Heidelberg, Berlin, Heidelberg, 2016.

[3] David Botstein, Steven A. Chervitz, and Michael Cherry. Yeast as a Model Organism. *Science*, 277(5330):1259–1260, 1997. Publisher: American Association for the Advancement of Science _eprint: https://science.sciencemag.org/content/277/5330/1259.

[4] J. Nielsen. Yeast Systems Biology: Model Organism and Cell Factory. *Biotechnol J*, 14(9):e1800421, September 2019.

[5] P. Jorjani and S. S. Ozturk. Effects of cell density and temperature on oxygen consumption rate for different mammalian cell lines. *Biotechnol Bioeng*, 64(3):349–356, August 1999.

[6] S. R. McKeown. Defining normoxia, physoxia and hypoxia in tumours-implications for treatment response. *Br J Radiol*, 87(1035):20130676, March 2014.

[7] National Oceanic and Atmospheric Administration, National Aeronautics and Space Administration, and United States Airforce. U.S. Standard Atmosphere, 1976. Technical report, National Oceanic and Atmospheric Administration, Washington, D.C., October 1976.

[8] Jim Cooper. Carbon dioxide Concentration and pH Control in the Cell Culture Laboratory., April 2019. Publisher: Culture Collections.

[9] Klaus Froehlich, Willem G Mook, and W Stichler. *Environmental Isotopes in the Hydrological Cycle*, volume 3. International Atomic Energy Agency, Paris/Vienna, March 2000.

[10] Nikon Instruments Inc. Darkfield Illumination.

[11] Nikon Instruments Inc. Introduction to Phase Contrast Microscopy.

[12] Arianne Heinrichs. Stains and fluorescent dyes. *Nature Cell Biology*, 11(1):S7–S7, October 2009.

[13] Sowmya Swaminathan. GFP: the green revolution. *Nature Cell Biology*, 11(1):S20–S20, October 2009.

[14] Christopher P Toseland. Fluorescent labeling and modification of proteins. *Journal of chemical biology*, 6(3):85–95, April 2013. Publisher: Springer-Verlag.

[15] G. Nebe-von Caron, P. J. Stephens, C. J. Hewitt, J. R. Powell, and R. A. Badley. Analysis of bacterial function by multi-colour fluorescence flow cytometry and single cell sorting. *J Microbiol Methods*, 42(1):97–114, September 2000.

[16] N. Rodriguez-Sastre, C. F. Thomas, and C. A. Bradham. Measuring voltage and ion concentrations in live embryos. *Methods Cell Biol*, 151:459–472, 2019.

[17] Essen Bioscience. Publications - Discoveries and Innovations from Incucyte.

[18] Mordor Intelligence. INCUBATOR DEVICES MARKET - GROWTH, TRENDS, AND FORECASTS (2020 - 2025). Technical report, Mordor Intelligence, Hyderabad, India.

[19] Nick Tippmann. Ultimate List of Medical Device Incubators and Accelerators (50+), January 2018.

[20] Orion Market Research Pvt. Ltd. Global Incubator Devices Market Size, Share & Trends Analysis Report by Product Type (Neonatal Incubators, Microbiological Incubators, and Others) By End-User (Hospitals, Diagnostic Labs, Others) Forecast Period (2019-2025). Technical report, Orion Market Research Pvt. Ltd, Madhya Pradesh, India, May 2020.

[21] paige Roovers. Planer BT37 Quote, April 2020.

[22] Carnevale, Elaine. Micro Q Incubator application and Cost, May 2020.

[23] Cooper Surgical. Planer BT37 Mark II bench top incubator – CooperSurgical Fertility Companies, September 2019.

[24] Planer Limited. BT37 MarkII Model No: BT37-02 Service Manual. User Manual MA200606 1.0.0, 2021.

[25] K-SYSTEMS. Instruction Manual CO2 Bench Top Incubator G85. Manual.

[26] Ilercil, Alp, May 2020.

[27] Micro Q Technologies LLC. Transportable Incubator, Temperature Controlled Transportable Incubator, Precision Temperature Controlled Transportable Incubator.

[28] OKOLAB S.R.L. Okolab - H301-K-FRAME.

[29] Warner Instruments. OKOLab Cage Incubator System Overview.

[30] IBIDI GMBH. ibidi Stage Top Incubation System, Universal Fit, for 1 Chamber, CO2/O2.

[31] OKOLAB S.R.L. HM-ACTIVE.

[32] OKOLAB S.R.L. H301-T-UNIT-BL-PLUS Electric Top Stage Incubation System Manual Vers. 01.17. Technical report, OKOLAB S.R.L., March 2017.

[33] OKOLAB S.R.L. HM-ACTIVE Humidity Controller Manual v01.17. Technical report.

[34] IBIDI GMBH. Instruction Manual ibidi Gas Incubation System version 2.2. Technical report, IBIDI GMBH, May 2019.

[35] IBIDI GMBH. Instruction Manual ibidi Heating System, Universal Fit Version 2.2. Technical report, IBIDI GMBH, May 2019.

[36] Tokai Hit Co., Ltd. Stage Top Incubator STX series.

[37] Tokai Hit Co., Ltd. Tokai Hit for Leica Microsystems, August 2019.

[38] OKOLAB S.R.L. Stage Top Chamber.

[39] Inc. OMEGA Engineering. Thermocouple Wire Special Limits of Error.

[40] Shridhar Atmaram More. Thermocouple, Cold-Junction Compensation—Analog Approach. Technical report, Texas Instruments, 2014.

[41] World Precision Instruments Inc. Full Chamber Environmental Central Unit.

[42] Digital Pixel Limited. Microscope Incubation systems.

[43] OKOLAB S.R.L. Okolab - Cage - Digital/Manual/Premixed.

[44] World Precision Instruments Inc. Instruction Manual ECU STEV2. Technical report, World Precision Instruments Inc., 2020.

[45] Elliot Scientific Limited. Microscope Incubation Systems.

[46] Essen BioScience. IncuCyte Live-Cell Analysis - Empower Live-Cell Research Inside Your Incubator, 2020.

[47] Thermo Fisher Scientific Inc. EVOS Light Cube Selection Guide - US.

[48] Keegan Walhood. Phone conversation regarding capabilities of Keyence BZ-X800E., April 2020.

[49] Carl Zeiss Microscopy GmbH. Phone Interview with Sales and Technical Representatives, 2020.

[50] Carl Zeiss Microscopy GmbH. Zeiss LSM 9 Family with Airyscan 2, 2019.

[51] Thermo Fisher Scientific Inc. EVOS M7000 Cell Imaging System, 2018.

[52] Keyence Corporation of America. All-in-One Fluorescence Microscope BZ-X800E, 2019.

[53] Essen Bioscience. Technical Specifications IncuCyte S3 Live-Cell Analysis System, 2018.

[54] Essen Bioscience. Technical Specifications IncuCyte S3 Live-Cell Analysis System for NeuroScience, 2018.

[55] PeCon GmbH. PeCon GmbH | CO2-O2-Controller 2000.

[56] Mike Howren. Quote for M7000, April 2020.

[57] Anna Magallanez. Quote for IncuCyte S3, April 2020.

[58] Keyence Corporation of America. Quotation, May 2018.

[59] Amy Courtney, Luke M. Alvey, George O.T. Merces, and Mark Pickering. The Flexiscope: a Low Cost, Flexible, Convertible, and Modular Microscope with Automated Scanning and Micromanipulation. *bioRxiv*, 2018. Publisher: Cold Spring Harbor Laboratory _eprint: https://www.biorxiv.org/content/early/2018/10/12/442210.full.pdf.

[60] M. P. Walzik, V. Vollmar, T. Lachnit, H. Dietz, S. Haug, H. Bachmann, M. Fath, D. Aschenbrenner, S. Abolpour Mofrad, O. Friedrich, and D. F. Gilbert. A portable low-cost long-term live-cell imaging platform for biomedical research and education. *Biosens Bioelectron*, 64:639–649, February 2015.

[61] A. J. Kabla. OpenLabTools, 2013.

[62] Goodfellow Group. Goodfellow - Catalogue.

[63] SST Sensing Ltd. LuminOx Cross Sensitivity Application Note, 2013.

[64] GasLab.com. Oxygen Sensors Features Comparison. Technical report.

[65] Bosch Sensortec GmbH. BME280 Combined Humidity and Pressure Sensor, September 2018.

[66] Fisher Scientific. Fisherbrand™ Traceable™ International Standards Extreme-Accuracy Digital Thermometers.

[67] Ferrotec Corporation. Reliability of Thermoelectric Cooling Modules.

[68] E.M. Greitzer, Z. S. Zpakovsky, and I. A. Waitz. 16.Unified: Thermodynamics and Propulsion Prof. Z. S. Spakovszky.

[69] Calin Zamfirescu and İbrahim Dinçer. Appendix D Psychometric Properties of Humid Air. In *Drying Phenomena*, pages 463–467. John Wiley & Sons, Ltd, 2015. _eprint: https://onlinelibrary.wiley.com/doi/pdf/10.1002/9781118534892.app4.

[70] Erik Cheever. Mathematical Models of Thermal Systems.

[71] Paul A. Tipler and Gene Mosca. Chapter 18: Heat and the First Law of Thermodynamics. In *Physics for Scientists and Engineers*, volume 1. 6 edition, 2008.

[72] Inc. The Mathworks. Analyze Design in PID Tuner - MATLAB & Simulink.

[73] Hodge Jenkins. MAE 691 Modern Control Theory, 2016.

[74] LLC Molex. Micro-Lock Plus Wire-to-Board Connector System - Molex.

[75] IEWC. Suggested Ampacities.

[76] Panasonic Corporation. Automation Controls Catalog: AQ-H Relays, 2020.

[77] Texas Instruments Inc. LP8860-Q1 Low-EMI Automotive LED Driver With Four 150-mA Channels. Datasheet SNVSA21G, Texas Instruments, October 2017.

[78] Texas Instruments Inc. Basic Calculation of a Boost Converter's Power Stage. Application Report SLVA372C, January 2014.

[79] Inc. Luminus Devices. MP-2016-1100 Mid Power Product Datasheet. Datasheet, Sunnyvale, CA, 2019.

[80] Samantha Montes de Oca. What Is CRI?, March 2016. Section: Learning Center.

[81] Vishay Intertechnology. VLMU1610-365-135 Rev. 1.2. Datasheet 84374, Malvern, PA, October 2018.

[82] Inc. Cree. Cree® XLamp® ML-E LEDs. Datasheet CLD-DS30 Rev 12, Cree, Inc., Durham, NC, 2021.

[83] Inc. Analog Devices. DEMO MANUAL DC2155A-A/DC2155A-B Rev. C. Technical report, February 2020.

[84] Atmel Corporation. ATmega328P. Technical Report 7810D-AVR-01/15, Microchip Technology Inc., San Jose, CA, 2015.

[85] Allegro Microsystems. A4988 DMOS Microstepping Driver with Translator and Overcurrent Protection. Technical Report MCO-0000827, Manchester, NH, 2020.

[86] Raspberry Pi Foundation. Power Supply - Raspberry Pi Documentation.

[87] Texas Instruments Inc. TPS84621 2.95-V to 14.5-V Input, 6-A Synchronous Buck, Integrated Power Solution. Datasheet SLVSAW7E, Texas Instruments Inc., Dallas, TX, April 2018.

[88] LTD. Mean Well Eenterprises CO. 450W Single Output Power Supply. Datasheet SE-450-SPEC, Mean Well Eenterprises CO., LTD., New Taipei City, April 2021.

[89] IPC. IPC-2221 Generic Standard on Printed Board Design. Standard ANSI/IPC-2221, IPC, Bannockburn, IL, February 1998.

[90] CircuitCalculator.com. Online Circuit Calculators, January 2006.

[91] Hashim Mir, Peter Xu, and Peter van Beek. An extensive empirical evaluation of focus measures for digital photography. volume 9023, March 2014.

[92] Brian Dean and Joerg Wunsch. AVRDUDE Downloader/UploaDEr - Summary, February 2016.

[93] Inc. Teknic. ClearPath® - Integrated Servo System, 2021.

[94] Sony Corporation. Diagonal 4.60 mm (Type 1/4.0) 8 Mega-Pixel CMOS Image Sensor with Square Pixel for Color Cameras IMX219PQH5-C. Datasheet E13Y12F44, Minato City.

[95] Kenneth R. Spring, Brian O. Flynn, Jogn C. Long, and Michael W. Davisdson. Spatial Resolution in Digital Imaging.

[96] Joel S. Silfies, Stanley A. Schwartz, and Michael W. Davidson. The Diffraction Barrier in Optical Microscopy.

[97] Richard W. Bowman, Boyko Vodenicharski, Joel T. Collins, and Julian Stirling. Flat-Field and Colour Correction for the Raspberry Pi Camera Module. *Journal of Open Hardware*, 4(1):1, April 2020. Number: 1 Publisher: Ubiquity Press.

[98] Thermo Fisher Scientific Inc. FocalCheck™ Fluorescence Microscope Test Slides. Datasheet MP 36906, Carlsbad, CA, August 2011.

[99] Ewa M. Goldys. *Fluorescence Applications in Biotechnology and the Life Sciences*, volume 1. August 2009.

[100] Joseph R. Lakowicz. *Principles of fluorescence spectroscopy*. Springer, New York, 3rd ed edition, 2006.

[101] Edmund Optics Inc. Understanding Microscopes and Objectives.

[102] Discover Echo Inc. Revolve Fluorescence Microscope by Echo, 2021.

[103] United Financial Casualty Company. General Liability Insurance Cost.

Appendix A

Circuit Diagrams

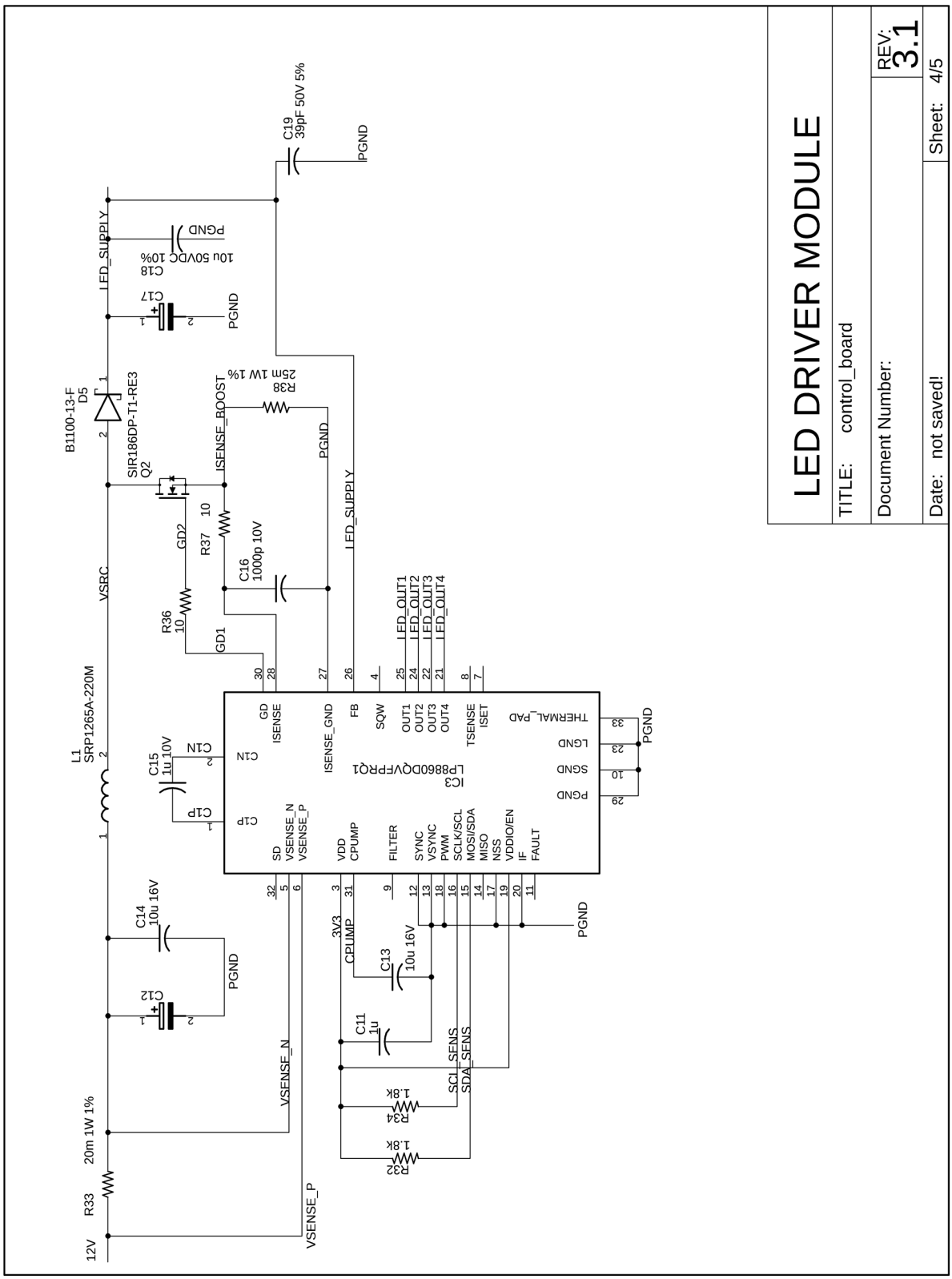

Figure A.1: Control Board Schematic Sheet 1

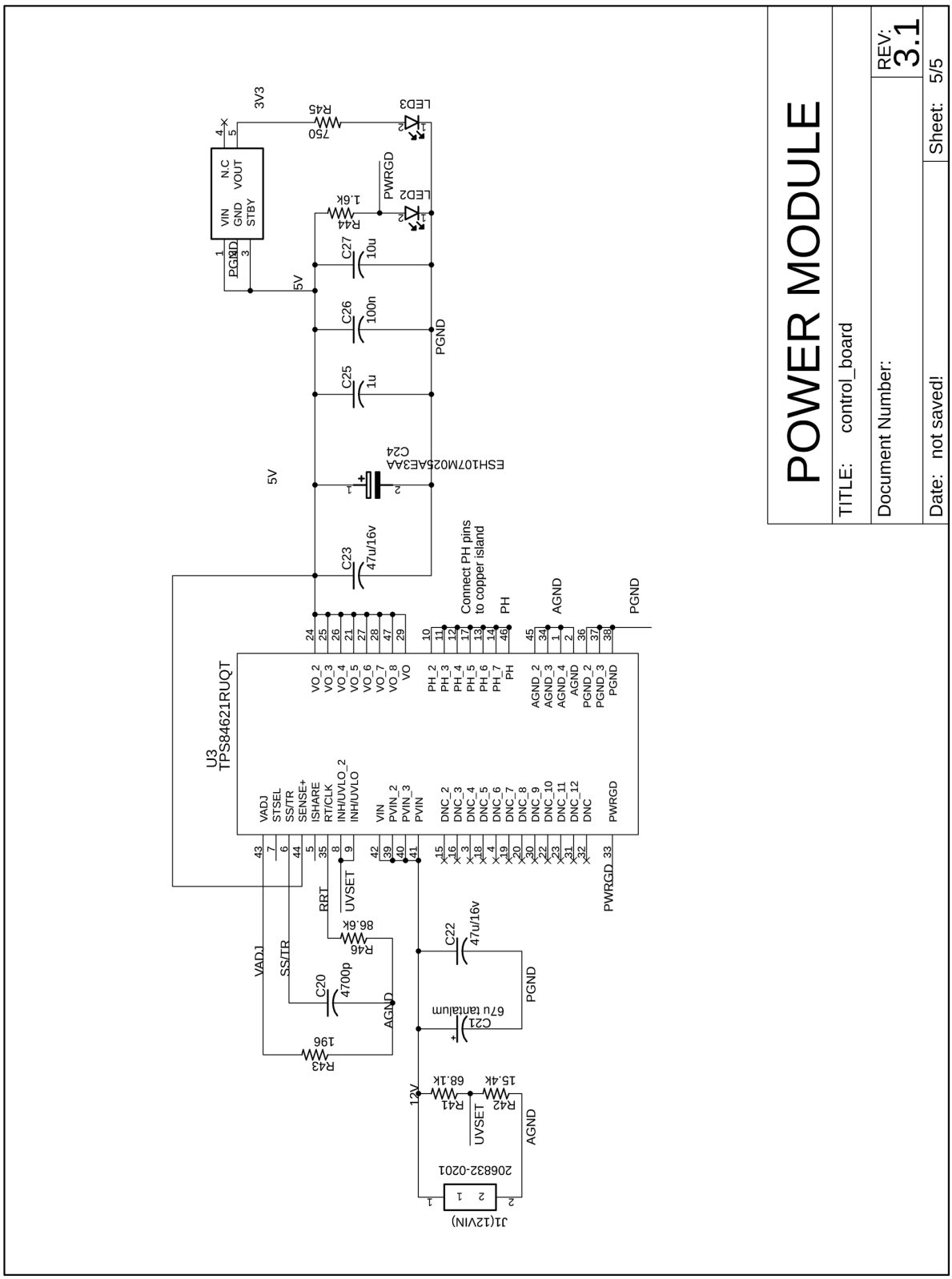

Figure A.2: Control Board Schematic Sheet 2

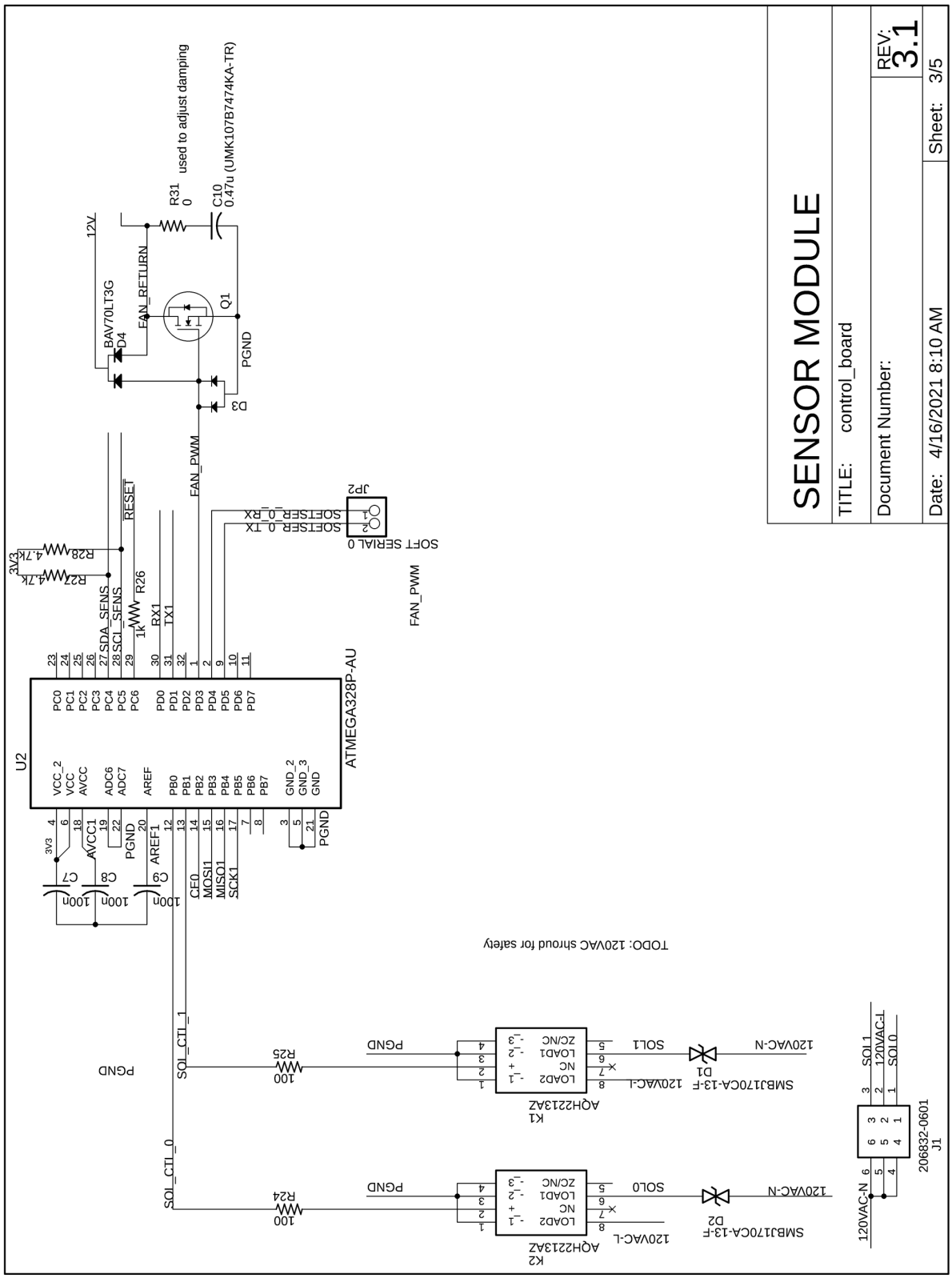

Figure A.3: Control Board Schematic Sheet 3

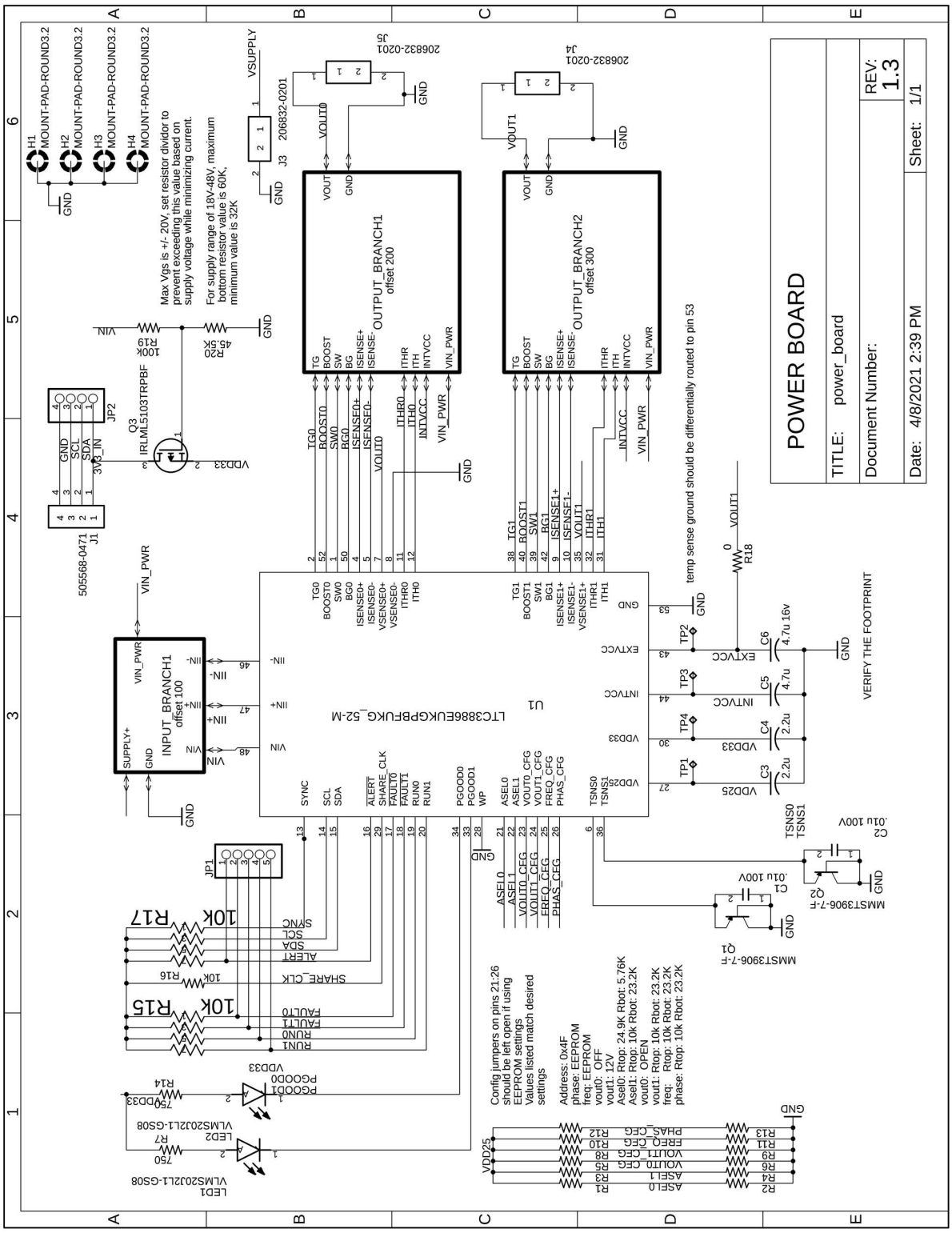

Figure A.4: Power Board Schematic Sheet 1

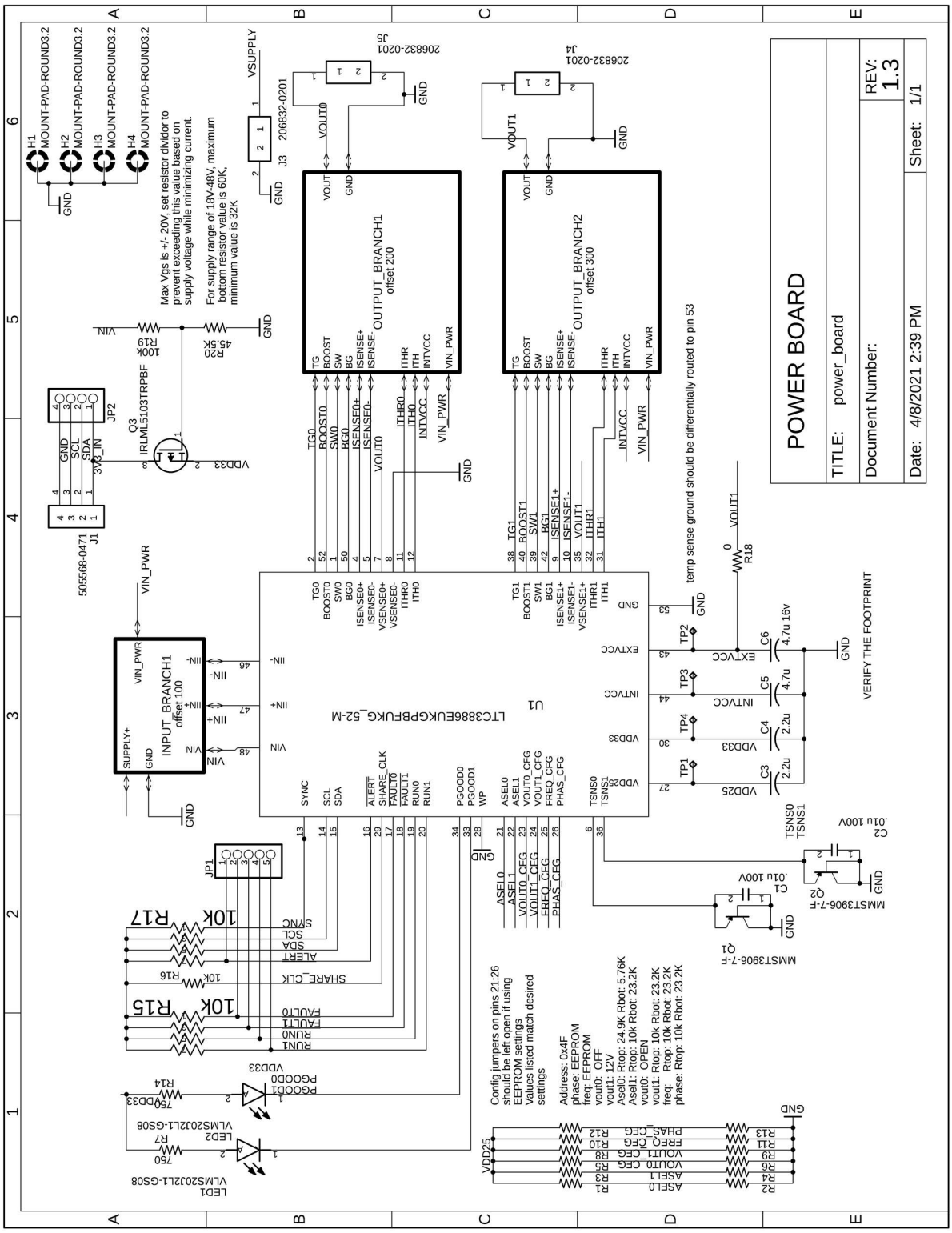

Figure A.5: Power Board Schematic Sheet 2

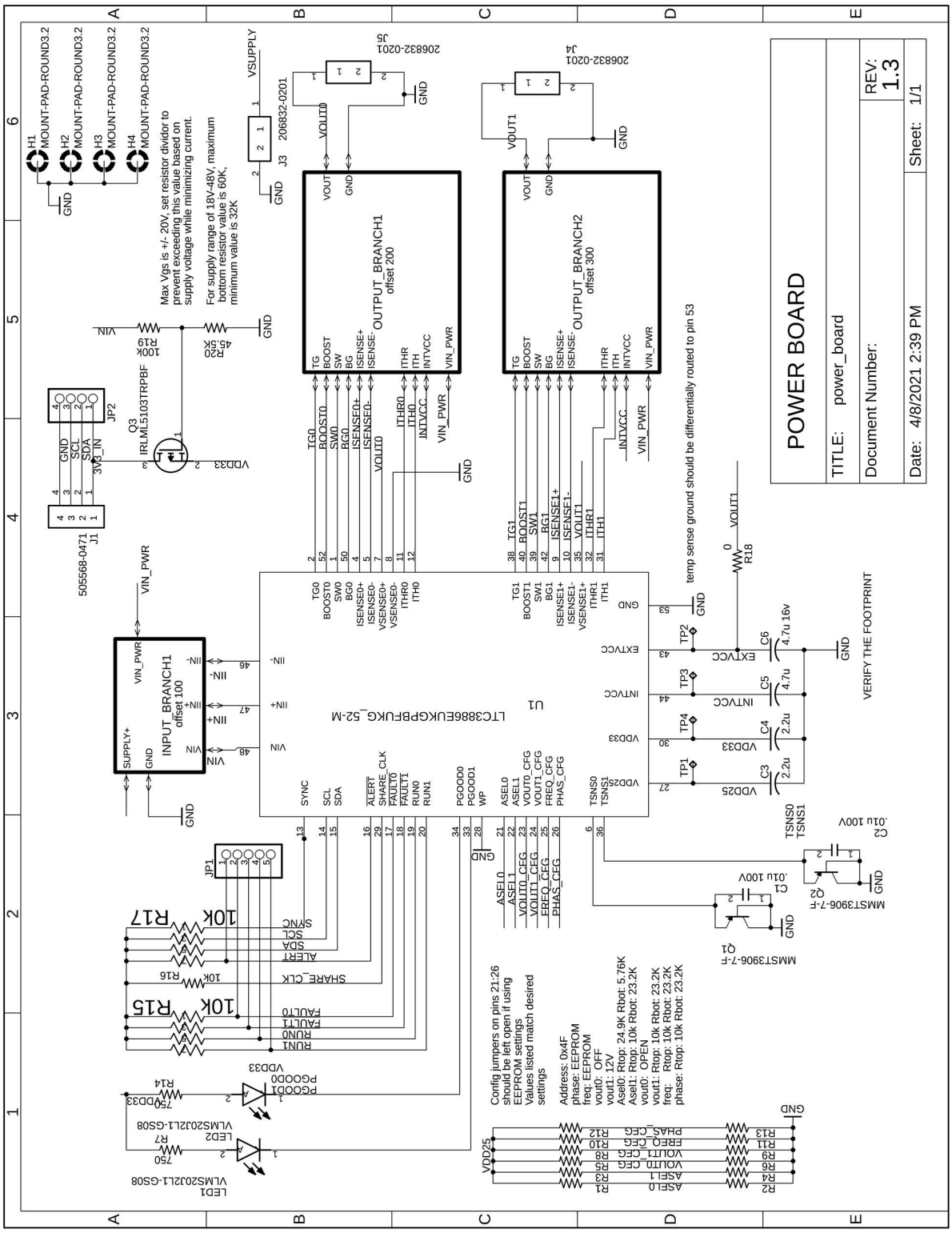

Figure A.6: Power Board Schematic Sheet 3

Appendix B

Cost Breakdown

Summary of costs for a single unit. Component costs assume bulk pricing for 100 units. Prices for shell components are based on volume plus 20% for supporting material, with a resin cost of $40/L for SLA printing. Costs do not include shipping or taxes. PCB assembly costs are included in the price for each board.

For labor costs, we consider two production rates of 1000 units per year and 100 units per year.There are 261 working days in a year, requiring 3.83 or 0.383 units produced per day respectively. Assume that three people with an efficient pipeline can produce a single unit per day. This means a requirement of 12 workers to produce 1000 units per year or 2 workers to produce 100 per year. Also assume that two support technicians are available during normal working hours. All of these employees are paid a $50,000/year wage.

Liability insurance costs may be a factor; however general liability insurance is inexpensive. Progressive states an average of $53 [103] per month for general liability insurance, a negligible amount amortized over 1000 boxes.

A breakdown of expected costs is shown in Table B.1.

Table B.1: The calculated field of view and Rayleigh Resolution at 500nm for each objective.

Section	Component	Cost per Unit
Enclosure	Shell	$183.36
	hardware	$4.06
Electronics	Control board	$131.56
	Power board	$41.25
	Interface Board	$8.99
	Power Supply	$53.12
	Interconnecting Cables	$24.832
Microscope	Optical Chain	$339
	Objectives	$128
	Camera	$25
	Gantry	$914.09
	LED Ring	$21.4
Environmental Control	Sensors	$20
	Heat Exchanger	$192
	Solenoids	$26
	Humidifiers	$22
	Total	$2134.66
Labor	Assembly (1000 units/year)	$600
	Technical Support(1000 units/year)	$100
	Assembly (100 units/year)	$1000
	Technical Support(100 units/year)	$1000